Evaluation of Carbon Characteristics' Influence on the Performance of Electrochemical Capacitor Systems Combining Double-Layer and Pseudocapacitive Electrode Materials

by

Adrienne Allison

Submitted in partial fulfilment of the requirements
for the degree of Doctor of Philosophy

at

Dalhousie University
Halifax, Nova Scotia
December 2022

To my father, may he rest in peace.

Table of Contents

List of Tables

List of Figures

Abstract

Electrochemical capacitors are energy storage devices that are uniquely capable of high power and extraordinarily long cycle life. Carbon materials are typically used to store energy in electrochemical capacitors, but the low energy density of these materials limits the expanse of applications for which they can be used. Pseudocapacitive materials, such as manganese oxides, could improve the energy density of electrochemical capacitors but suffer from lower power and lower cycle life compared to their carbon counterparts. In recent years, there has been increasing interest in combining carbon and pseudocapacitive materials in order to benefit from the high power density and high energy density that these materials offer respectively.

The work presented in this thesis explores the electrochemistry of a number of different carbon materials, highlighting differences in the abundance of redox-active functional groups (which increase the carbon energy density) as well as differences in the carbons' rate capabilities. Importantly, we show that electrochemical experiments in neutral-pH electrolyte cause an increase in redox-active surface functional groups on carbon materials, despite the fact that these species are not detectable in the neutral-pH electrolyte itself.

Additionally, this work identifies the origin of interfacial resistance in manganese oxide films as resistance between the manganese oxide and its substrate. This is an important discovery, as this resistance is commonly mis-identified in the literature as an intrinsic property of manganese oxide. Experiments exploring the performance of manganese oxide electrodeposited onto carbon do not demonstrate this resistance between manganese oxide and carbon substrates.

Experiments exploring the effect of carbon surface area and chemistry on the performance of electrodeposited manganese oxide found no significant impact for these carbon properties. However, electrodeposited manganese oxide is able to greatly improve the energy storage of carbon with only a small decrease in the rate capabilities. This is thought to perhaps be due to manganese oxide depositing on the outer surface of carbon, rather than down the pores where it will be impeded by resistance associated with ion movement through tight spaces.

List of Abbreviations Used

A	ampere
A	cross-sectional area
Ag/AgCl	silver/silver chloride reference electrode
C	coulomb, capacitance, capacitor
°C	degree Celsius
C_{im}	imaginary component of capacitance from impedance
C_{real}	real component of capacitance from impedance
CPE	constant phase element
CV	cyclic voltammogram
E_0	impedance potential perturbation amplitude
E_{BE}	binding energy
EC	electrochemical capacitor
EDS	energy dispersive X-ray spectroscopy
EIS	electrochemical impedance spectroscopy
E_k	kinetic energy
eV	electron volt
F	farad
h	Planck's constant (6.626 x 10-34 m ^{2} kg s^{-1})
Hz	hertz
I	current

I_0	impedance current response amplitude
L	length
M	molar
$MnOx_{10dry:90wet}$	10% heat-treated and 90% wet-stored manganese oxide
$MnOx_{dry}$	heat-treated manganese oxide
$MnOx_{wet}$	wet-stored manganese oxide
R	resistance, resistor
SCE	saturated calomel electrode
SEM	scanning electron microscopy
SHE	standard hydrogen electrode
t	time
V	volt
W	work function, Warburg element
XPS	X-ray photoelectron spectroscopy
Z	impedance
Z_{im}	imaginary component of impedance
Z_{real}	real component of impedance
ν	speed of light ($2.998*10^8$ m s^{-1}), sweep rate
ρ	resistivity
Φ	impedance phase shift
Ω	ohm
ω	angular frequency

Acknowledgements

Special thanks to my supervisor, Dr. Heather Andreas, for her continued support and guidance. It has been a privilege to work in her lab and I feel that I have grown immensely as a scientist under her counsel. I would also like to acknowledge Todd Carter for his glass blowing skills, without which I would not have been able to use microcavity electrodes (not to mention the surplus of broken electrodes that would be occupying the lab). Thank you to Andrew George for running XPS analysis on my carbon samples, and to Dr. Patricia Scallion for training me and providing her expertise for the collection of SEM images and EDS. I would also like to thank my supervisory committee members, Dr. Peng Zhang, Dr. Mita Dasog, and Dr. Erin Johnson for all their advice and insights with respect to this project. I appreciate all the graduate school colleagues who have ever edited my work, listened to my presentations, or humoured me as I complained about experiments not working. The biggest thanks goes out to my love, Raymond, who has made this entire process so much easier on me.

Chapter 1: Introduction

Rising global temperatures have spurred environmental concerns regarding the burning of fossil fuels for energy. Renewable energy alternatives, such as wind and solar, are intermittent in nature and therefore require large-scale energy storage to accommodate the energy demands of consumers. Of the different energy storage systems (batteries, fuel cells, and electrochemical capacitors), batteries have received the most attention as means to alleviate this problem, in part due to their high energy density making them appropriate for grid storage. However, batteries have limitations when it comes to power, i.e., how quickly they can store and release energy. Electrochemical capacitors (ECs), on the other hand, have inherently higher power capabilities and as such are often used in situations where other energy storage systems cannot respond fast enough.

For example, ECs are paired with batteries to aid in load-leveling in energy storage from wind turbines.[1] This helps store energy during sudden wind fluctuations, energy that could not be harnessed by the slower battery system. ECs can also be paired with batteries or fuel cells in electric vehicles, decreasing the energy demands by supplying energy through regenerative breaking wherein energy released during breaking is used during acceleration.[2] This decreases the total energy required from the battery or fuel cell, meaning smaller, lighter devices can be implemented. ECs are therefore an important tool in the energy storage field, particularly when there are high-power demands. Additionally, the extraordinarily long cycle life of ECs (up to 10^3 times the

cycle life of batteries)[3] means that they rarely need to be replaced. However, in many applications it is impractical to exclusively use an EC as energy storage, as the energy density of these systems is typically very poor compared to batteries and fuel cells.[3]

There are two main types of electrode materials that can be used for EC applications: carbon and pseudocapacitive materials. Carbon materials store energy via electrostatic attractions at the electrode-electrolyte interface, whereas pseudocapacitive materials (which include some transition metal oxides and conductive polymers) store energy through kinetically fast and highly reversible Faradaic reactions. Due to the processes by which these materials store energy, carbon inherently has higher power density whereas pseudocapacitive materials have higher energy density.[4] In recent years, there has been a surge in literature exploring electrodes that combine both carbon and pseudocapacitive materials.[4–8] The hope is that the pseudocapacitive material can boost the energy density of the system, while the high power density is maintained due to the presence of the carbon material. In addition to maintaining high power density, it is also critical to maintain high cycle life, as this the other main advantage of ECs. Unfortunately, pseudocapacitive materials tend to suffer from comparatively poor rate capabilities and higher instability compared to their carbon counterparts. Therefore, it is important that the rate capabilities and stability of pseudocapacitive materials in these systems are maximized as much as possible in order for them to be compatible with the niche applications in which EC devices are typically employed.

The goal of this thesis is to elucidate how various characteristics of carbon materials may impact the electrochemical performance and stability of pseudocapacitive

materials when the two materials are combined in the same electrode. How carbon materials and pseudocapacitive manganese oxide perform both separately and together will be explored. Chapter 2 provides context for this work by outlining the theories and literature precedent that brought about the goals of this thesis and Chapter 3 will provide the necessary details for the experimental methods used to achieve those goals.

In Chapter 4, the electrochemical performance of four different carbon materials is established. Long-term cyclic voltammetry in acidic electrolyte allows any changes in redox-active surface functional groups to be tracked over time, providing insight into how these carbon materials change during electrochemical experiments. Similar cyclic voltammetry experiments in neutral pH electrolyte provide insight into how these carbon materials may change differently during electrochemistry in less acidic media, which is important as the introduction of pseudocapacitive manganese oxide will require a near neutral pH. Additionally, the rate capabilities of these different carbons are explored to establish how fast the potential can be changed before there is a loss in capacitance (i.e., a loss in active surface area).

Chapter 5 identifies the origin of semi-circular features in the electrochemical impedance spectroscopy Nyquist plots of manganese oxide films. This is critical, as the origin of this feature has been historically mis-identified in the literature. Importantly for this project, semi-circles that may arise in Nyquist plots of manganese oxide on carbon materials can now be linked to poor contact between the manganese oxide and the substrate. This insight into the origin of this common Nyquist plot feature prompts an

exploration into how to determine what circuit model (or models) appropriately represent pseudocapacitive manganese oxide.

Chapter 6 delves into the electrochemical behaviour of electrodes that combine carbon and pseudocapacitive manganese oxide. First, an assessment was made of how to best combine these materials by testing a number of different manganese oxide electrodeposition protocols. The impact of varying the amount of manganese oxide on different carbon substrates was also assessed. Using our newfound understanding of manganese oxide's Nyquist plot as gained in Chapter 5, we were able to evaluate the connection between manganese oxide and carbon in all our tested electrodes. The impact of carbon's surface area on the performance of these electrodes was studied by comparing manganese oxide on two graphite materials with differing particle sizes. Additionally, the impact of carbon surface chemistry on electrode performance was assessed by comparing electrodes with as-received Vulcan XC-72 carbon and Vulcan XC-72 that was oxidized electrochemically, using the same electrochemical tests that were shown to cause changes in carbon surface chemistry in Chapter 4.

The work presented in this thesis provides insight into how the surface chemistry of carbon materials changes during electrochemistry in both acidic and neutral-pH electrolytes and establishes the electrochemical impedance spectroscopy behaviour of manganese oxide. Considerations for how to best combine carbon materials and electrodeposited manganese oxide are detailed. Our manganese oxide electrodeposition method seems to allow the carbon substrates to remain electrochemically active, which was an important factor in the performance of these electrodes at fast rates. Importantly,

the impact of carbon characteristics like surface area and surface chemistry were not shown to have an impact on manganese oxide's electrochemical performance in these electrodes. Ultimately, we were able to create electrodes that benefitted from manganese oxide's high energy storage capabilities, while maintaining carbon activity at fast rates. Future work is outlined in detail in Chapter 8 and describes further experiments that could be completed to expand upon this research.

Chapter 2: Background

2.1 Electrochemical Capacitor Materials

Electrochemical capacitors (ECs) are energy storage systems that owe their name to their capacitor-like behavior. This means that ECs are able to charge and discharge rapidly, especially compared to other energy storage systems. These high rate capabilities of ECs make them particularly useful in high power applications such as camera flashes,[9] load-leveling in wind turbines,[1] and load-leveling in electric vehicles to improve acceleration.[2] ECs attain this fast charging and discharging due the rapidity of the mechanisms by which their materials store energy: double-layer charge storage and pseudocapacitive Faradaic reactions.

Double-layer charge storage is the main charge-storage mechanism utilized by carbon materials in ECs. In double-layer charge storage, charge that is applied to the material surface is balanced by ions in electrolyte, which are electrostatically attracted to the surface, forming a double layer of charge at the electrode/electrolyte interface (Figure 2-1). Because this mechanism does not involve changes in the chemical composition or structure of the material, EC materials that utilize double-layer charge storage are able to charge and discharge repeatedly with minimal loss in energy density (with cycle lives upwards of 1 000 000).[3] The high cycle life of these systems makes them useful in energy storage applications requiring repeated charging and discharging without replacement of the device, such as regenerative breaking and energy storage in remote locations.[1] Carbon materials are especially attractive for use in ECs not only due to their stability, but also

their abundance, inexpensiveness and their high specific surface areas, which allow for more energy to be stored via the double-layer charge storage mechanism.

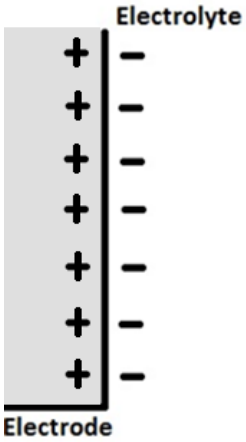

Figure 2-1. Diagram showing a simplified version of the double layer charge-storage mechanism.

Pseudocapacitive Faradaic reactions are redox reactions that have fast kinetics and high reversibility, and that achieve a capacitor-like response.[10] Because pseudocapacitive materials store energy via Faradaic reactions, they can store one or multiple electrons per surface site (unlike carbon, which mainly stores energy via double-layer charge storage, storing only ~0.2 e^- per surface atom[3]). This gives pseudocapacitive materials much higher energy densities than their carbon counterparts,[4] ameliorating one of the main shortcomings of ECs as energy storage systems. However, because of their energy storage mechanism, pseudocapacitive materials present a slower response (i.e., lower power) compared to carbon-based materials in ECs.[4] This is problematic because ECs are typically employed in high power (or fast rate) applications. Materials that have been shown to have pseudocapacitive behaviour include certain polymers and transition-metal-

based materials. This thesis focuses on a pseudocapacitive material that is transition-metal-based due to its established history, accessibility, and ease of handling in our laboratory setting.

There exists a limited range of transition metal oxides and sulfides that present pseudocapacitive behaviour, including ruthenium oxide,[9,11,12] manganese oxides,[6–8,11,13,14] and molybdenum sulfide.[15] In addition to having lower rate capabilities than carbon materials, pseudocapacitive transition metal oxides sometimes suffer from poor stability, high cost, negative environmental impact, and sustainability issues. This thesis focuses on pseudocapacitive manganese oxides, which are abundant, environmentally friendly, and cost-effective.[16] Manganese oxides have pseudocapacitive behavior due to the following Faradaic reaction: $MnOOX^+ \rightleftharpoons MnO_2 + X^+ + 1e^-$, where X^+ is an electrolyte cation.[14] One of the advantages of manganese oxides over other materials is that they exhibit true pseudocapacitive behaviour over a relatively large potential window, unlike many other materials that are studied for pseudocapacitive applications.[10] As such, manganese oxides are one of the more promising pseudocapacitive transition metal oxides.

Pseudocapacitive Faradaic reactions can also occur on carbon materials, even though they mainly store energy via double-layer charge storage. These Faradaic reactions can occur due to redox-active surface functional groups or contaminants. Many surface functional groups are known to exist on carbon materials including lactone, carbonyl, carboxylic acid, phenol, and quinone groups.[17] Of these, quinone groups are the most widely studied in electrochemistry,[18–20] as they are able to undergo a fast Faradaic reaction in acidic electrolyte (Figure 2-2). The presence of this reaction increases the

energy density of the carbon material, but it has been shown that the formation of these quinone groups may contribute to self-discharge (i.e., spontaneous loss in stored energy as the material sits unused).[20] Whether these types of electrochemically active functional groups are a positive or negative attribute, they are an important consideration when evaluating the electrochemical performance of carbon materials.

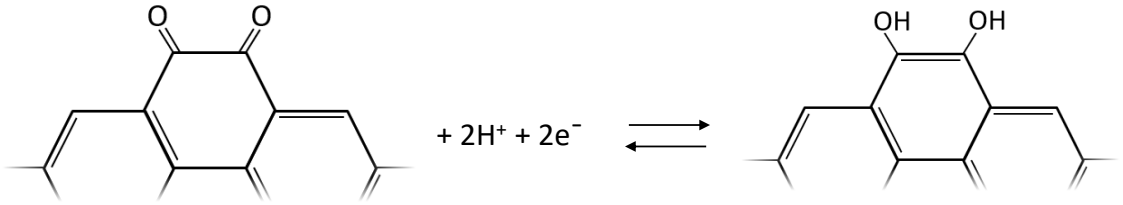

Figure 2-2. Faradaic reaction of ortho-quinone in acidic electrolyte.

It is noteworthy that even functional groups that do not participate in Faradaic reactions can influence the electrochemical behaviour of carbon materials. For example, ether and carbonyl groups on carbon surfaces have been shown to inhibit the reduction of hemoglobin.[21] Additionally, nitrogen- and oxygen-containing functional groups have been found to increase the wettability of carbon materials,[22–24] thereby improving the materials' contact with aqueous electrolytes. However, it is not yet well understood how carbon surface functionalities may affect other aspects electrochemical performance. For instance, it has not been established how carbon surface functional groups may influence the connection between pseudocapacitive transition metal oxides and carbon surfaces. This connection is critical to the performance of ECs as it can decrease the overall resistance of the system (which is necessary for high-power applications).

Because carbon materials mainly store energy via double-layer charge storage, they tend to have lower energy density (but higher power density) than pseudocapacitive materials. However, there are other variables that impact the overall power of a system besides the material's energy storage mechanism, such as the material thickness and porosity. Unfortunately, altering these parameters comes with a tradeoff. For example, using a thinner film of pseudocapacitive material will lead to an improvement in power capabilities. Regrettably, this also decreases the amount of active electrode material, resulting in a decrease in energy storage capacity. Similarly, one might try to improve the energy storage of a carbon material simply by increasing its specific surface area. However, the surface area of carbon materials is related to the porosity of the material, and the size of the pores can also influence other aspects of electrochemical performance. Pores that are thinner or longer have a greater resistance to electrolyte ions,[25–27] as is evident by equation 1 (where R is resistance, ρ is the resistivity, L is length, and A is cross-sectional area).

$$(1)\quad R = \frac{\rho L}{A}$$

Utilizing electrochemical double-layer charge storage requires there to be electrolyte ions at the carbon surface. High resistance hinders distribution of ions down pores and can therefore lead to a loss of utilized surface area at fast rates (i.e., at high power). This means that although very small micropores can increase the surface area (and therefore increase the energy density), they may result in a forfeit of high-power capabilities, which is the most important parameter in many EC applications. Therefore, mesoporous

(2 nm to 50 nm) carbon networks are considered necessary for good EC performance. Evidently, there is a tradeoff between power and energy when manipulating film thickness or porosity to optimize an EC system.

It is important to note that the porosity of carbon materials is impacted both by how the carbon material was made, and how that carbon material was made into an electrode. In working with carbon powders (of which many carbon-based electrodes are made), there are two main considerations when it comes to porosity. Depending on how a carbon material was synthesized it will have a certain pore-size distribution, which will affect the porosity within each carbon particle. However, the channels between the carbon particles can also introduce porosity to the system and this can change depending on how the carbon electrodes are fabricated. A diagram depicting this porosity within carbon particles and between carbon particles is shown in Figure 2-3.

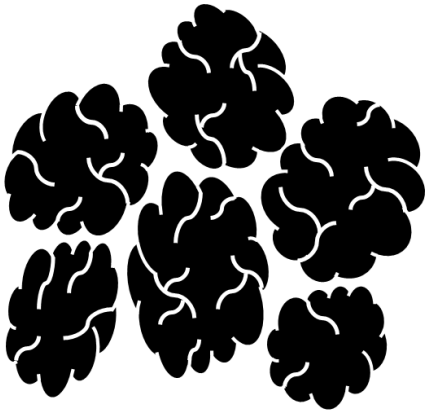

Figure 2-3. Diagram of porous carbon material showing channels between carbon particles as well as porosity within each particle.

One consideration that should be made when making carbon electrodes is that firmly compacting a carbon powder will decrease the space between carbon particles,

increasing the resistance that ions experience when navigating these channels and decreasing the material's performance at high power. Therefore, when evaluating how promising a carbon material is for EC applications, it is important to consider not only what the carbon material is, but how it was made into an electrode. In this thesis, carbon materials are studied via microcavity electrodes, as described in section "3.2.1 Microcavity Electrodes". This method involves packing loose carbon powder into an extremely small cavity, where it is held in place by friction. It is helpful to note that the performance of carbons in this setup may not be directly analogous to other electrode methods, where the carbon may be mixed with solvents or binders and is sometimes compacted at high pressures. However, this electrode set-up gives the clearest insight into the behaviour of the carbon material by itself.

In recent years, there has been a surge in literature exploring the combination of carbon materials and pseudocapacitive metals oxides for applications in ECs.[4–8] These systems could take advantage of the high-power capabilities of carbon, while increasing the energy density via pseudocapacitive Faradaic reactions. Potentially, the use of carbon as a substrate or scaffold for pseudocapacitive metal oxides could increase the stability of these materials. In the literature, there has been some exploration of how different pseudocapacitive materials perform in conjunction with carbon[5,11] and how the morphology of the carbon material affects the overall electrochemical performance.[4] However, there has been less attention regarding how other aspects of the carbon materials are influencing the electrochemical performance of these systems. Carbon materials can vary in many ways besides morphology, for example in surface area,

functional groups, and pore-size distribution, to name a few. For example, how surface functional groups of carbon may affect the stability of electrodeposited manganese oxide would be of particular interest to the EC field. The goal of my research is to shed light on how various aspects of carbon materials influence the performance of electrochemical systems combining carbon and pseudocapacitive transition metal oxides, for applications in ECs.

2.2 Electrolytes for Electrochemical Capacitors

There are many different electrolytes used in the literature and in industry for EC systems. Organic electrolytes are used in many commercial ECs due to their high voltage window (leading to higher energy storage capacity) and good stability, particularly at a range of temperatures.[28,29] This thesis, however, will utilize aqueous electrolytes, which are extremely common in EC literature in part due to their low cost and relative safety to handlers and the environment. Aqueous electrolytes also offer high conductivity compared to non-aqueous electrolytes,[28] allowing for better performance at high power, which may be critical in some applications.

In Chapter 4, some of the carbon electrochemistry was performed in 1 M H_2SO_4 electrolyte. This electrolyte was chosen due to its excellent conductivity,[28] allowing us to optimize the fast-rate performance of the carbons studied in conjunction with Elcora Advanced Materials, as part of an NSERC Engage grant. Additionally, this proton-rich electrolyte allows us to detect and monitor redox-active surface functional groups on the carbon materials, such as quinone groups (Figure 2-2). However, the pseudocapacitive

material studied in this thesis, manganese oxide, is unstable in acidic electrolytes. Therefore, much of the data in Chapters 4, 5, and 6 are collected using a neutral-pH aqueous electrolyte: 0.5 M Na_2SO_4.

2.3 Cyclic Voltammetry

To evaluate how promising a material may be for EC applications, one generally begins by evaluating if the material exhibits a capacitor-like response in electrochemical experiments. For example, in cyclic voltammetry the potential of the working electrode is cycled between two limits at a constant rate (Figure 2-4a), while the current is recorded. The rate at which the potential is changed is known as the "sweep rate" (typically given in units of millivolts per second). During a cyclic voltammogram (CV), an ideal capacitor operates at a constant positive current as the potential is increased, and then immediately switches to a negative current of equal magnitude as the potential is decreased (Ideal capacitor, Figure 2-4b). Many materials that are appropriate for ECs exhibit a similar rectangular-shaped profile in cyclic voltammetry experiments ("Carbon", Figure 2-4b). However, CVs of real systems tend to deviate slightly from the ideal shape of a perfect rectangle. This is seen at the potential extremes of the "Carbon" CV in Figure 2-4b. Here, there are areas where the current is significantly larger than the rectangular baseline. Areas like these are often attributed to oxidation (for positive currents) or reduction (for negative currents). Note that there are also regions at the potential extremes where the current is smaller than the rectangular baseline. This always exists to some extent due to resistance in the system, which causes a loss in energy when the potential sweep changes

direction. Minimizing this resistance is especially important for EC systems, as this loss in energy is higher at the faster rates typical of EC applications.

In carbon materials that have pseudocapacitive redox-active surface functional groups, there can also be noticeable peaks above the rectangular baseline, as seen by the mirror-image peaks in Figure 2-4b ("Carbon with redox reactions"). Note that this results in a mostly rectangular CV (due to double-layer charging) with the addition of peaks on top (due to the pseudocapacitive Faradaic reactions). While redox-active surface groups like quinones are known to cause these kinds of peaks in carbon CVs, note that it may be possible for other redox-active species (such as a redox-active contaminant) to cause similar profiles.

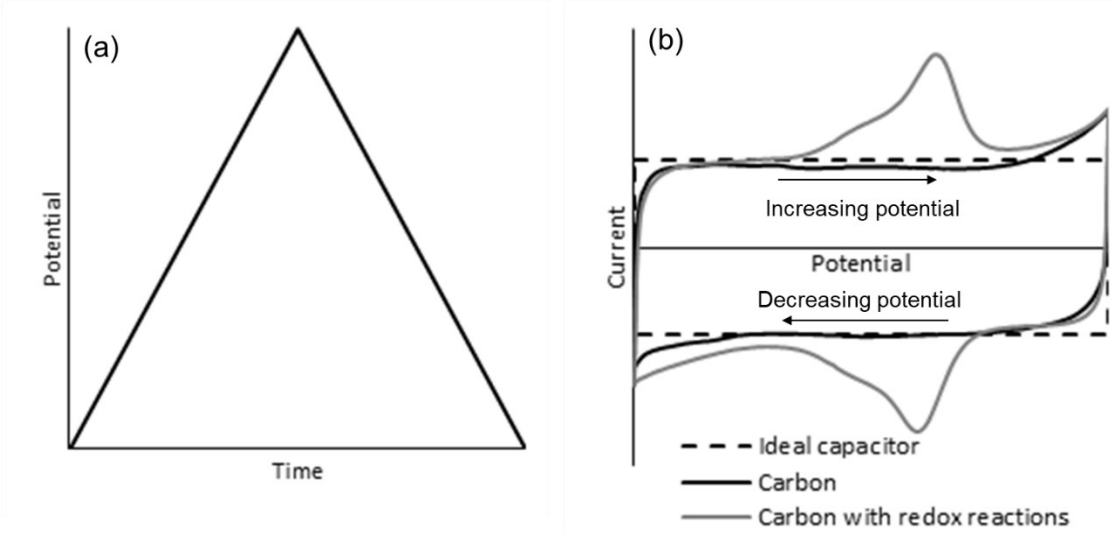

Figure 2-4. (a) Applied potential during a CV and (b) the current response of an ideal capacitor, carbon electrode, and carbon electrode with redox-active functional groups.

Pseudocapacitive materials ideally present a rectangular CV shape, like that of "Carbon" in Figure 2-4b. However, because pseudocapacitive materials primarily store

energy via Faradaic reactions, it is also common to see peaks in their CVs.[9,11,12] For a material to be considered pseudocapacitive, the oxidation peaks (positive current) and reduction peaks (negative current) should be a mirror image of one another. The peaks should also maintain this mirror-image appearance at rates that are appropriately fast for the material's intended application. Note that there are many Faradaic reactions that result in CV peaks, but whose peak positions for oxidation and reduction occur at significantly different potentials. This peak separation indicates that the redox reaction in question is not kinetically fast enough to be considered appropriate for EC applications. Conversely, the oxidation and reduction peaks associated with carbon surface functional groups in Figure 2-4b ("Carbon with redox reactions") often present as a mirror image and would therefore be kinetically fast enough to be considered supplemental energy storage in an EC application.

2.3.1 Methods for Normalizing Cyclic Voltammograms

Like with many techniques, it is sometimes important to normalize cyclic voltammetry data in order to compare and contrast different samples. CVs are typically plotted as the current response versus the applied potential. The area under this CV curve is proportional to the amount of charge stored and released by the system. Therefore, the size of the cyclic voltammogram will depend on the amount of active electrode material, where more material increases the amount of charge being stored and released, increasing the size of the CV. A common way that this is accounted for is by dividing the current by mass or moles of electrode material. The method is used to normalize CVs of full-cell EC

devices in Section “4.4 Full-Cell Electrochemical Capacitor Devices”, since the mass of carbon in the electrodes is known. Here, the current is divided by the smallest mass electrode in these symmetric coin cells, since this would be the limiting electrode in the system.

However, work in this thesis commonly employs the use of a microcavity working electrode (the setup of which is outlined in “Section 3.2.1 Microcavity Electrodes”). A benefit of using this type of electrode to study carbon materials is that no binder is required. This is important as the impact of binders on carbon electrochemistry and surface functionalities is not well-established. Additionally, only a very small amount of sample is needed. However, this electrode setup uses such a small amount of sample that it cannot be weighed accurately. If data must be normalized in this type of electrode system, it must be done another way. Because carbon-based EC materials mainly store charge via the electrochemical double-layer, their CV size is mainly impacted by surface area. However, having different sized CVs can sometimes make it difficult to compare other features in the graph, such as peaks from carbon surface functional groups that are redox-active. Conveniently, because we know that the rectangular portion of these CVs is associated with double-layer charging, we can divide the CV by the current in flat regions to effectively normalize the CV to the electrochemical surface area. This technique is employed in “4.2.1 Redox-Active Surface Functional Groups” and allows us to compare the size of redox peaks for different samples and electrode conditions. Thus, we can evaluate if redox-active species are more abundant (or at a higher surface concentrations) under certain conditions.

Another parameter that can impact the size of a CV is the sweep rate; changing the potential more quickly requires moving charge more quickly and thus increases the current. Performing cyclic voltammetry at different sweep rates can be useful in evaluating the rate capabilities of EC materials. However, because the measured current increases at faster sweep rates, it can be helpful to normalize the current by dividing by the sweep rate of the CV (i.e., the change in potential over time). This results in capacitance, as is given by equation 2 (where C is the capacitance, I is the current, and υ is the sweep rate of the cyclic voltammetry experiment).

$$(2)\ C = \frac{I}{\upsilon}$$

For any material, there is a limit to how quickly charge can be moved. However, even different portions of an electrode may have differing rate capabilities. For example, when testing increasing sweep rates, one would expect the depths of long skinny pores to become inaccessible earlier than the surface of a material, which does not have the same resistive impediment to charge movement. After normalizing the CV data by dividing by sweep rate (as is done in "4.2.3 Rate Capabilities" and all CV sweep rate experiments in Chapter 6), a loss in active material at fast rates can be confirmed by an observed decrease in the overall capacitance.

2.4 Electrochemical Impedance Spectroscopy

Frequently, EC materials are evaluated using electrochemical impedance spectroscopy (EIS) to evaluate the resistance and capacitance in the system. In EIS, a

sinusoidal potential perturbation with a known amplitude (E_0) is applied to the working electrode (Figure 2-5a). Then the sinusoidal current response or the system is measured (Figure 2-5b). Depending on the nature of the electrochemical system (e.g., capacitive process, resistive process, etc) and its magnitude, the current response will have a particular phase shift (Φ) and amplitude (I_0) (shown in Figure 2-5b). The sinusoidal potential perturbation is applied at a range of frequencies, and because of the known frequency dependence of different electrochemical features (e.g., capacitive versus resistive), the processes responsible for the electrochemical behavior can be inferred and quantified.

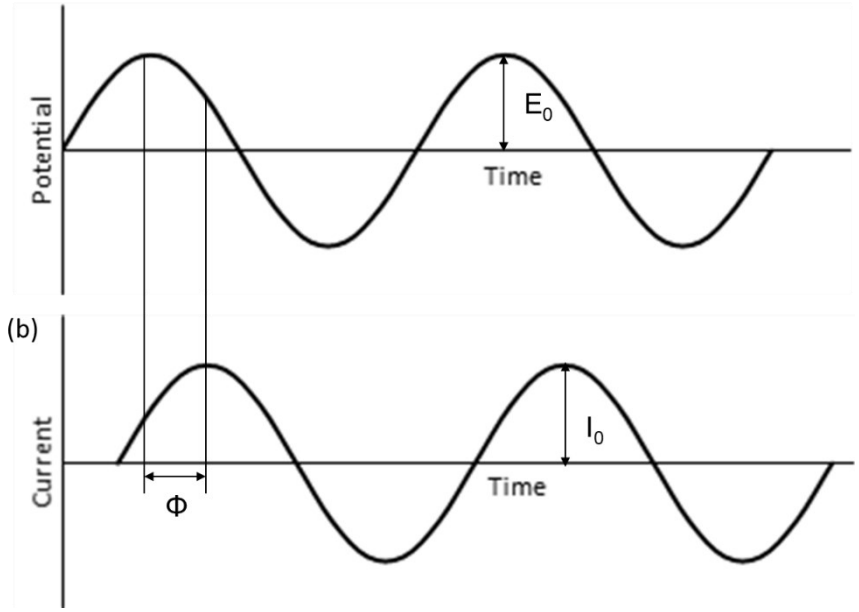

Figure 2-5. (a) Applied potential perturbation during an EIS measurement and (b) an example of the current response.

The impedance (Z) of a system is defined as the ratio of the input signal to the output signal (equation 3), where t is the time, ω is the angular frequency, E_0 is the

amplitude of the applied voltage perturbation, and I_0 and Φ are the amplitude and phase shift of the current response, respectively. This can also be expressed in terms of complex numbers, as is described by equation 4.[30]

$$(3)\ Z = \frac{E_0 \sin(\omega t)}{I_0 \sin(\omega t + \Phi)}$$

$$(4)\ Z = \frac{E_0}{I_0}(\cos\Phi + j\sin\Phi)$$

This separation of the impedance into real and imaginary components is particularly useful, as certain aspects of the electrochemical system may have real or imaginary components. For example, to determine the impedance expression of a resistor, we first need to consider Ohm's Law (equation 5), which states that the potential (E) is equal to current (I) times resistance (R).

$$(5)\ E = IR$$

For a given electrochemical system, the resistance (R) is going to be a non-zero constant. If we are applying a sinusoidal potential perturbation, we can see from equation 5, that the current will be at a maximum when the potential is at a maximum (and a minimum when the potential is a minimum). This is depicted in Figure 2-6.

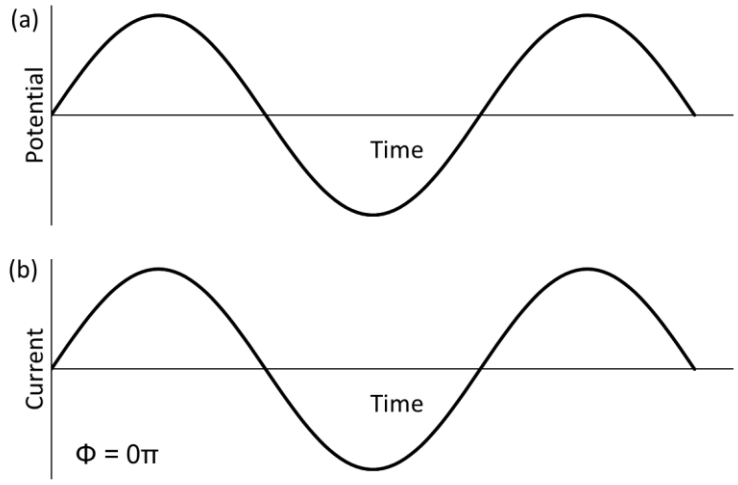

Figure 2-6. (a) Applied EIS potential perturbation and (b) current response for a resistor.

We can see from Figure 2-6 that the sinusoidal potential input and current output are completely in phase, giving resistors a phase shift (in radians) of 0π. When inserting this phase shift (Φ) into equation 4, the cosine component goes to one and the sine component goes to zero. This means that resistors only have a real component to their impedance. From this we can get the impedance expression for a resistor, using Ohm's Law (equation 5) to write the expression in terms of resistance (R). This is shown in equation 6.

$$(6)\ Z = \frac{E_0}{I_0} = R$$

From this, we can see that the impedance of a resistor is simply equal to its resistance. Therefore, in EIS representations that plot the real component of impedance (such as in

Nyquist plots, which are described in section “2.4.2 Nyquist Plots”), resistance can be directly read from the real impedance axis.

Because EC systems tend to have a capacitor-like electrochemical response, a capacitor is another important element to consider. Capacitance was described in a previous section by equation 2, where capacitance is equal to current divided by a CV sweep rate. Because a sweep rate is the change in potential over change in time, we can re-express this via equation 7, where current (I) is equal to capacitance (C) times the change in potential (dE) divided by the change in time (dt).

$$(7)\ I = C\frac{dE}{dt}$$

We can see from this equation that an EIS current response is going to be at a maximum when the potential is changing at a maximum rate. In terms of a sinusoidal EIS current response, this means we can expect current maxima where the slope of the input potential wave is greatest. Similarly, minima in the current are expected to occur when the potential wave is at its greatest negative slope and the current will be zero when the slope of the potential wave is zero (i.e., at potential maxima or minima). This is shown visually in Figure 2-7.

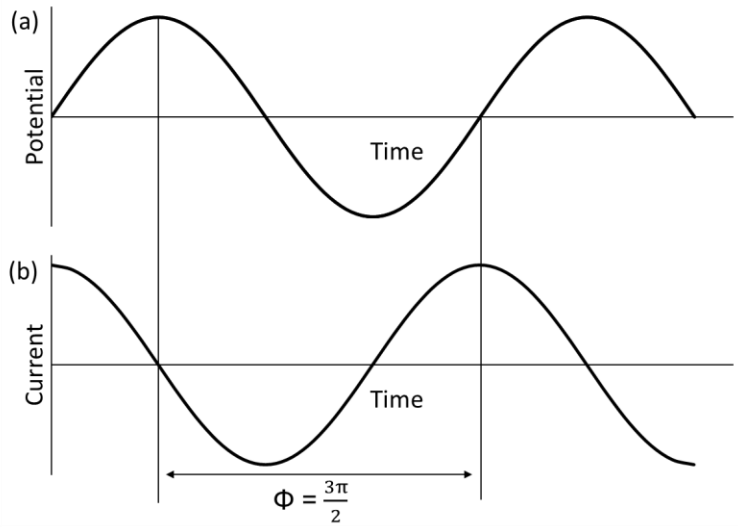

Figure 2-7. (a) Applied EIS potential perturbation and (b) current response for a capacitor.

In comparing the potential input and current output waves in Figure 2-7, we can see that the EIS phase shift for a capacitor is 3π/2. When inserting this phase shift (Φ) into equation 4, the cosine component goes to zero and the sine component goes to negative one. This means that capacitors only have a negative imaginary component to their impedance.

The definition of capacitance (C) is that it equals charge (Q) over potential (E). This is shown in equation 8. Since we know that current (I) is the flow of charge over time, we can re-express this equation in terms of these variables. Additionally, because capacitance is time dependent, it will be a function of the time-related parameter in EIS measurements: the angular frequency of the applied potential perturbation, represented by ω. Knowing that frequency is inversely related to time, we can write an expression for capacitance as shown at the end of equation 8.

(8) $C = \frac{Q}{E} = \frac{It}{E} = \frac{I}{E\omega}$

After inserting the EIS phase shift of a capacitor into equation 4 and using the expression in equation 8 to substitute potential and current, we get the equation for impedance of a capacitor, as is given in equation 9.

(9) $Z = \frac{1}{C\omega}(-j)$

In addition to always being negative and imaginary, you may note from equation 9 that the impedance of a capacitor is inversely proportional to its capacitance. This means that a material with higher capacitance will have negative impedance values that are smaller in techniques such as Nyquist plots (which are described in section "2.4.2 Nyquist Plots").

2.4.1 Equivalent Electrical Circuit Models

Circuits composed of resistors and capacitors can be used to model the EIS of materials for ECs. For example, a material that has exclusively capacitive properties could be modeled by an ideal capacitor (circuit 1, Figure 2-8). However, all electrochemical systems feature some non-zero resistance due to the resistivity of the electrolyte and electrode material. This can be modelled by adding a resistor in series with a capacitor (circuit 2, Figure 2-8). In some cases, electrodes have substantial resistance across an interface between two materials. This can be modelled by the addition of a resistor and capacitor in parallel (circuit 3, Figure 2-8). This behaviour can be due to electron transfer (which has an associated resistance) across the electrode-

electrolyte interface due to Faradaic reactions at the electrode surface. However, this behaviour can also be caused by substantial resistance between the electrode material and its current collector. The EIS result of these three circuits can be best understood by considering their Nyquist plots, which will be described in the next subsection.

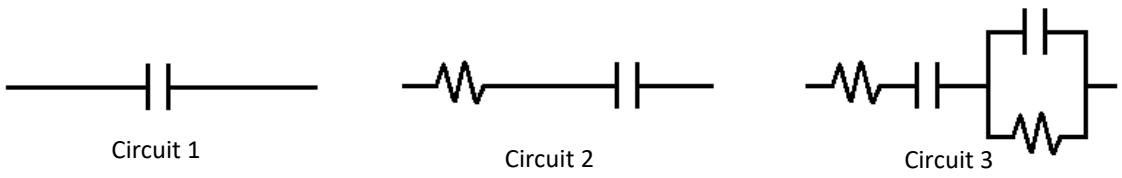

Figure 2-8. Model circuits for a pure capacitor (circuit 1), a capacitor with equivalent series resistance (circuit 2) and a capacitor with equivalent series resistance and resistance at an interface (circuit 3).

In addition to resistors and capacitors, two other circuit elements that will be discussed in this thesis are constant phase elements and Warburg elements. In real electrochemical systems, which usually have surface roughness and variations in surface chemistry, capacitive processes often do not behave like ideal capacitors. Constant phase elements are used in the place of capacitors in circuits to model these imperfect capacitive processes in EIS data. The constant phase element is able to model certain time constant distributions for capacitive processes and is typically given in units of F $s^{(n-1)}$), where F is Farads, s is seconds, and n is a fitted constant between 0 and 1. The value of n is indicative of how closely the system is to the behaviour of a true capacitor, where an n-value of 1 is an ideal capacitor and 0 is an ideal resistor.

Warburg elements are commonly employed in circuit models that describe Faradaic systems with semi-infinite linear diffusion. The Warburg element utilizes the

known time dependency of diffusion controlled processes to model how the impedance response changes with frequency and results in a characteristic 45° line in Nyquist plot representations, which are described in the next subsection.

2.4.2 Nyquist Plots

Nyquist plots are one representation of EIS data, where the negative imaginary component of impedance is plotted versus the real component. The Nyquist plot for an ideal capacitor with 150 mF capacitance (i.e., circuit 1, Figure 2-8) features an upright tail positioned at zero on the x-axis (circuit 1, Figure 2-9). Note here that the length of the tail is inversely proportional to the magnitude of the capacitance (i.e., a higher capacitance would result in a shorter tail). The addition of an equivalent series resistance of 2 Ω shifts this tail to the right (circuit 2, Figure 2-9). Note that the x-axis intercept is equal to the value of the equivalent series resistance of 2 Ω. The addition of a resistance of 8 Ω across an interface introduces a semi-circle to the Nyquist plot (circuit 3, Figure 2-9). The diameter of this semi-circle corresponds to the 8 Ω resistance across the interface, whereas the x-axis intercept of 2 Ω still corresponds to the equivalent series resistance (i.e., resistance from the electrode material and electrolyte).

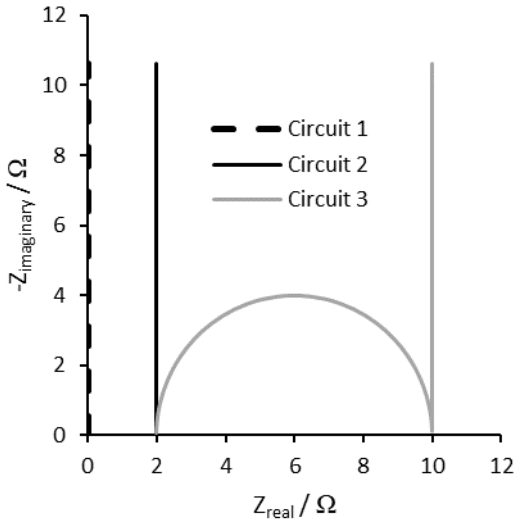

Figure 2-9. Nyquist plot of an ideal capacitor with some non-zero system resistance (solid) and a capacitive material with the addition some electrochemical process causing a semi-circular feature (dashed).

For carbon materials, the Nyquist plots generally approximate the straight line observed in Figure 2-9 (circuit 2). However, the porosity of carbon materials can sometimes influence the EIS data. Because of the resistance within pores, high frequency perturbations are not able to fully access the surface area of the material. Nyquist plots of porous materials can therefore present curvature or a change in slope at high frequencies (i.e., close to the x-axis). For example, cylindrical pores result in a 45 degree section followed by an upright tail, where the length of the 45 degree section becomes longer for more resistive pores.[31] Sometimes carbon materials also present semi-circular features in their Nyquist plots (like that of circuit 3 in Figure 2-9). In studies of carbon EC materials, it is widely recognized that these semi-circles are often caused by resistance between the carbon material and its substrate.[32–34] The magnitude of these semi-circles can be

decreased by improving the contact of the electrode material, for example by roughening the metal substrate[32,34] or coating it with a conductive intermediate.[32–34]

However, when manganese oxides are evaluated using EIS, there is substantial variation in the literature data. Some researchers show significant semi-circles in the Nyquist plots,[13,35–41] while the semi-circle is absent in other results.[42] Although the origin of these semi-circles is often not addressed, researchers that do address its origin usually suggest that the semi-circle is due to "charge-transfer resistance".[13,35–41] Charge-transfer resistance is often defined as resistance at the electrode-electrolyte interface,[38–41] and is sometimes further explained by the charge transfer in manganese oxide's pseudocapacitive reaction.[13,36,37] Only one paper has suggested that contact issues with the substrate may impact the Nyquist plots of pseudocapacitive materials, but proposed this possibility for plots with multiple semi-circles.[39] It has not yet been established if single semi-circles are a result of contact impedance at the substrate or are associated with the pseudocapacitive reaction for manganese oxide. This issue will be explored in depth in Chapter 5.

2.4.3 Complex Capacitance Plots

One downside of the Nyquist plot representation of EIS data is that there is no way to tell at which frequency each of the points were collected. This means that Nyquist plots do not give us information about rate capabilities, which is an important performance metric for EC materials especially. Another impedance representation, which includes frequency information and is particularly relevant to capacitor-like

systems, is complex capacitance plots. In these plots, the real and imaginary components of the capacitance (equations 10 and 11, respectively) are plotted versus the log of the measurement frequency.[43,44]

$$(10)\ C_{real} = \frac{-Z_{imaginary}}{\omega|Z|^2}$$

$$(11)\ C_{imaginary} = \frac{Z_{real}}{\omega|Z|^2}$$

In Figure 2-10 the complex capacitance plots for a capacitive process with non-zero equivalent series resistance (i.e., circuit 2, Figure 2-8) are shown. This circuit was chosen as it best represents the EIS response from capacitive or pseudocapacitive materials.

In the real capacitance plots, at high frequencies the real capacitance is near-zero. As the frequency is decreased, the real capacitance increases, approaching a plateau at low frequencies (Figure 2-10a). This is because at very high frequencies, the instrument is trying to move charge faster than the material can respond. As the frequency is lowered, the material starts responding (first the most accessible areas like the surface, followed by harder to access areas such as pores). The capacitance value at the plateau reflects the capacitance at maximum material usage. Note, however, that figures of merit measured by alternating-current techniques like EIS are often not the same in value as figures of merit measured from direct-current techniques or other methods of characterization.[45,46] That being said, trends within or between data sets are expected to be the same regardless of technique.

When plotted versus the log(frequency), the imaginary capacitance forms a peak (Figure 2-10b). The area under this peak is proportional to the capacitance of the system but, more importantly, the position of the peak can be used to calculate the RC time constant for the capacitive process.[43,44] An RC time constant gives us a measure of how long it takes to charge a capacitor as current moves through a resistor (hence the term "RC time constant"). An imaginary capacitance peak positioned at higher frequency values is indicative of a faster time constant and the material would therefore be able to charge more quickly and would have better performance at high power.

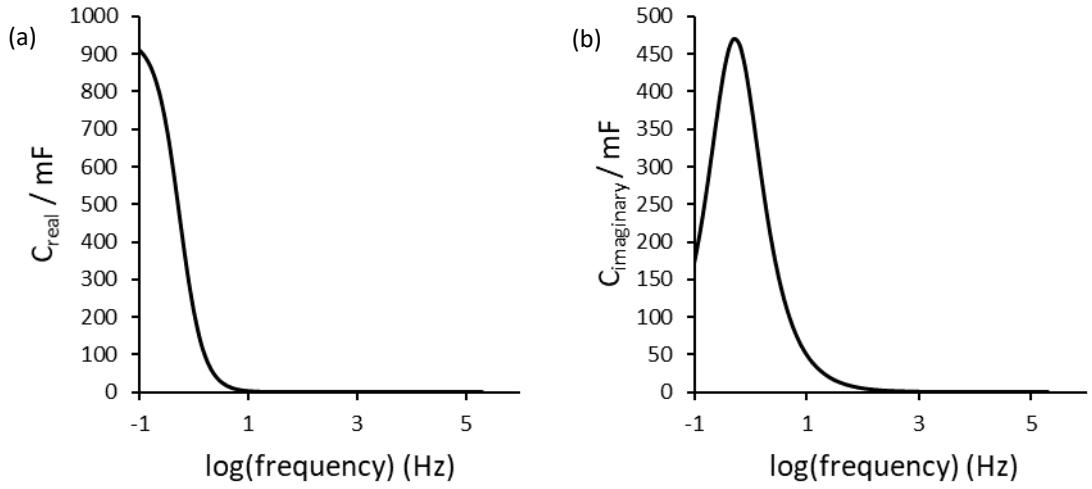

Figure 2-10. (a) Real capacitance plot and (b) imaginary capacitance plot of a capacitive system with some non-zero resistance (i.e., circuit 2 in Figure 2-8).

2.4.4 Measurement Considerations

For an EIS measurement to work properly, the relationship between potential and current must be linear. However, many electrochemical systems do not inherently satisfy this requirement. This is why the amplitude of the potential perturbation in an EIS

measurement must be very small. The logic here is that, within a very small potential window, the current response can be assumed to be approximately linear. Experimentally, one can evaluate if this assumption holds by testing multiple potential perturbation amplitudes. If the amplitude becomes too large for the potential-current relationship to remain linear, one would expect the EIS data to change (e.g., a change in the Nyquist plot, which is described in section "2.4.2 Nyquist Plots"). It is important to note that materials appropriate for electrochemical capacitors typically have an electrochemical response similar to that of a capacitor, which inherently has a linear relationship between potential and current. Therefore, the electrode materials explored in this thesis are not exceptionally sensitive to the amplitude of the applied potential perturbation in EIS.

Another underlying assumption of EIS is that the electrochemical system is stationary (i.e., unchanging) over the course of the measurement. One way to evaluate this is to run subsequent cycles of EIS to ensure there is no major change in the system between cycles. This can be done, for example, by qualitatively comparing the Nyquist plot (see section "2.4.2 Nyquist Plots") for each cycle. If it appears that the system is changing, alterations can be made in the measurement parameters, for example decreasing the frequency range to decrease the measurement time or altering the EIS measurement potential. Adjustments like these can sometimes help ensure the electrochemical system is stable over the course of a measurement.

Another, more robust way to test if an EIS measurement has satisfied its underlying assumptions is to use a measurement model to test if it is Kramers-Kronig compliant. Kramers-Kronig relations are mathematical transformations that describe the

relationship between real and imaginary impedance. If a system does not satisfy the underlying assumptions of an EIS measurement (i.e., linear current response and stationary state), then these mathematical transformations are no longer appropriate. Information that is then extrapolated from the EIS has diminished physical meaning.

Measurement models are a type of circuit model that is used to test if EIS measurements are linear and stationary. A common example of a measurement model is the Voight circuit,[47] which is comprised of a series of "Voight elements" where a resistor and capacitor are in parallel, as is shown in Figure 2-11. Recall that a capacitor and resistor in parallel is expected to make a semi-circle shape in a Nyquist plot. Therefore, we can expect the Voight circuit to result in a series of semi-circles, which can occur at a variety of frequencies and sizes, depending on the capacitance and resistance values in each Voight element. This type of circuit can, therefore, adapt to a variety of shapes in Nyquist plot data.

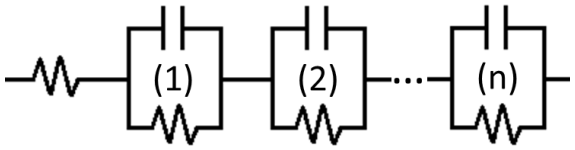

Figure 2-11. Voight circuit with "n" Voight elements.

Because Voight circuits have so many elements, one can expect that it will fit EIS data well by the way of "overfitting". Discrepancies between the EIS data and fitted circuit data may therefore suggest that the EIS did not satisfy the measurement assumptions. Fitting EIS data with a measurement model like the Voight circuit can

therefore be used as a tool to evaluate if there may be issues in how EIS data was collected. This is particularly important to consider before fitting EIS data with a circuit model intended to measure specific figures of merit or validate a hypothesis for how an electrochemical system functions.

When using this measurement model method, typically the relative residuals for both the real and imaginary impedance are evaluated. If the residuals are large, it points towards violations in EIS measurement assumptions, rendering interpretations of the EIS data moot. Relative residuals errors (in percentage) are calculated as described in equation 12, where x is the value from the data and $\hat{x}$ is the fitted value for the same data point.

(12) Percent relative residual error = $\frac{x-\hat{x}}{x} * 100\%$

2.5 Physical Characterization of Materials

Investigating electrochemical behaviour is important but it is also important to be able to link the electrochemical properties of a material to its physical and chemical properties, so that EC systems can be designed thoughtfully. For instance, we know that porosity can impact surface area (affecting energy storage capacity) but can also impact power capabilities (as the depths of long, skinny pores are unable to respond at fast rates). We also know that surface chemistry can impact things like wettability[22–24] and redox activity[18–20] in carbon materials. However, it is not currently known how these physical characteristics might impact the performance of an electrode combining carbon and a

pseudocapacitive material like manganese oxide. These characteristics will be particularly important to consider in Chapter 6, when these materials are combined.

2.5.1 Scanning Electron Microscopy

Scanning electron microscopy (SEM) can generate images of a material's surface through detection of electrons that are ejected from the valence level of atoms in the sample after bombardment with an electron beam. The electrons are ejected only from atoms near the sample's surface and the origin of the ejected electrons can be inferred by the detector, allowing an image of the sample's surface to be constructed. This can provide qualitative insight into the morphology and particle size of a material. Since we know that porosity can impact a material's performance at fast rates (as charging down pores is more difficult), this technique can give us insight into why the rate performance of different carbons may vary. Additionally, because in this thesis we control the amount of manganese oxide deposited on electrodes, it will be important to consider the morphology of carbons in Chapter 6. We can imagine that the manganese oxide might deposit thinner or thicker, depending on the carbon substrate, and we know that film thickness can impact rate performance.

2.5.2 Energy Dispersive X-Ray Spectroscopy

Energy dispersive X-ray spectroscopy (EDS) is a technique used for elemental analysis of a sample. This technique uses an electron beam to excite core electrons, allowing electrons in outer shells to relax down to fill the resulting electron hole. This electron relaxation results in the release of excess energy in the form of X-rays. Because

each element has a distinct set of energies between orbitals, it will also have a distinct set of X-ray frequencies it can emit during EDS. This allows for the identification of elements in a sample, as well as their proportional abundance. This technique is of particular importance in section "4.2.2 Unstable Redox Species in Elcora Carbon", where we attempt to evaluate if redox species seen in carbon CVs are from redox-active surface functional groups or a contaminant.

2.5.3 X-Ray Photoelectron Spectroscopy

X-ray photoelectron spectroscopy (XPS) can give insight into the chemical composition of a material's surface via detection of core electrons ejected from the sample due to excitation by applied X-rays. The binding energy (E_{BE}) of the ejected electrons can be calculated as follows (where $h\nu$ is the energy of the incident X-rays, E_k is the kinetic energy of the ejected electrons, and W is the work function of the material):

(13) $E_{BE} = h\nu - E_k - W$

Generally, the counts per second (CPS) of ejected electrons is plotted versus the binding energy. Because different chemical environments result in different binding energies, this type of plot can be used to infer the chemical nature of the sample. For example, in XPS of the carbon 1s orbital, different carbon surface functional groups will result in peaks at different binding energies. Therefore, the measured peak can be fit with peaks corresponding to these different surface functional groups in order to calculate the relative amounts of these groups on the surface.[20,21] This will help us understand how the

surface chemistry of different carbons may vary, giving us insight into redox activity seen on different carbons (Chapter 4) and carbon performance with manganese oxide (Chapter 6). In addition, an XPS survey scan can help identify signals from different elements, providing insight into the relative amounts of different elements that make up the sample's surface. Like with EDS, this helped us evaluate whether redox species seen in carbon CVs are from redox-active surface functional groups or a contaminant (as is explored in section "4.2.2 Unstable Redox Species in Elcora Carbon").

Chapter 3: Experimental

3.1 Physical Characterization Techniques

3.1.1 Scanning Electron Microscopy

Scanning electron microscopy (SEM) images were collected under the guidance of Dr. Patricia Scallion (Dalhousie University, Department of Mechanical Engineering) using a using a Hitachi S-4700 cold field emission scanning electron microscope under high-vacuum. A 3.0 kV accelerating voltage was used for images of manganese oxide films, whereas 12.0 kV was used for images of the carbon materials. Manganese oxide samples on metal foils (presented in Chapter 5) were mounted into a stainless steel mount using copper fasteners to ensure electrical connection. The carbon powder samples were mounted onto stainless steel mounts using silver paint as a conductive adhesive. Samples prepared with conductive graphite rods (McMaster-Carr, ⅛") presented in Chapter 6 were mounted vertically in a tube-shaped stainless steel mount with screws to secure the rod.

3.1.2 Energy Dispersive X-Ray Spectroscopy

Energy dispersive X-ray spectroscopy (EDS) was performed for some of the carbon powder samples during SEM measurements using an Oxford Instruments energy dispersive X-ray spectrometer and INCA software. The accelerating voltage was 12.0 kV for these EDS measurements, like with other carbon data collected via the SEM instrument.

3.1.3 X-Ray Photoelectron Spectroscopy

X-ray photoelectron spectroscopy (XPS) was performed by Andrew George (Technician, Dalhousie University, Department of Physics and Atmospheric Science) using a Thermo VG Scientific Multilab ESCA 2000 spectrometer with a CLAM4 MCD electron energy analyzer. The X-ray source was from Mg Kα rays (1253.6 eV, spot size 0.6 mm in diameter) with a pass energy of 30 eV. The XPS data were collected at room temperature and pressures between $9.5*10^{-10}$ to $7.0*10^{-9}$ torr.

Fittings of the C 1s orbital are completed in section "4.1.3 X-Ray Photoelectron Spectroscopy". Fitted peak positions were constrained based on known literature values for sp2 carbon,[48–50] sp3 carbon,[51,52] C-O,[48,53,54] C=O,[48,49,55–57] COOR, [48,49,55–57] pi-pi* shakeup,[50,55,58] and carbidic carbon[59–61] (based on silicon carbide). Peak widths at half-max were constrained to be between 1 and 2 eV, unless a more specific range was indicated by the literature. The goodness of fit was evaluated by each fitting's residual standard deviation, residual plot versus binding energy, and by noting when fitted peak parameters were at the extremes of constraint ranges, as this could indicate inappropriate fitting parameters or components.

In Section "5.1.3 X-Ray Photoelectron Spectroscopy" XPS fittings of Mn $2p_{3/2}$ spectra were completed using parameters developed by Biesinger et al.[62] Of the manganese species that had well-defined fitting parameters in the literature, Mn_2O_3, MnOOH, and MnO_2 were most relevant to our electrodeposited manganese oxide films. Therefore, all three of these manganese oxide species were fitted to our XPS data. Each manganese species' XPS profile is comprised of a number of peaks, whose peak positions

were constrained with respect to the first peak and whose peak width at half-max was defined as described in the literature.[62] For simplicity, the fitted peaks for each species will be shown as one profile, rather than a series of individual peaks. Goodness of fit was evaluated in the same manner as the C 1s XPS fittings, as described in the preceding paragraph.

3.2 Working Electrode Construction

The working electrodes studied by electrochemical experiments in this thesis come in two main forms: microcavity electrodes packed with carbon powder (used in Chapter 4) and manganese oxide films on metal foil (used in Chapter 5). Chapter 6 also uses a microcavity electrode packed with carbon powder, but also features a manganese oxide film electrodeposited on the carbon surface.

3.2.1 Microcavity Electrodes

Microcavity electrodes were made in house from 250 μm platinum wires sealed in a glass tube (by Todd Carter, scientific glass blower, department of chemistry, Dalhousie University). After sealing the Pt, the glass was ground to a flat surface using 220 grit sandpaper, and then was polished smooth using 3 μm and 1 μm diamond polish (BASi PK-4 MF-2060 polishing kit), consecutively. The result is a flat glass surface with an exposed platinum wire flush to the glass surface. The microcavity was then formed by dissolving the platinum wire in 70-80 °C aqua regia for 6 hours (changing to fresh aqua regia halfway through). This results in a cavity that is 250 μm in diameter and 100 to 250 μm in depth.[63]

Carbon is packed into the cavity by pressing the glass surface firmly into a pile of carbon powder. Electrical connection to the instrument was made using nickel wires in contact with the platinum wire inside the glass tube. Figure 3-1 shows a cross section of a microcavity electrode. Note, however, that the size of the microcavity has been exaggerated in this diagram so that it can be properly visualized. In reality, the microcavity is approximately the same width as the platinum wire (i.e., 250 μm).

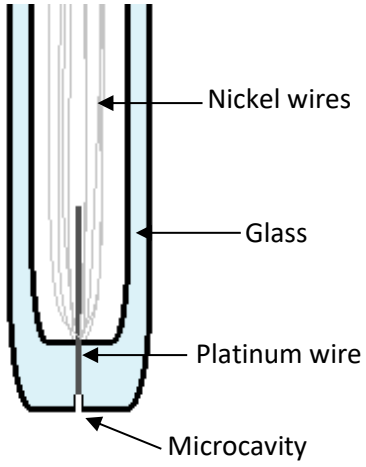

Figure 3-1. Cross section of a microcavity electrode showing the cavity into which carbon powders can be packed.

The microcavity electrodes can be reused after each experiment. This ensures that data sets can be collected using the same microcavity electrode, maintaining a constant volume of carbon powder between replicates and helping to limit the variance within a data set. In order to clean carbon powder out of the microcavity, the electrode was sonicated in distilled water for 2 minutes using a Branson 1800 sonicator. Then, to ensure the surface of the platinum was pristine, the electrode was then cleaned by cyclic voltammetry in 1 M H_2SO_4 electrolyte by cycling between -0.3 and 1.1 V vs Ag/AgCl at

a sweep rate of 1000 mV/s. Hydrogen gas evolved at low potentials during these CVs helps ensure any remaining carbon material is agitated off of the platinum surface. Cyclic voltammetry was then performed at a slower sweep rate of 100 mV/s to better evaluate if the platinum surface is clean. After cleaning the microcavity, it was dried in air briefly before packing with new carbon powder.

All carbon electrochemical data presented in this thesis (Chapters 4 and 6) were collected using a microcavity electrode, with the exception of data presented in Section "4.4 Full-Cell Electrochemical Capacitor Devices". Carbons studied in this thesis include Vulcan XC-72 (Cabot), reduced graphene oxide (Sigma Aldrich), Nanoplatelet carbon (Elcora Advanced Materials), graphene (Elcora Advanced Materials), 325-mesh graphite (Sigma Aldrich, > 99.99% purity), and graphite with < 150 μm particle size (Sigma Aldrich, ≥ 99.99% purity). Data from Chapter 6 also included manganese oxide electrodeposited onto the carbon in the microcavity electrode, the experimental parameters of which are described in Section "3.2.3 Manganese Oxide Electrodeposition".

3.2.2 Full-Cell Electrochemical Capacitor Carbon Electrodes

As part of a Mitacs/NSERC-Engage Grant partnership with Elcora Advanced Materials, symmetric coin cells were created in order to evaluate the performance of Elcora's carbon materials in full-cell EC devices. Under the supervision of James Lanigan at Elcora Advanced Materials, there were various attempts made to create

carbon electrodes that performed well in these cells, as is later discussed in Section “4.4 Full-Cell Electrochemical Capacitor Devices”.

Initially, carbon slurries were made with a 94:3:3 mass ratio of Elcora’s nanoplatelet carbon, carbon black, and polyvinylidene fluoride (PVdF) binder and approximately a 3:1 mass ratio of n-methyl-2-pyrolidone (NMP) to solid. The inclusion of carbon black is common practice in the fabrication of graphite anodes in batteries as a means to improve the overall conductivity of the electrode. However, in our system, the carbon black was agglomerating and was therefore not serving its intended purpose. Because there was no observed difference in conductivity of EC electrodes made with or without carbon black, this was excluded from the fabrication protocol. For data presented in this thesis the carbon slurries were made from a 96:4 mass ratio of carbon to PVdF binder mixed with NMP in a 3:1 mass ratio of NMP to solid. The slurry was then coated onto copper foil and dried at 55 °C. Electrodes were made by punching 16 mm diameter disks out of the sheet.

Note that some electrodes were made with compressed carbon coatings that were fed through rollers that applied pressure and heat (50 °C). Additionally, some electrodes were removed from their copper foil backings by dipping them in concentrated formic acid. These carbon electrodes were then soaked in de-ionized water before placing it directly on the cell hardware (one electrode on the spacer and one on the coin cell casing, see Figure 3-3) and drying at 55 °C. These variations in electrode fabrication will be indicated as necessary in Section “4.4 Full-Cell Electrochemical Capacitor Devices”.

3.2.3 Manganese Oxide Electrodeposition

Manganese oxide was potentiostatically electrodeposited at 1.02 V vs Ag/AgCl in 0.2 M $MnSO_4$ (deaerated with N_2 gas), at 55-60 °C. A platinum gauze acted as the counter electrode and a Ag/AgCl (1 M KCl filling solution) acted as the reference electrode.

In Chapter 5, manganese oxide was electrodeposited onto metal foil substrates. This substrate was either stainless steel foil (grade 304, McMaster-Carr, cleaned with de-ionized water, methanol, and de-ionized water, consecutively), or platinum foil (cleaned electrochemically by cyclic voltammetry in 1 M H_2SO_4), as is specified in each relevant section. These metal foils were sealed with Parafilm to produce a 1 x 3 cm deposition area (6 cm^2 total geometric area) and were thoroughly rinsed before and after electrodeposition. In Chapter 5, the amount of manganese oxide deposited onto each substrate was controlled by the amount of charged passed (1600 mC for the total electrodeposition). Additionally, there were a number of different types of manganese oxide films studied in Chapter 5. Films denoted as "wet" were stored in 0.5 M Na_2SO_4 after electrodeposition. "Dry" films were heat-treated at 200 °C for 2 hours and stored in air. Hybrid films were made by depositing an initial layer of manganese oxide, which was dried under the same conditions as the "dry" films, followed by a second deposition of manganese oxide, after which the electrode was stored in 0.5 M Na_2SO_4 (like the "wet" films). The total amount of charge passed during electrodeposition of hybrid films remained 1600 mC, but the ratio of charge used to deposit the initial "dry" film versus the second "wet" film was varied. In this thesis, the data labels used for hybrid films indicate

the ratio of charge passed in the deposition of each film layer. For example, "10dry:90wet" films have an initial 10% layer (160 mC electrodeposition) that underwent heat-treatment, which was followed by the electrodeposition of the remaining 90% of the film (1440 mC electrodeposition) and wet storage. Note that these hybrid films therefore have a manganese oxide – current collector interface similar to the dry films, but the surface of the film is hydrous like the wet films. To help visualize these hybrid films, Figure 3-2 shows cross sections of "wet", "dry", and "10wet:90dry" films. In addition to the "10dry:90wet" films, dry:wet manganese oxide ratios of 1:99, 5:95, 25:75, 50:50, and 75:25 were studied in Subsection "5.2.2 Interfacial Resistance in Other Dry:Wet Ratio Films".

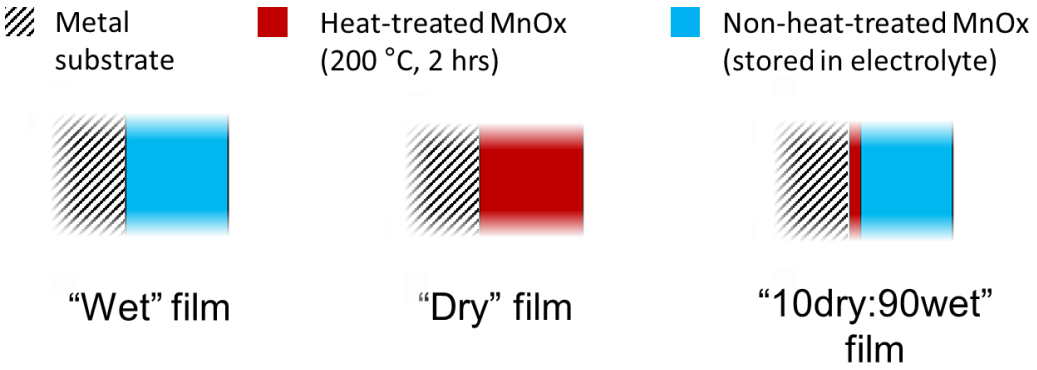

Figure 3-2. Cross sections of different types of manganese oxide films on metal substrates, showing heat treated ("dry") and non-heat-treated ("wet") manganese oxide layers.

In Chapter 6, manganese oxide was electrodeposited onto carbon materials using the same type of deposition cell and potential as in Chapter 5, as was described in the preceding paragraph. However, manganese oxide electrodepositions in Chapter 6 were carried out at room temperature rather than the 55-60 °C used for electrodes in Chapter 5.

Some of the electrodepositions in Chapter 6 were controlled by charge passed but others were controlled by time, as will be explicitly stated throughout Chapter 6. Pulsed electrodepositions used in Section "6.2 Manganese Oxide Electrodeposition on Carbon Substrates" consisted of one second holds at the electrodeposition potential with five second open-circuit rests in between each hold. Other time-controlled electrodepositions used in Chapter 6 are simply un-pulsed holds at the electrodeposition potential previously specified. The exact time used for each electrodeposition will be stated in each relevant section. Before manganese oxide electrodeposition, carbon powders were packed into microcavity electrodes, as described in section "3.2.1 Microcavity Electrodes". After electrodeposition, these electrodes were soaked for two minutes each in three vials of de-ionized water, in order to allow any Mn^{2+} ions that may remain in the pores of the carbon to diffuse out of the electrode. The microcavity electrodes were re-used after each experiment and were cleaned in the same way as described in section "3.2.1 Microcavity Electrodes".

3.3 Experimental Set-up for Electrochemical Experiments

Electrochemical experiments were performed in a three-electrode configuration, one-compartment cell using a Biologic VMP3 Multipotentiostat. The counter electrode for each experiment was platinum, with a surface area greater than ten times that of the working electrode. The potential of the working electrode was measured and controlled against a Ag/AgCl reference electrode (1 M KCl filling solution), whose potential is 0.22 V versus the standard hydrogen electrode (SHE). All potentials reported herein are

therefore reported versus Ag/AgCl. All electrolyte solutions were made using 18.2 MΩ·cm deionized water (from an Arium Mini Plus) and either $MnSO_4$ (purity >99.0%, Sigma Aldrich), Na_2SO_4 (>99.0% purity, Fisher Scientific), or H_2SO_4 (Caledon, 95-98% by weight, reagent grade) at the concentrations specified in each experiment. The working electrode for each experiment is specified in the relevant chapter.

3.3.1 Cyclic Voltammetry

Cyclic voltammetry of carbon electrodes presented in Chapter 4 was performed between -0.22 to 0.78 V vs. Ag/AgCl at a sweep rate of 100 mV/s. This potential range was chosen so that the same 1 V potential range could be used in both acidic electrolyte (Section "4.2 Carbon Electrochemistry in Acidic Electrolyte") and neutral -pH electrolyte (Section "4.3 Carbon Electrochemistry in Neutral-pH Electrolyte"), without major water oxidation or reduction. The number of cycles recorded varies by experiment and will be indicated in the relevant results section. In order to compare different replicates, some CVs were normalized by dividing the data by the double-layer current (i.e., the current at flat regions of the CV). Because this current is related to double-layer charging, it is proportional to the electrode surface area, meaning the CV is effectively normalized by the electrochemical surface area. Other CVs were normalized by dividing the current by mass or by sweep rate, as was previously described in Section "2.3.1 Methods for Normalizing Cyclic Voltammograms". The electrolyte used for CV data of carbon was either 1 M H_2SO_4 or 0.5 M Na_2SO_4 and will be indicated in the relevant results sections.

In Chapter 4, a cyclic voltammetry sweep rate experiment was used to evaluate rate capabilities (see Section "4.2.3 Rate Capabilities"). This experiment tested sweep rates of 10, 50, 100, 200, 400, 800, 900, 1000, 2000, 4000, 6000, 8000, and 10 000 mV/s, by recording 5 cycles at each sweep rate in this given order. A potential window of -0.22 to 0.78 V vs. Ag/AgCl was used to match other CV potential ranges used in this Chapter.

In Chapter 6, the same cyclic voltammetry sweep rate experiment was employed as described above. However, the potential window was set to 0 to 1 V vs Ag/AgCl to avoid manganese oxide dissolution that could occur with the lower potential window used in Chapter 4. Because the electrodes in Chapter 6 included manganese oxide, all of these CVs were recorded in 0.5 M Na_2SO_4 electrolyte. In Section "6.4 Carbon Surface Functional Groups' Impact on Manganese-Oxide-Containing Electrodes", CVs were used as a means to oxidize the carbon surface. To encourage this oxidation, a higher potential window of 0.02 to 1.02 V vs Ag/AgCl and acidic 1 M H_2SO_4 electrolyte were used. The electrode was then soaked for two minutes each in three vials of deionized water in order to remove acid from the carbon pores before using it for further experiments.

In Chapter 5, cyclic voltammetry of manganese oxide was performed between 0.4 to 0.8 V vs. Ag/AgCl at a sweep rate of 10 mV/s, as this smaller potential window was necessary to ensure the stability of "wet" manganese oxide films on stainless steel. All CVs of manganese oxide were performed in 0.5 M Na_2SO_4 electrolyte, and the CVs presented in Chapter 5 are the tenth CV cycle.

3.3.2 Full-Cell Electrochemical Capacitor Coin Cells

Symmetric EC coin cells were made by stacking a stainless-steel spring, stainless steel spacer, carbon electrode, separator (glass microfiber), and carbon electrode, in that order (Figure 3-3). A description of the fabrication methods for the carbon electrodes is available in Section "3.2.2 Full-Cell Electrochemical Capacitor Carbon Electrodes". Electrolyte (100 µL of 0.5 M Na_2SO_4) was added to the separator during assembly. The stack was then encased in a stainless-steel coin cell casing and compressed at 140 psi. The stainless steel components in this set-up were 316 type stainless steel.

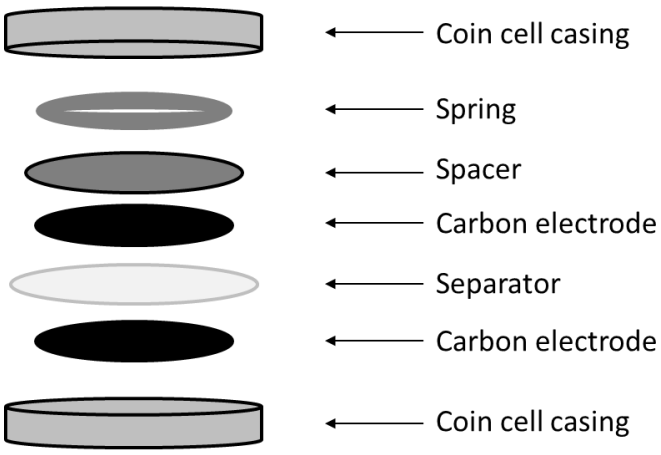

Figure 3-3. Full-cell electrochemical capacitor coin cell configuration.

3.3.3 Electrochemical Impedance Spectroscopy

In Chapters 4 and 5, EIS was measured at the open-circuit potential (i.e., resting potential) of the working electrode. In these experiments, the open-circuit potential of the working electrode was measured for 30 minutes and then set as the applied potential in the EIS measurement. However, in Chapter 6 we are studying electrodes that combine

carbon and manganese oxide, which have different open circuit potentials. Therefore, all EIS in Chapter 6 was measured at 0.650 V vs Ag/AgCl, as this is approximately halfway between carbon and manganese oxide's open circuit potentials. The EIS potential perturbation amplitude (E_0) for all EIS data in this thesis was 10 mV. Frequencies were applied from 200 kHz to 100 mHz, with ten points recorded per decade. The EIS data is presented either in a Nyquist plot representation (see Section "2.4.2 Nyquist Plots") or by plotting the real and imaginary components of the capacitance versus the log(frequency) (see Section "2.4.3 Complex Capacitance Plots"). Note that every EIS measurement in this thesis included at least three subsequent cycles, as a means to qualitatively check that the system is stationary (which is an assumption of EIS measurements, as discussed in section "2.4.4 Measurement Considerations").

3.4 Equivalent Electrical Circuit Model Fittings

In section "5.3 Considerations for Manganese Oxide Circuit Models", we fit a number of circuit models to manganese oxide EIS data. These fittings were completed using the "Z fit" tool in EC-Lab software. A randomized simplex algorithm was used to fit the circuit components to the circuit that was built and specified in the software.

Chapter 4: Carbon

Before combining carbon with pseudocapacitive materials, it is a good idea to understand carbon's properties and electrochemical behaviour. Currently it is unknown how carbon properties such as surface chemistry and porosity might impact electrode performance when combined with pseudocapacitive materials. This could be of importance, especially since we intend to grow pseudocapacitive manganese oxide on carbon by electrodeposition in order to combine these materials in Chapter 6. Additionally, while carbon electrochemistry is well-documented in acidic aqueous electrolytes, it is not as well-studied in neutral pH electrolytes. Neutral pH electrolyte will be necessary when we combine carbon with pseudocapacitive manganese oxide in Chapter 6, as manganese oxide would be unstable and dissolve in acidic solutions. Therefore, it is important we understand the electrochemical behaviour of our carbon materials in neutral pH electrolyte, as will be explored in section "4.3 Carbon Electrochemistry in Neutral-pH Electrolyte".

A number of experiments presented in this chapter were completed in order to characterize carbon materials from Elcora Advanced Materials, as part of a Mitacs and NSERC-Engage grant partnership with the company. The goal was to determine if carbon materials made by Elcora Advanced Materials might be suitable for applications in EC devices. Full-cell EC device prototypes were also made using Elcora's materials and are discussed in section "4.4 Full-Cell Electrochemical Capacitor Devices".

Four different carbon materials are studied in this chapter: Vulcan XC-72, a commercially-available carbon black; a commercially-available reduced graphene oxide; and nanoplatelet and graphene carbons received from Elcora Advanced Materials. The Vulcan carbon is typical of the type of carbon used in EC applications and is therefore used as a benchmark to which to compare the other carbon materials. Similarly, the commercially available reduced graphene oxide is used as a comparison for the graphene material produced by Elcora Advanced Materials. All carbon powders were packed into a microcavity working electrode (described in Section "3.2.1 Microcavity Electrodes") for the electrochemical experiments shown in this chapter except for the full cells, whose set-up is described in Section "3.3.2 Full-Cell Electrochemical Capacitor Coin Cells".

4.1 Physical Characterization

4.1.1 Scanning Electron Microscopy

SEM images of the Vulcan carbon and Elcora nanoplatelet and graphene carbons highlight that these materials have different particle sizes and morphology. Note that the commercially available reduced graphene oxide material was not imaged by SEM due to the extremely small amount of material available and its high cost. The Vulcan carbon has very fine particles (Figure 4-1a), compared to the nanoplatelet and graphene carbons from Elcora. The Elcora nanoplatelet carbon appears to have the largest particles and therefore the largest gaps between the carbon particles (Figure 4-1b). These large gaps between the carbon particles may be beneficial for fast-rate applications as it could allow more facile movement of electrolyte ions through the carbon material. The nanoplatelet

carbon particles tend to be flat flakes that vary in size (Figure 4-1b). By comparison the Elcora graphene carbon has a similar flake-like morphology, but in general the flakes are smaller in and more consistent in size (Figure 4-1c). We anticipate that smaller flakes will lead to smaller channels between the flakes when the carbon is made into an electrode. This would cause higher resistance to electrolyte movement through the material, decreasing the electrode performance at fast rates.

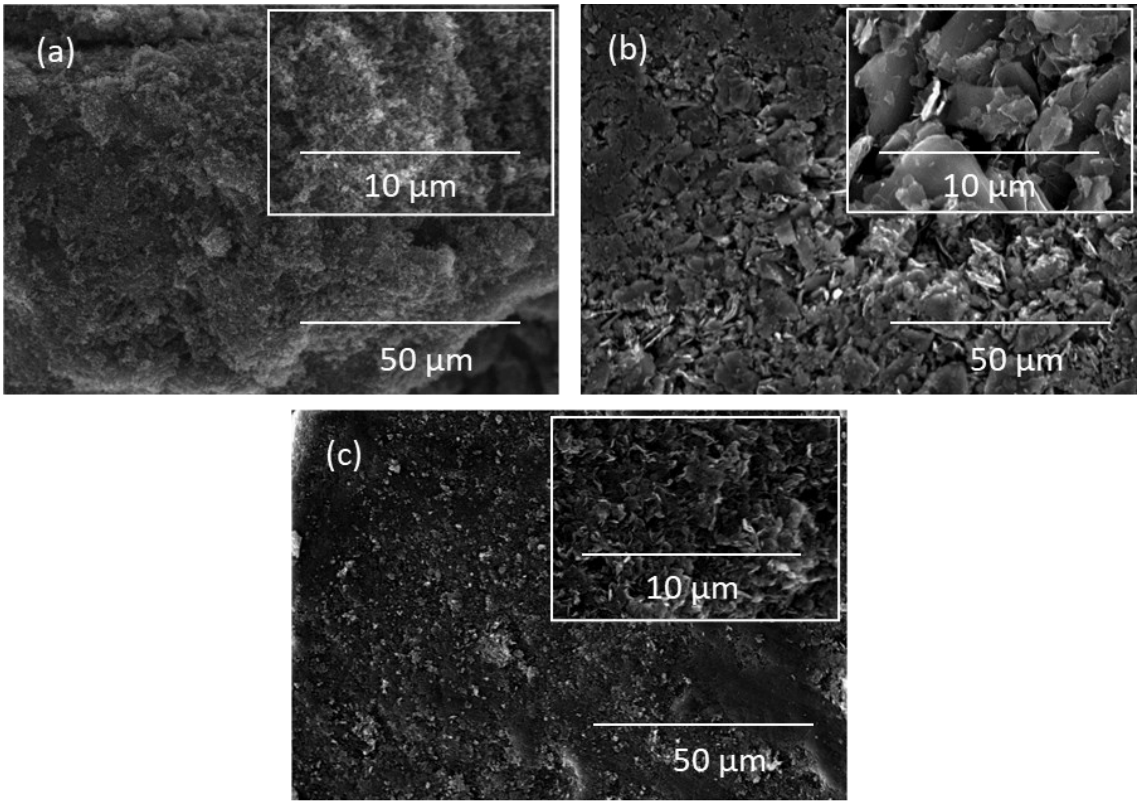

Figure 4-1. SEM images of (a) Vulcan XC-72 (b) Elcora nanoplatelet carbon, and (c) Elcora graphene at 1000 times magnification, with insets showing 5000 times magnification.

4.1.2 Electron Dispersive Spectroscopy

EDS of the Elcora nanoplatelet and graphene carbons as well as Vulcan was performed on the same samples used for SEM images. Note that the nanoplatelet and graphene carbons were both from the first batch of carbons provided by Elcora Advanced Materials, the importance of which will be discussed later in this chapter. The areas that the EDS spectra were collected from on each sample are shown in Figure 4-2. While EDS should be able to give us an elemental breakdown for our carbon samples, note that EDS sample areas are relatively small. Therefore, it is possible that EDS could fail to detect some trace elements in a sample.

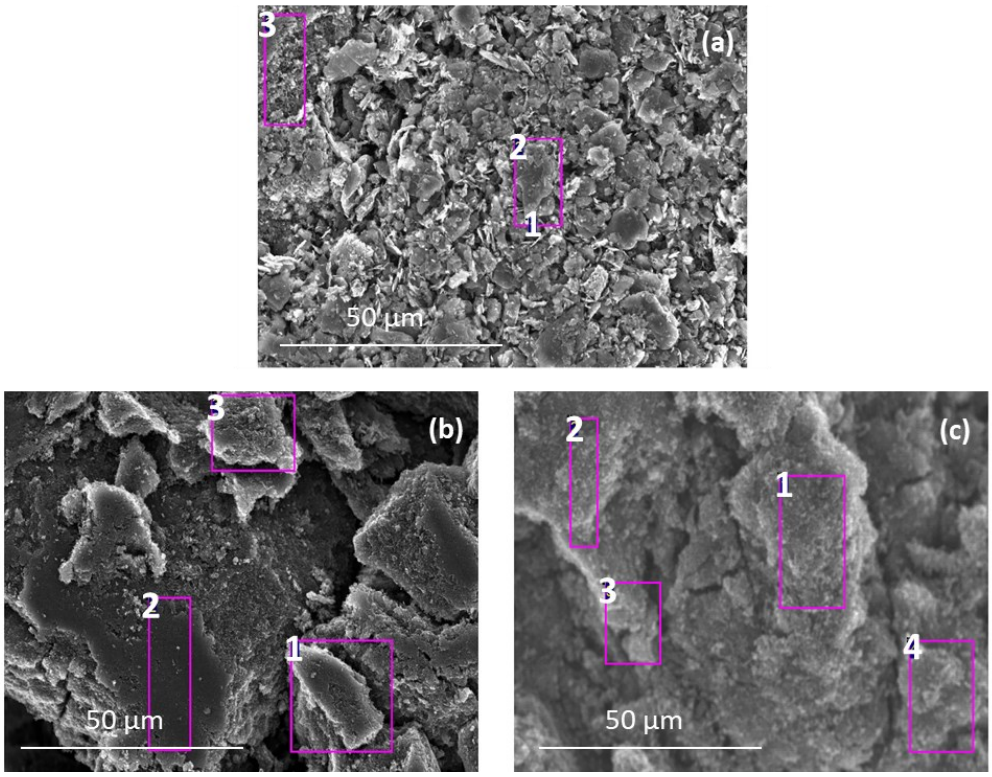

Figure 4-2. SEM images of (a) batch #1 of Elcora nanoplatelet carbon, (b) batch #1 of Elcora graphene, and (c) Vulcan XC-72 carbon showing areas where EDS was performed (note that spectrum 1 for the nanoplatelet carbon was a point-collection spectrum).

The relative amounts of each element detected in EDS were averaged for the spectra shown in Figure 4-2 and are compiled in Table 1. These carbon powders were mostly comprised of carbon with a small amount of oxygen, but trace amounts of silicon and sulfur were detected for the Elcora nanoplatelet carbon and Vulcan carbon, respectively. In both cases, the trace element was detected in all of the collected spectra. The Elcora nanoplatelet carbon and graphene did not have significantly different amounts of oxygen but the silicon that was detected in the nanoplatelet carbon was not found in the graphene sample. The fact that silicon was not detected in the other Elcora samples paired with its very low detected amount suggests that the presence of this element is not definitive. The Vulcan carbon had a comparatively lower amount of oxygen compared to the Elcora carbons and was the only carbon tested that was found to contain sulfur. The relative amount of oxygen detected on these carbons' surfaces will be helpful to keep in mind as we interpret cyclic voltammetry of these different carbons later in this chapter, since some oxygen-based surface functionalities are redox active and can play a role in the performance of the carbon material when tested electrochemically

Table 1. Relative amount of each element detected in EDS measurements, as averaged from the spectra shown in the SEM image in Figure 4-2 (note that the nanoplatelet and graphene carbons were both from "batch #1").

Carbon type	**C**	**O**	**Si**	**S**
Elcora nanoplatelets	97.7 ± 0.1	2.3 ± 0.1	0.08 ± 0.01	-
Elcora graphene	97.4 ± 0.4	2.6 ± 0.4	-	-
Vulcan XC-72	98.19 ± 0.07	1.5 ± 0.1	-	0.29 ± 0.04

4.1.3 X-Ray Photoelectron Spectroscopy

Because carbon surface functional groups can have important electrochemical responses, we used XPS to get a clearer idea of the surface chemistry of the Elcora carbon materials. X-ray photoelectron spectroscopy (XPS) data were collected for two different production batches of the Elcora nanoplatelet carbon and two different production batches of the Elcora graphene. Note that the sample labelled "Graphene 2" in this section was the only sample from Elcora that did not present an unstable redox peak in its cyclic voltammetry, as is described in section "4.2.2 Unstable Redox Species in Elcora Carbons".

The XPS survey scans detected mostly carbon and oxygen for all samples, although a small amount of beryllium was detected for one of the nanoplatelet samples (NP 1). Given the measured peak area and standard deviation for the survey scan's beryllium peak (0.9 ± 0.4) and the fact that it would be an unlikely contaminant for this material, it is likely that there is no beryllium in the sample. The only other elements detected for all four samples were carbon and oxygen; XPS did not detect trace amounts of silicon as was found from the EDS results in the previous section. Like in EDS, there was no significant difference in the relative amount of oxygen in the four Elcora carbon samples tested. The relative amount of oxygen measured by XPS was on par with that detected by EDS (Table 1).

In order to best compare the shape of the XPS C1s orbital spectra from each carbon sample, the spectra were normalized by the graphitic peak. This reveals that all four samples of the Elcora graphene and nanoplatelet carbons have extremely similar C1s

XPS profiles (Figure 4-3). This is not necessarily surprising, as these two types of carbons have similar production conditions.

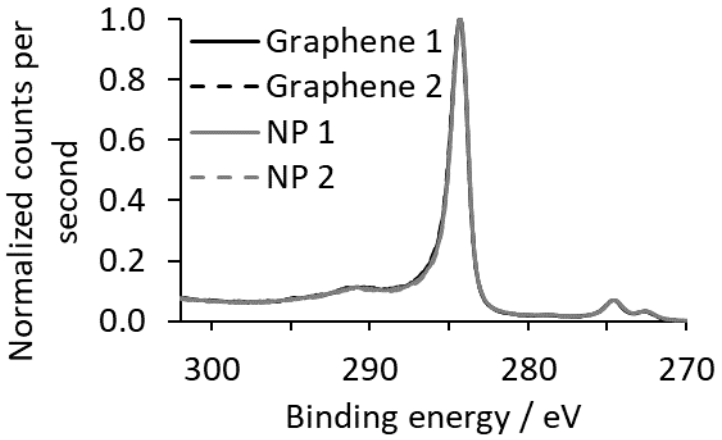

Figure 4-3. Normalized counts per second versus binding energy for XPS of the C1s orbital for two production batches of the Elcora graphene ("Graphene 1" and "Graphene 2") and two production batches of the Elcora nanoplatelet carbon ("NP 1" and "NP 2").

An example of the fittings that were performed on this XPS data is shown in Figure 4-4, with all of the fitted peaks and the resulting envelope. Details on the fitting parameters for this XPS data is described in Section "3.1.3 X-Ray Photoelectron Spectroscopy". Note that in addition to the C-O and C=O peaks that are shown in Figure 4-4, peaks associated with COOR groups were also initially fitted, but found to be negligible in all the tested carbons. COOR peaks were therefore excluded from final fittings. It was also noted that there were large fitting residuals at binding energies lower than the graphitic peak (i.e., below 284.3 eV). This would be best accommodated by a carbidic peak. The only element other than carbon and oxygen detected in Elcora carbon samples via physical characterization techniques (i.e. XPS and EDS) was silicon.

Although silicon was only tentatively detected in one Elcora carbon during EDS (see Table 1), silicon carbide was the only carbidic species that we had physical characterization data to support. The peak fitting parameters for the carbidic peak were therefore constrained based on known literature values for silicon carbide, as previously described in Section "3.1.3 X-Ray Photoelectron Spectroscopy".

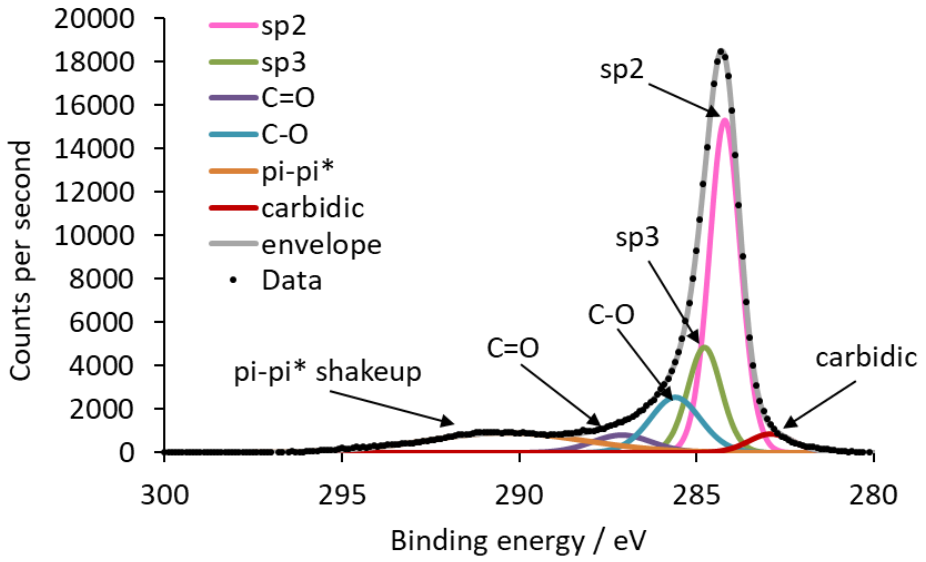

Figure 4-4. XPS C1s spectrum fitting example (for Elcora nanoplatelet carbon, batch #1), with fitted peaks labelled accordingly.

The relative amounts of the different fitted carbon environments were calculated for the four carbon samples using the peak areas from these XPS fittings. The main difference between the samples is that the graphene carbon has a higher proportion of sp^2 carbon and less sp^3 carbon compared to Elcora's nanoplatelet carbon (Table 2). There is no substantial difference in the fitted carbon surface functional groups for the two different types of carbon (Table 2, "C-O" and "C=O"). Note in particular that there is no

substantial difference in the fitted surface functional groups between the two batches of graphene. This is important because the second batch of Elcora graphene did not present "redox peak 3" in cyclic voltammetry experiments like the other Elcora carbons, as will be discussed in subsection "4.2.2 Unstable Redox Species in Elcora Carbons".

Table 2. Percent abundance of different carbon environments as calculated from C1s XPS fitted peak areas for the four Elcora carbon samples.

Elcora carbon sample	**sp^2 carbon**	**sp^3 carbon**	**carbidic carbon**	**C-O**	**C=O**
Nanoplatelet (batch 1)	56	19	5	15	5
Nanoplatelet (batch 2)	41	35	4	15	5
Graphene (batch 1)	61	13	5	15	6
Graphene (batch 2)	62	11	5	16	6

4.1.3 Surface Area

Gravimetric surface areas of Vulcan XC-72 and reduced graphene oxide used in this chapter were provided in the materials' data sheets and are approximately 250 and 450 m^2/g, respectively. As discussed in Chapter 2, higher specific surface areas are often achieved by smaller pores and while this results in higher energy storage it can also cause lower power, as will be explored in section "4.2.3 Rate Capabilities".

More important than gravimetric surface area is the electrochemically active surface area, as this is what will dictate the energy storage capacity of these carbon materials. Based on literature values relating carbon capacitance to electrochemical

surface area,[64] we can estimate the electrochemical surface areas of Vulcan XC-72 and reduced graphene oxide in our microcavity electrode to be approximately 8 and 30 cm^2, respectively. This is a larger difference than expected from the gravimetric surface areas. This discrepancy is likely due to more of the reduced graphene oxide material packing into the microcavity electrode, which will contain a consistent volume of carbon (but not necessarily a consistent mass). To compare, the Elcora nanoplatelet and Elcora graphene materials are estimated to have surface areas of approximately 6 and 15 cm^2 in our microcavity electrode, based on our electrochemical data. From this, we can see that Elcora's nanoplatelet material will be best compared to Vulcan XC-72, while Elcora's graphene material has a much higher surface area in our electrode set-up, albeit still lower than the commercially-available reduced graphene oxide.

4.2 Carbon Electrochemistry in Acidic Electrolyte

Although electrodes that combine carbon and pseudocapacitive manganese oxides would typically not be paired with acidic electrolytes (due to instability of the manganese oxide), carbon electrochemistry performed in acidic electrolyte can extract useful information. Because some carbon surface functional groups can undergo redox reactions involving protons (e.g., quinones, as described in Figure 2-2), electrochemistry in acidic electrolyte can give insight to the presence of these functional groups and how they may be changing during electrochemical experiments.

4.2.1 Redox-Active Surface Functional Groups

Different carbon materials have different surface functionalities, and those surface functionalities may also change over the course of electrochemical experiments. Redox-active surface functional groups can be desirable in carbons intended for energy storage systems as they can increase the carbon's energy density through their Faradaic reactions. For this project, it is especially important to consider that the type of surface functional groups present on a carbon (and how much they change during electrochemical experiments) may impact the connection between carbon and manganese oxide, as will be explored later in Section "6.4 Carbon Surface Functional Groups' Impact on Manganese-Oxide-Containing Electrodes". This could have the potential to influence the rate capabilities and cycle life of electrodes that combine carbon and pseudocapacitive materials like manganese oxide. Cyclic voltammetry in acidic electrolyte is a convenient way to detect redox-active surface functional groups and track how they change in real time during electrochemical experiments.

Figure 4-5 shows CVs for four different carbon materials initially (cycle 2), after a short period of cycling (cycle 50), and after 15 hours of cycling (cycle 2700). Note that all of the carbons produce a rectangular shaped CV but that some have additional peaks centered around 0.3 V. These peaks correspond to Faradaic (redox) reactions and are consistent with the potential where we would expect to see redox activity from surface functional groups like quinones in 1 M H_2SO_4 electrolyte.[20,65] It is evident from the CV of Elcora graphene (Figure 4-5c) that there are actually three different sets of redox peaks

in some CVs. These will from hereon be referred to as peaks 1, 2, and 3 as is indicated in Figure 4-5c.

Vulcan carbon initially shows negligible redox peaks indicating a low level of redox-active functional groups (Figure 4-5a). However, broad redox peaks (centered around 0.3 V) develop during the 15 hours of cycling in acid, indicating redox-active functional groups have developed over time. Note that although multiple peaks are not visible in the Vulcan CV, they occur around the same potential as the peaks 1 and 2 in the Elcora carbon CVs. These broad peaks developed in Vulcan CVs are a common occurrence in carbon electrochemistry and is typically attributed to the formation of quinone surface groups.[20,65] By comparison, Elcora's nanoplatelet carbon has much larger redox peaks at cycle 50, indicating this carbon has a higher proportion of redox-active groups on its surface (Figure 4-5b). This is consistent with EDS findings that the Elcora carbons have a higher abundance of oxygen compared to Vulcan (Table 1). The redox peaks in the nanoplatelet carbon CV do not change dramatically between cycle 50 and end of the 15 hours of cycling, indicating that the amount of these redox-active functional groups is not further increased by the electrochemical cycling. On the other hand, CVs of Elcora's graphene material also show substantial redox peaks at early cycling (cycle 50), but these peaks increase further during the 15 hours of cycling (Figure 4-5c). This indicates that the graphene also has a high proportion of these redox-active functional groups after synthesis but has the capacity to develop more of these groups during electrochemistry. As a comparison to the Elcora graphene, commercial reduced graphene oxide has much smaller initial redox peaks and, although the peaks grow in size during

cycling, they do not reach anywhere near the level of the redox peaks in in the Elcora graphene (or the nanoplatelet carbon) (Figure 4-5d). Therefore, the commercial reduced graphene oxide and Vulcan carbons have much lower proportions of redox-active surface functional groups compared to the Elcora carbons. This means that the Elcora carbons can store more energy via Faradaic reactions, increasing the energy density for a given surface area of carbon.

In addition to presenting much larger redox peaks compared to the Vulcan and reduced graphene oxide carbons, the carbons from Elcora present a third set of redox peaks that are not present in the other carbons during initial cyclic voltammetry cycles (see "peak 3" in cycle 2 of Figure 4-5b and Figure 4-5c). Peak 3 decreases and disappears during the first 50 CV cycles, suggesting that whatever is responsible for the redox peaks is unstable in the experimental conditions. This could either be due to the electrolyte (and perhaps its acidic pH) or the applied potentials during the CVs.

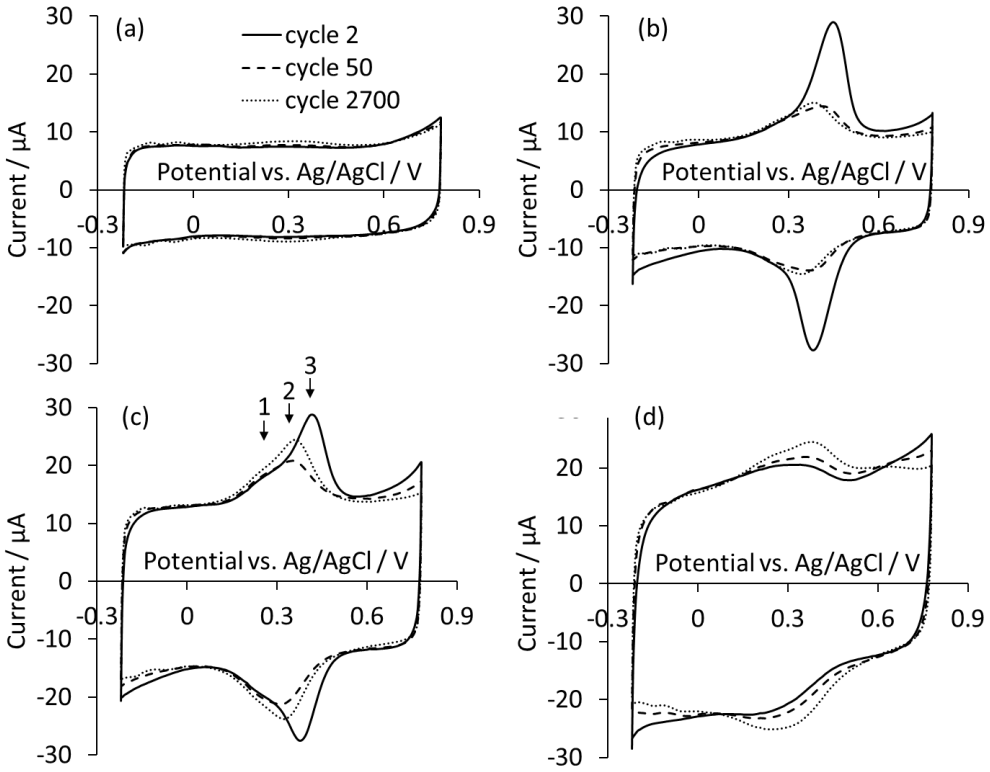

Figure 4-5. CVs at 100 mV/s of (a) Vulcan, (b) Elcora nanoplatelet carbon, (c) Elcora graphene, and (d) commercial reduced graphene oxide in 1 M H_2SO_4 electrolyte.

From these CVs, it appears that redox peaks 1 and 2 are likely due to redox active functional groups that can develop a higher abundance during electrochemistry in acidic electrolyte. This electrochemical behaviour (and the potential at which the peaks appear) is comparable to that of surface quinones.[20,65] However, the presence of two sets of redox peaks suggests that we have two distinct redox-active species in the Elcora carbons. While ortho- and para-quinones theoretically have peaks that occur at different potentials, they are not typically resolved in cyclic voltammetry experiments without chemical labelling.[19] Therefore, it is not clear whether the Elcora carbons have ortho- and para-quinones that are better resolved than most other systems, or if they have two distinct

redox-active species. Nevertheless, the presence of both these pseudocapacitive species suggests the Elcora carbon materials will have enhanced energy-storage capabilities

Redox peak 3, which is present only in the carbons from Elcora, has dramatically different electrochemical behaviour from the other peaks, disappearing completely during cyclic voltammetry experiments. Therefore, it is not clear what may be responsible for redox peak 3. If the species responsible for peak 3 is a redox-active surface functional group it could potentially contribute to the energy storage of the carbon, if it could be stabilized. However, it is also possible that peak 3 is due to a redox-active contaminant, which could potentially contaminate the electrolyte and worsen energy loss in the material through self-discharge via Faradaic reactions.[66] The origin of redox peak 3 will be explored further in subsection "4.2.2 Unstable Redox Species in Elcora Carbons".

To better study the behaviour of peaks 1 and 2, it would be beneficial to eliminate the unstable peak 3 from the Elcora carbon CVs. It is unclear, however, if this instability is due to the potentials being applied or the pH of the electrolyte. In order to address how the pH of the electrolyte may be affecting the stability of the species responsible for peak 3, CVs of the nanoplatelet carbon were recorded after soaking the carbon in de-ionized water, 0.5 M Na_2SO_4, or 1 M H_2SO_4 for approximately 65 hours. In order to account for differences in surface area between the carbon samples and more easily compare the peaks in the different CVs, all CVs were normalized to the double-layer current (i.e., the flat region of the CV), as described in subsection "2.3.1 Methods for Normalizing Cyclic Voltammograms". Soaking the nanoplatelets in de-ionized water did not affect peak 3, as it was still present in initial cycles and disappeared as usual with CV cycling (Figure 4-6).

This suggests that the species responsible for peak 3 is not simply a water-soluble contaminant. Soaking the carbon in 0.5 M Na_2SO_4 did not eliminate peak 3 either (Figure 4-6). However, the peak separation (i.e., the separation between the oxidation and reduction peak) is larger than usual after soaking in Na_2SO_4 electrolyte, indicating that the redox reaction has slowed down. Replicates of this Na_2SO_4 soak showed variability in the peak separation, although the peaks were always more separated than the peaks in CVs of as-received Elcora carbon. Soaking the nanoplatelets in 1 M H_2SO_4 entirely eliminated peak 3 (Figure 4-6). This confirms that the species responsible for peak 3 is unstable in the sulfuric acid electrolyte. This information could eventually aid in the identification of the species responsible for peak 3, but would be consistent with either a surface functional group or contaminant that is unstable at acidic pHs.

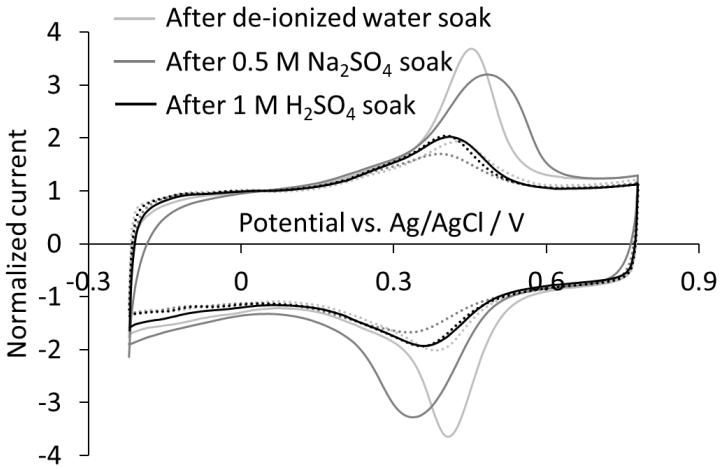

Figure 4-6. Representative CVs at 100 mV/s of nanoplatelet carbon in 1 M H_2SO_4 after soaking in water, neutral electrolyte (0.5 M Na_2SO_4), and acidic electrolyte (1 M H_2SO_4) where the solid line represents cycle 2 and the dotted line represents cycle 1000.

Although this experiment confirms that the sulfuric acid electrolyte does contribute to the instability of peak 3, the potentials applied during the CVs could play a role as well. In order to explore this, CVs of the nanoplatelets were first run either from -0.22 to 0.28 V or 0.28 to 0.78 V, followed by CVs in the full window (Figure 4-7). CVs performed in the lower potential window caused peak 3 to disappear entirely, whereas CVs in the upper potential window resulted in a decrease in peak 3 but did not entirely eliminate it. This suggests that applying lower potentials (below 0.28 V vs Ag/AgCl) accelerates the degradation the species responsible for redox peak 3. Some possibilities for why this may be include a reduction reaction causing the degradation of the species responsible for peak 3, or the more positive potentials resulting in a passivating layer, slowing the species degradation.

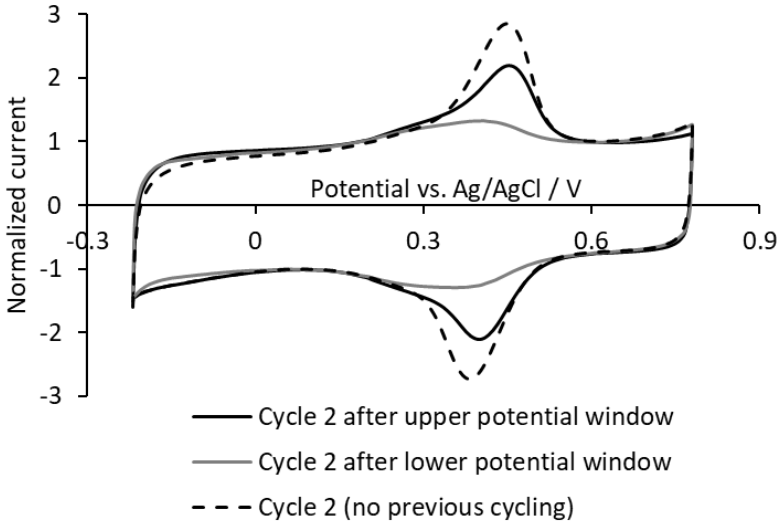

Figure 4-7. CVs of nanoplatelet carbon recorded in 1 M H_2SO_4 after cycling in the upper potential window (-0.22 to 0.28, 100 cycles) and the lower potential window (0.28 to 0.78 V, 100 cycles) with a CV of as-received nanoplatelet carbon for comparison.

From the evidence presented herein, we were able to determine that the species responsible for redox peak 3 in Elcora carbon CVs is unstable at an acidic pH and at applied potentials in the lower half of our CV potential window. Therefore, we were able to eliminate peak 3 from the Elcora carbon CVs by running CVs in acidic electrolyte at the full 1 V potential window, allowing us to better study the behaviour of peaks 1 and 2. Although it has been established that peaks 1 and 2 increase in size during CVs in the full potential window, it has not been established if these peaks may have different behaviour depending on the potential window of the CVs. To explore this, a similar experiment was conducted to the experiment shown in Figure 4-7. However, before running the CVs at either the -0.22 to 0.28 V or 0.28 to 0.78 V window, 50 CVs at the full potential window (-0.22 to 0.78 V) were performed in order to eliminate peak 3 from the data. This way, the CVs recorded after cycling at the upper or lower window can be more easily compared for differences in peaks 1 and 2. Cycling at higher potentials results in larger peaks 1 and 2 compared to cycling at low potentials (Figure 4-8). Therefore, applying potentials above 0.28 V is helpful in accelerating the formation of the redox-active functional groups responsible for peaks 1 and 2. This may be desirable since the pseudocapacitive nature of these species suggests they could improve the energy storage of this material in EC systems.

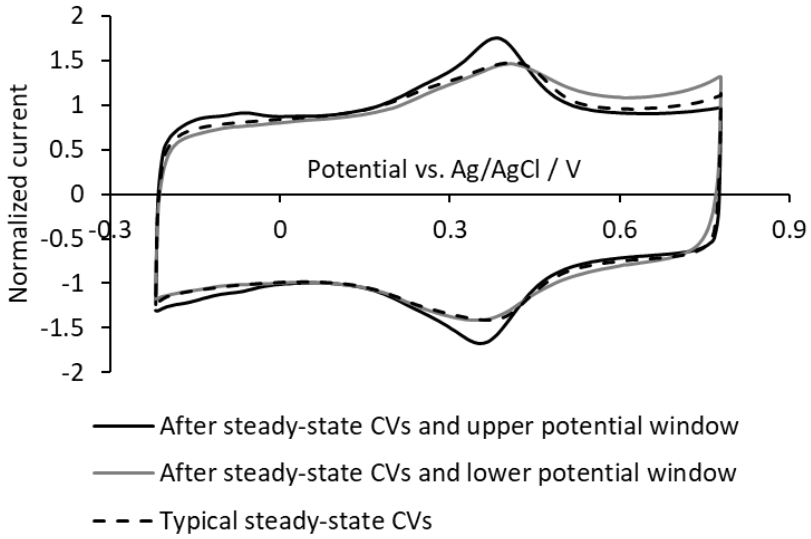

Figure 4-8. CVs of nanoplatelet carbon in 1 M H_2SO_4 after steady-state CVs and cycling in the lower potential window (-0.22 to 0.28 V, 11000 cycles) and upper potential window (0.28 to 0.78 V, 11000 cycles), with a typical steady-state CV (i.e., cycle 50 without prior electrochemical experiments) shown for comparison.

From these experiments, the Elcora carbons seem most promising for energy density due to the large proportion of redox-active functional groups responsible for peaks 1 and 2. However, the unstable species responsible for peak 3 could be problematic for energy storage performance if it is a redox-active contaminant.[66] Identification of this species is addressed in the next subsection.

All of the carbons tested in this section have the ability to develop more redox-active functional groups, if higher potentials are applied (i.e., potentials in the 0.28 to 0.78 V vs Ag/AgCl window). Developing more redox-active groups may be desirable to increase energy density, but we will need to consider how changes in the carbon surface may impact the connection between carbon and pseudocapacitive manganese oxide, as will be studied in Chapter 6.

4.2.2 Unstable Redox Species in Elcora Carbons

The redox peak previously labelled "peak 3" in Elcora carbon CVs is of interest as it could be from a redox-active surface functional group that could contribute to energy storage if stabilized. Alternatively, this peak could be from a contaminant which could potentially be a source of energy loss in the electrode.[66] Therefore, it was of interest to Elcora to further investigate what is responsible for the unstable redox peak 3. The experiments presented in the preceding subsection have determined that the species responsible for peak 3 is unstable at an acidic pH and at lower potentials in our CV potential window. This allowed us to eliminate peak 3 in order to better study other redox peaks present in the Elcora carbon CVs but does not necessarily provide insight into what type of species is responsible for this unstable redox peak.

Note that there were two different batches of both nanoplatelet carbon and graphene carbon provided by Elcora for examination. The only carbon provided by Elcora that did not present "peak 3" in cyclic voltammetry experiments was the second batch of graphene. Importantly, this batch of carbon went through an additional purification process that the other carbons did not undergo. This raises the question of whether peak 3 might be due to a redox active contaminant. One possibility for this is an iron contaminant, which are known to be common in mined graphite (the starting material for these carbons) and could have redox activity around the potential where redox peak 3 appears. Recall, however, that there was no redox-active contaminant found in either EDS or XPS analyses (see sections "4.1.2 Electron Dispersive Spectroscopy" and "4.1.3 X-Ray Photoelectron Spectroscopy"). Therefore, we must also consider the

possibility that the difference in processing for these carbons has resulted in a difference of surface functional groups, and that this may be the source of peak 3. However, when the second batch of graphene (which did not have peak 3) was analyzed by XPS and compared to the other Elcora carbon materials, it did not have majorly different abundances of surface functional groups (see Table 2). Therefore, our physical characterization of these materials has not provided evidence that peak 3 is due to a contaminant or carbon surface functional group. Further electrochemical investigation may provide insight into what could be causing this unstable redox activity.

To evaluate if iron contamination could cause the same kind of electrochemical behaviour as redox peak 3, Vulcan carbon (which does not normally exhibit this peak) was contaminated with iron. Initially, the electrolyte was contaminated with $FeSO_4$ and, although this caused CV redox peaks centred around the same potential as peak 3, the peak separation was large indicating slow kinetics. This deviated from the fast kinetics (and therefore, near-mirror-image redox peaks) seen for peak 3 in CVs of the Elcora carbons (see Figure 4-5b and Figure 4-5c). However, these faster kinetics could be because the iron contaminant was existing within the pores of the carbon, rather than in the bulk electrolyte, making it more readily available at the carbon surface. To explore this, Vulcan carbon was soaked in 1 M H_2SO_4 contaminated with 0.05 M $FeSO_4$. Cyclic voltammograms were then recorded in 1 M H_2SO_4 electrolyte. The resulting cyclic voltammograms (Figure 4-9a) are very similar to typical cyclic voltammograms of the Elcora nanoplatelet carbon (Figure 4-9b). Note that in both cases the redox peaks are centred around a similar potential, fairly close to mirror image (i.e., kinetically fast), and

decrease in a similar manner with progressive cycling. From this, it seems that iron contamination is electrochemically consistent with the behaviour of "redox peak 3" seen in most Elcora carbon cyclic voltammograms.

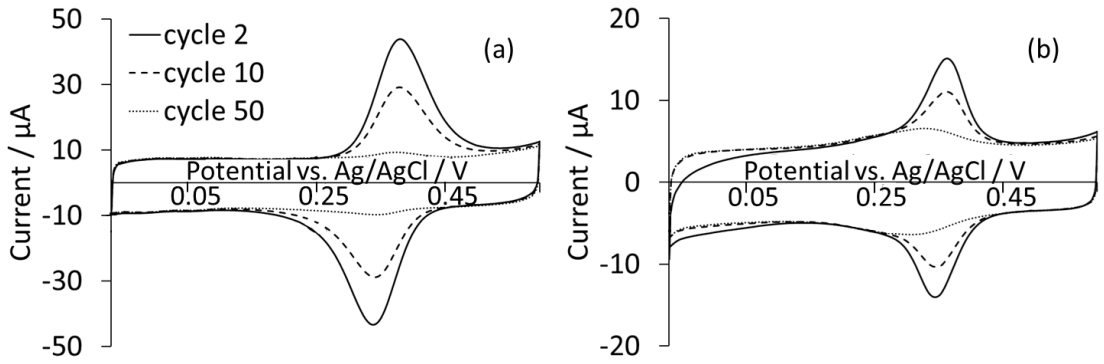

Figure 4-9. Cyclic voltammograms recorded in 1 M H_2SO_4 electrolyte for (a) Vulcan after soaking in a solution containing 0.05 M Fe^{2+} and (b) typical cyclic voltammograms of Elcora Nanoplatelet carbon.

This evidence seems to suggest that the unstable redox peak seen in the Elcora carbon CVs might be from iron contamination, which would also be consistent with the fact that the species responsible for "peak 3" was unstable when soaked in acidic electrolyte. Iron contamination would be undesirable as it is known to cause energy loss (or self-discharge) in carbon materials.[67,68] However, recall that EDS and XPS of the Elcora carbons did not detect iron or any other redox-active contaminants (see sections "4.1.2 Electron Dispersive Spectroscopy" and "4.1.3 X-Ray Photoelectron Spectroscopy"). It is possible, however, that there are contaminants at concentrations below the detection limits of these techniques. The surface sensitivity and small detection area of the XPS and EDS, respectively, may also result in practical limitations in the detection of contaminants. Although our attempts to identify the species responsible for

"redox peak 3" in Elcora carbon CVs were inconclusive, it was ultimately not worth investigating further, especially since our industry partners were able to eliminate the peak by altering their purification process.

4.2.3 Rate Capabilities

Being able to operate at fast rates is critical for carbon materials intended for EC applications, as these devices are typically intended for use at high power. Because carbons store energy mainly through double-layer charge storage at the electrode-electrolyte interface, the rate that charge can be stored and released is limited by how quickly electrolyte ions can move to and from the carbon surface. This can be an issue in carbon materials with small pores, as electrolyte ions experience resistance as they navigate narrow and long spaces, decreasing the rate capabilities in these kinds of carbon materials.

The rate capabilities of different carbons were explored by altering the sweep rate of the CVs and normalizing each CV current by sweep rate, yielding capacitance as described in subsection "2.3.1 Methods for Normalizing Cyclic Voltammograms". Note that before these experiments, CVs were performed until they reached steady-state in order to eliminate redox peak 3 and ensure it is not obscuring the data. All of the carbons exhibited a decrease in their capacitance as the sweep rate increased (Figure 4-10), as electrolyte ions are not able to access deep within the pores of the carbon material effectively (causing a decrease in the double-layer charge storage). Note that at faster rates the CVs become more slanted and approach the response of a pure resistor, which

would form a straight line with a slope inversely proportional to the resistance in a CV. In this experiment, the Vulcan and nanoplatelet carbons showed less capacitance loss at high sweep rates compared to the graphene and reduce graphene oxide (Figure 4-10). This suggests that these carbons will have better rate capabilities (i.e., perform better at high powers). This may be an inherent property of these carbon materials, since we might expect larger particle sizes to result in larger channels between carbon particles, allowing more facile movement of ions through the carbon material (recall that the nanoplatelet carbon showed large spaces between carbon particles in SEM images in Figure 4-1b). It should be noted, however, that the experimental set-up may be influencing these results. Variation between replicates suggests that there is variation in the amount of carbon material that packs into the microcavity electrode. Likely, the more tightly a carbon is packed into the microcavity, the smaller the channels would be between carbon particles. Smaller channels would cause higher electrolyte resistance as it moves through the carbon material, resulting in more capacitance loss at fast sweep rates. It should be noted, therefore, that the way each carbon material is "packed" will be different for other electrode set-ups. At this point, it is unclear how these results will translate to a more typical working electrode set-up. Nevertheless, these results show that Elcora's nanoplatelet carbon's performance at fast rates is similar to Vulcan XC-72, suggesting it is a promising material for EC applications.

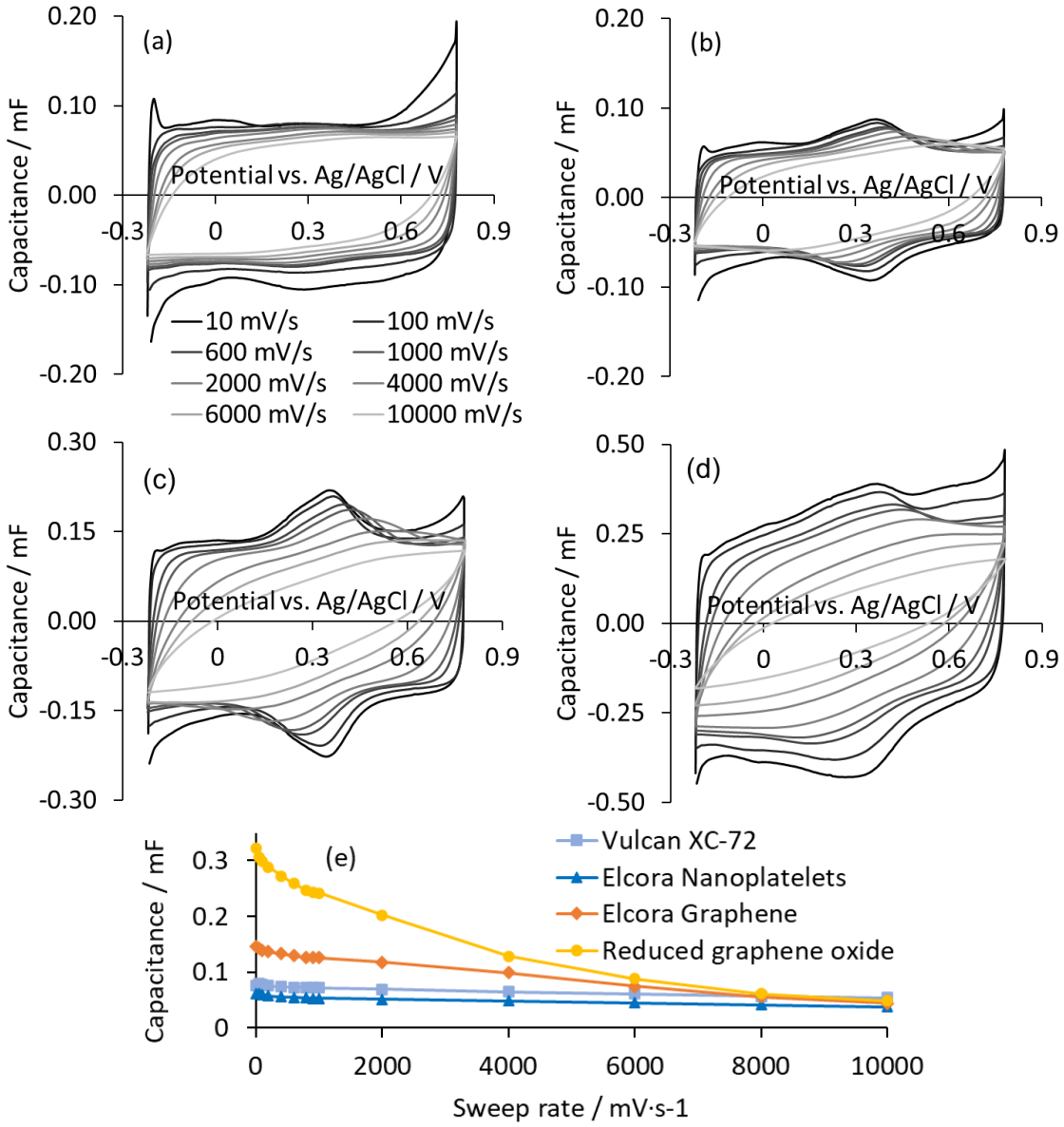

Figure 4-10. Capacitance of (a) Vulcan, (b) Elcora nanoplatelet carbon, (c) Elcora Graphene, and (d) commercial reduced graphene oxide at selected sweep rates from CVs recorded in 1 M H_2SO_4 electrolyte and (e) a comparison of capacitance at 0.15 V vs Ag/AgCl at all sweep rates for these four carbon materials.

4.3 Carbon Electrochemistry in Neutral-pH Electrolyte

When carbon is used in conjunction with manganese oxide in an electrode, it will need to be in neutral (or near-neutral) pH electrolyte (to avoid dissolution of the

manganese oxide). Therefore, it is necessary to establish if the redox-active groups (as seen in CVs in acidic electrolyte) can also contribute to energy storage in neutral pH electrolytes. Additionally, although the functional groups of carbon have been shown to change during electrochemical experiments in acidic electrolyte, it has not yet been established if a similar phenomenon occurs during electrochemistry at a more neutral pH. Again, this is an important consideration since if the carbon material is changing during electrochemical experiments, it could impact the carbon's connection with manganese oxide (potentially impacting the rate performance and cycle life of the system). Because initial evaluations of the rate capabilities of the four carbons studied in this thesis suggest that Vulcan and Elcora nanoplatelets have superior rate performance (and therefore higher promise as carbons for EC applications), they will be the focus in the following subsection.

4.3.1 Redox-Active Surface Functional Groups

We have previously established that cyclic voltammetry of Vulcan in 1 M H_2SO_4 electrolyte causes the development of peaks associated with redox-active functional groups, as seen by the broad peak centered around 0.3 V in Figure 4-5a. However, CVs of Vulcan in 0.5 M Na_2SO_4 show no evidence of such peaks, even after up to 92 hours of cycling (Figure 4-11a). It is possible that redox-active functional groups are simply not developing in the near-neutral pH electrolyte. However, it is also possible that redox-active groups have developed, but the peaks associated with these groups are simply not observable in the Na_2SO_4 due to the low concentration of H^+ which is required for the

Faradaic reaction of some functional groups (such as quinones).[65] In order to assess if redox-active groups had developed on the carbon surface during the CVs in Na_2SO_4, the electrode used in Figure 4-11a was transferred to a separate cell containing 1 M H_2SO_4 electrolyte after cycling in Na_2SO_4 electrolyte. The abundance of H^+ in the H_2SO_4 electrolyte may aid in the detection of redox-active groups whose reactions involve H^+. The CVs of this material in acidic electrolyte exhibit peaks around 0.3 V vs Ag/AgCl (Figure 4-11b), revealing that redox-active groups have developed on the carbon during CVs in Na_2SO_4, even though these groups were not detectable in the Na_2SO_4 electrolyte itself.

The CVs in acidic electrolyte also show very small peaks at a more positive potential of around 0.4 V vs Ag/AgCl (Figure 4-11b) during early cycles, but this peak diminishes quickly after exposure to acidic electrolyte. This suggests that the CVs in Na_2SO_4 electrolyte have developed functional groups that are unstable in acid and that do not normally develop during electrochemistry in acidic electrolyte. When we eventually study carbon in conjunction with manganese oxide (in Chapter 6) we will need to remember that the carbon's surface chemistry may be changing during electrochemical experiments, but that this change is not exactly the same as what tends to happen in acidic electrolytes.

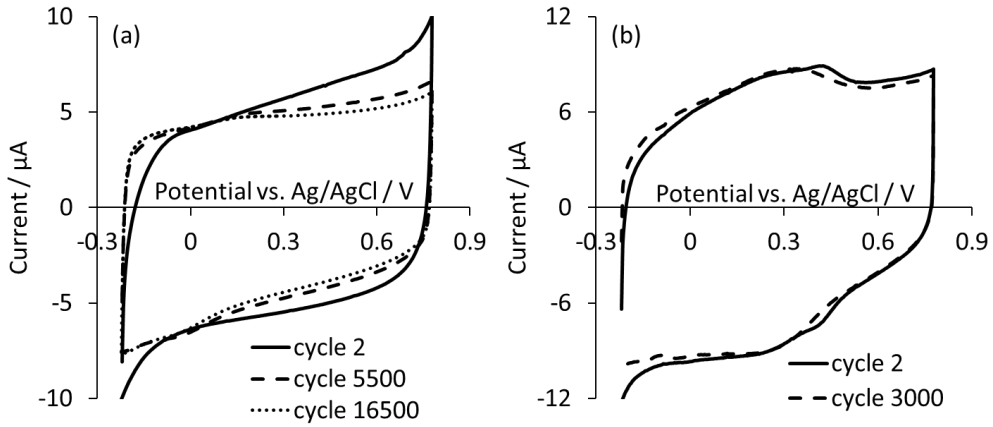

Figure 4-11. CVs at 100 mV/s of the same Vulcan electrode (a) in Na_2SO_4 electrolyte up to 16500 cycles (92 hours) and (b) in H_2SO_4 electrolyte after the CVs in Na_2SO_4.

As described above, relatively small redox peaks develop after electrochemistry in neutral electrolytes. In order to establish if more abundant surface functional groups would be observable in Na_2SO_4 electrolyte, redox-active groups were first developed on Vulcan by CVs in 1 M H_2SO_4 (Figure 4-12a). Then, this electrode was transferred to another cell with 0.5 M Na_2SO_4 electrolyte, and CVs in this cell show no evidence of peaks (Figure 4-12b). When the electrode was later returned to the acidic electrolyte cell (Figure 4-12a, "cycle 10 (after CVs in (b))"), the redox peaks were still visible. This confirms that these redox-active surface functional groups were definitely present when the CV was recorded in the 0.5 M Na_2SO_4 electrolyte. This demonstrates that even if Vulcan has an abundance of redox-active functional groups, the associated peaks will not be observable in neutral-pH electrolyte CVs. This suggests that changes in the redox-active functional groups present in this carbon will simply not be trackable during electrochemical experiments in Na_2SO_4 electrolyte. In order to gain insight into how these functional groups are changing, electrodes would need to be evaluated a cell with acidic electrolyte.

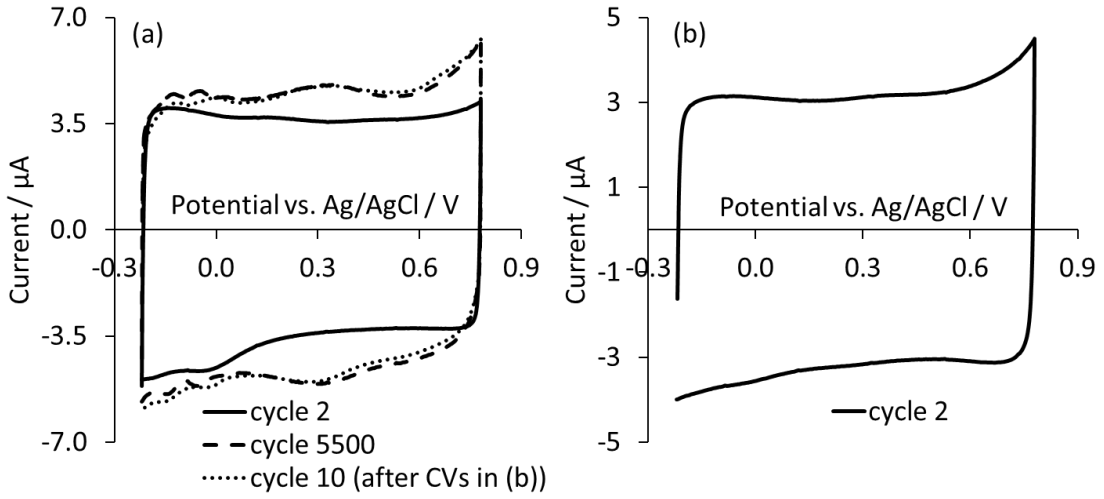

Figure 4-12. CVs of the same Vulcan electrode (a) in H_2SO_4 electrolyte up to 5500 cycles (30.5 hours) and after the CVs shown in b and (b) in Na_2SO_4 electrolyte after the 5500 cycles in H_2SO_4.

Although redox peaks cannot be seen in Na_2SO_4 electrolyte for Vulcan, it is unclear if the same would be true for carbon materials with an even higher abundance of redox-active functional groups. In order to explore this, CVs of Elcora's nanoplatelet carbon were performed in 0.5 M Na_2SO_4 (Figure 4-13a). By the end of the 5500 cycles, some peaks are visible below 0.2 V, however these peaks are not visible during initial CVs. It is not clear whether these peaks are due to the same functional groups normally observed in CVs in acidic electrolyte or not. The same electrode was then transferred to a cell with acidic electrolyte, which reveals that the CVs in neutral-pH electrolyte did not affect peak 3 (Figure 4-13b). Recall that peak 3 readily diminishes during cyclic voltammetry in H_2SO_4 electrolyte, especially when potentials below 0.5 V are applied. Therefore, the degradation of the species responsible for peak 3 is not accelerated at low potentials when there is not a surplus of H^+ in the electrolyte.

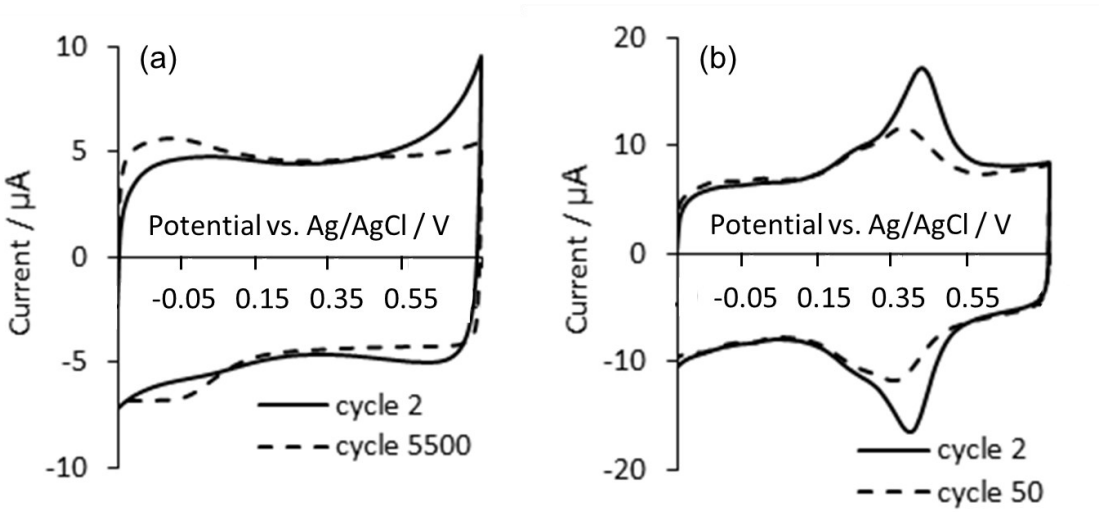

Figure 4-13. CVs of the same nanoplatelet carbon electrode (a) in Na_2SO_4 electrolyte up to 5500 cycles (30.5 hours) and (b) in H_2SO_4 electrolyte after the 5500 cycles in Na_2SO_4.

In order to evaluate how the CVs in neutral-pH electrolyte affected peaks 1 and 2, cycle 50 in acidic electrolyte (from Figure 4-13b) is compared to cycle 50 for an electrode that did not undergo prior cycling in neutral-pH electrolyte. Here, cycle 50 is being compared to avoid obstruction from "peak 3" (recall from section "4.2.1 Redox-Active Surface Functional Groups" that peak 3 is unstable and thought to potentially be a contaminant). Note that the only difference between these two electrodes is that one previously underwent 30.5 hours of cycling in 0.5 M Na_2SO_4 electrolyte whereas the other did not. This shows that cycling in 0.5 M Na_2SO_4 increased the size of peaks 1 and 2 (Figure 4-14), confirming that more redox-active functional groups form on the nanoplatelet carbon during electrochemistry in neutral-pH electrolyte, as was also the case for the Vulcan. Therefore, it is important to remember that this change in carbon surface chemistry during electrochemical experiments in 0.5 M Na_2SO_4 is not a phenomenon exclusive to Vulcan.

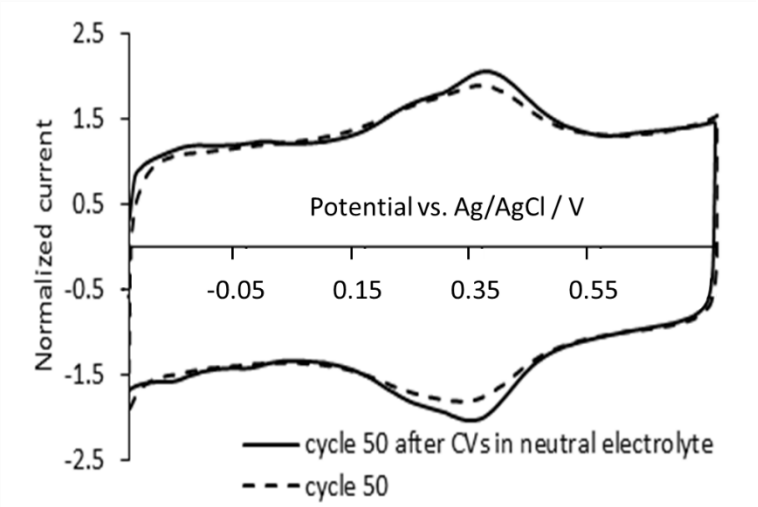

Figure 4-14. CVs of nanoplatelet carbon in H_2SO_4 after 5500 cycles in Na_2SO_4 electrolyte (solid line) and without other electrochemical experiments (dashed line).

4.4 Full-Cell Electrochemical Capacitor Devices

The half-cell electrochemical testing presented thus far in this chapter allowed us to study our carbon materials as-received in a microcavity working electrode. Additionally, the use of a reference electrode in this half-cell set-up gives us control over the electrode's potential, providing insight into each carbon's electrochemical behaviour. However, in order to understand how these carbon materials might perform in real-world devices, full-cell EC coin cells were made using the carbon materials explored in this chapter, under the supervision of Elcora Advanced Materials. Details on how full-cell carbon electrodes and coin cells were made can be found in sections "3.2.2 Full-Cell Electrochemical Capacitor Carbon Electrodes" and "3.3.2 Full-Cell Electrochemical Capacitor Coin Cells". Note that the voltage window used for CV testing of full cells in this section is 1 V. Because there is no reference electrode in these full-cell systems, we do not know the exact potentials of the two carbon electrodes. However, because these

are symmetric cells, we can estimate that the electrode potential will increase ~0.5 V for one electrode and decrease ~0.5 V for the other. Given that the open-circuit potential (i.e., resting potential) for the electrode materials used in this section typically range between 0.5 to 0.6 V vs Ag/AgCl, we can expect the potentials of the carbon electrodes to range anywhere from approximately 0 to 1.1 V vs Ag/AgCl during this testing, with some variation. This potential range is a bit higher than that used in the half-cell testing in previous sections, causing these cells to be at higher risk of oxygen evolution in neutral pH electrolytes.

Initial prototypes of these coin cells presented high resistance, which is a particularly problematic issue for EC devices as it negatively impacts rate capabilities. This spurred further investigation into the optimization of resistance in these cells. Cells were made that had no carbon (to evaluate if contact resistance between the carbon and substrate was an issue) but were still resistive in a cyclic voltammetry experiment. Cells were then made that had different volumes of electrolyte (50 µL and 150 µL) and different concentrations of electrolyte (0.5 M vs 1 M Na_2SO4_4). While increasing the volume of electrolyte marginally improved the resistance, it was suspected that the real root of the problem was the non-wettability of the polyolefin separator being used at the time (as this separator is often used in non-aqueous systems). Therefore, some different separators were investigated including: glass microfiber, cellulose, gas line filter (unknown material), and coffee filter paper. Both the glass microfiber and gas line filters provided dramatically improved resistance. Because the gas line filter was an unknown

material, the glass microfiber filter was selected as the separator of choice for the cells discussed in this section.

To further attempt to reduce resistance in these full-cell EC devices, a couple of modifications to the carbon electrodes were made and tested by CV. One possible source of resistance in these cells could come from a poor connection between the carbon and its copper-foil substrate. Therefore, we tested if compressing the carbon electrodes could improve resistance in our full-cell devices by pressing the electrodes through rollers that apply pressure and heat (50 °C). CV comparisons of cells made with these electrodes versus non-compressed electrodes is shown in Figure 4-15. Note that the compressed coating (Figure 4-15, "Compressed") actually results in a cell that is more resistive than the non-compressed coating (Figure 4-15, "Non-compressed"). This is thought to perhaps be due to a decrease in porosity introducing higher resistance to electrolyte movement through pores in the compressed coating. Therefore, making electrochemical capacitors without compressing the carbon coatings will be important for high-rate performance. A third type of carbon electrode was made by removing the carbon coatings from their copper foil backings by immersing them in formic acid. Note that this type of carbon electrode was non-pressed. This electrode type results in a smaller but more rectangular-shaped CV (Figure 4-15, "No copper foil") compared to the non-compressed electrodes with copper foil backings (Figure 4-15, "Non-compressed"), indicating that performance of these electrodes is closer to that of an ideal capacitor. Eliminating the copper foil is therefore important for improving the capacitor-like behaviour of these cells, eliminating a non-reversible electrochemical processes, as is seen in the oxidation wave (i.e., increase

in positive current) for the “non-compressed” coatings in Figure 4-15. This non-reversible process would lead to energy loss between device charges and discharges, hindering the energy efficiency of the device.

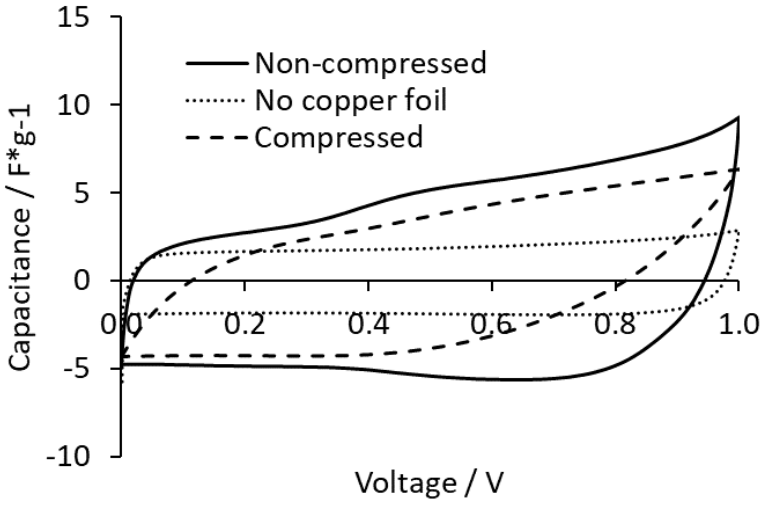

Figure 4-15. Representative cyclic voltammograms at 100 mV/s for full-cell EC devices made with compressed, non-compressed and no-backing (“no copper foil”) Elcora nanoplatelet carbon electrodes (cell electrolyte is 0.5 M Na_2SO_4).

Further exploration of the rate performance of these different coating types was done by altering the sweep rate of the cyclic voltammograms. Note that the compressed films (Figure 4-16b) undergo a greater capacitance loss at fast rates compared to the non-compressed films (Figure 4-16a), suggesting the compression of the film may have decreased the porosity of the electrode, hindering fast movement of electrolyte ions through the carbon coating. Note that the cell with no copper foil backings actually undergoes the least amount of capacitance loss at fast rates (Figure 4-16c). This suggests that the resistance of this type of cell is lower than the non-compressed cell with the copper foil (Figure 4-16a). Therefore, it is likely that the connection between the carbon

and copper foil contributes some resistance to the system. Additionally, note that all these cells present an oxidation wave (i.e., increase in positive current at higher voltages) in their CVs (see Figure 4-16). As mentioned earlier in this chapter, the voltage used in these experiments paired with the natural resting potentials of the carbon materials used in the electrodes puts these cells at risk for oxygen evolution. It is therefore likely that the oxidation wave seen in these CVs corresponds to the oxidation of water into oxygen gas. Note, however, that the cells that contain copper (Figure 4-16a and Figure 4-16b) have peaks in their positive current that do not appear in the CVs for the cell without copper. This indicates that there is an additional non-reversible process related to the presence of the copper, possibly the oxidation of the copper metal. The cells made without the copper are therefore superior as they benefit from lower resistance overall and will likely be more consistent with long term use due to the absence of the non-reversible reaction seen in the other cells. Cells made without the copper foil backings have been tested immediately after fabrication as well as three weeks later, with no loss in the capacitance, suggesting that they have good short-term stability in storage.

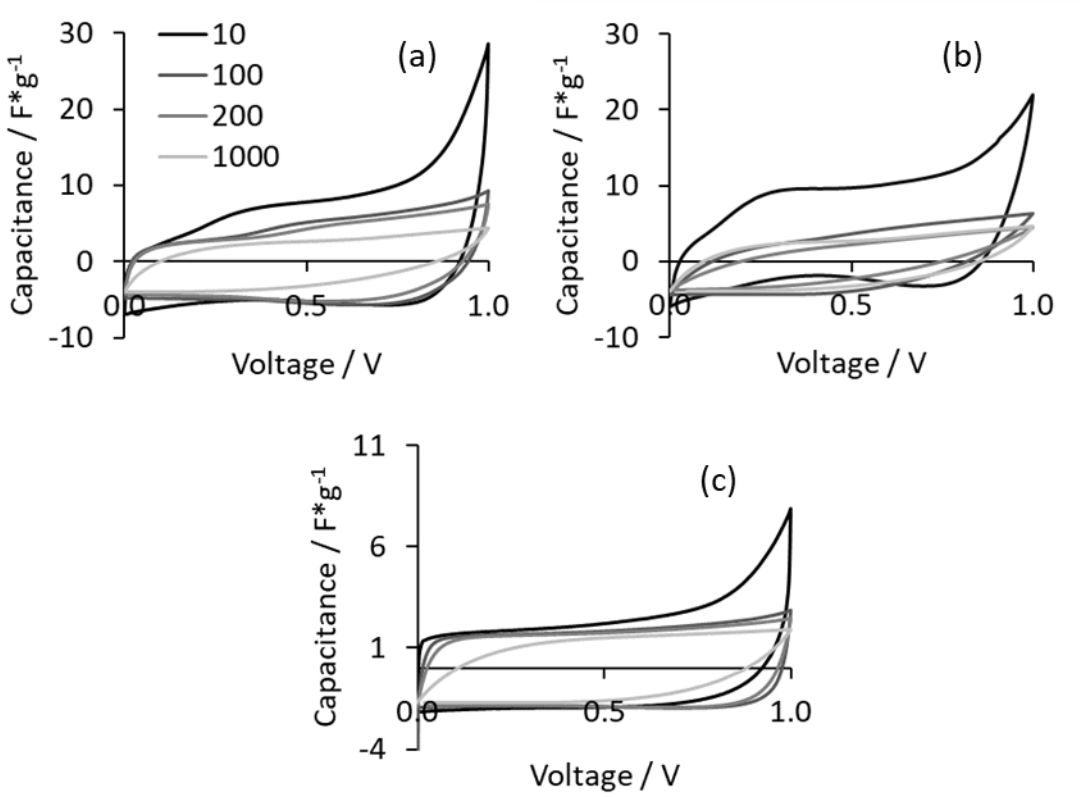

Figure 4-16. Representative cyclic voltammograms of full-cell EC devices made with (a) the non-compressed coatings, (b) the compressed coatings and (c) the coating with no copper foil backing with sweep rates in mV/s indicated in the legend (electrodes are Elcora-nanoplatelet-carbon based and electrolyte is 0.5 M Na_2SO_4).

Next, we wanted to compare how different Elcora carbon materials might perform in full-cell EC devices, both before and after cell usage. In order to simulate cell usage, the cells were charged and discharged in the 0 to 1 V voltage window at constant currents. In Figure 4-17, CVs from immediately before and after this cell usage are compared for different type of electrodes. Because the Elcora graphene material did not perform well in CV sweep rate tests shown earlier in this chapter (see Figure 4-10c), it was determined that its rate capabilities were not sufficient to make it a promising material for EC devices. Elcora's nanoplatelet carbon was instead the material of interest,

and CVs of a full-cell EC device made using this carbon exhibit a reasonably rectangular shape and change minimally after cell usage (see Figure 4-17, “Elcora Nanoplatelet”). This suggests that this device is operating in a capacitor-like manner and maintains its performance after cell usage.

Although the Elcora graphene material was not used on its own in these cells, electrodes were made with a 50:50 mixture of the Elcora graphene and nanoplatelet carbons. This was done in an attempt to increase the energy storage ability for these electrodes while hopefully maintaining the nanoplatelet’s good rate capabilities, as the graphene as a higher surface area and can therefore store more energy via electrochemical double-layer charging and discharging. Interestingly, the specific current for the cell made with a mixture of nanoplatelet and graphene carbons (see Figure 4-17, “Elcora Nanoplatelet + Elcora Graphene”) is lower than the cell with only nanoplatelet carbon in its electrodes, indicating it actually stores less energy by mass. Ultimately, it is unclear if this is difference is statistically significant, as these protype cells were made and tested at the end of our industry partnership grant and replicates were therefore not tested. By comparison, a cell made with electrodes combining Vulcan with Elcora’s graphene (see Figure 4-17, “Vulcan + Elcora Graphene”) has a specific current in between the two previous cell types. This suggests that the Vulcan (which is a carbon black material typical of EC applications) performs better than the nanoplatelet carbon in combination with graphene, but not as well as the nanoplatelet carbon by itself in terms of energy storage. Again, we are unable to determine from the data available if this trend would hold if a full set of replicates were analyzed. One other noticeable difference in

these CVs is that the graphene-containing cells have more vertical changes in current at 0 V and 1 V (Figure 4-17) compared to the cell made with nanoplatelet-only electrodes. This suggests that the cell with only nanoplatelet carbon has more resistance and is therefore slower to react to changes in potential.

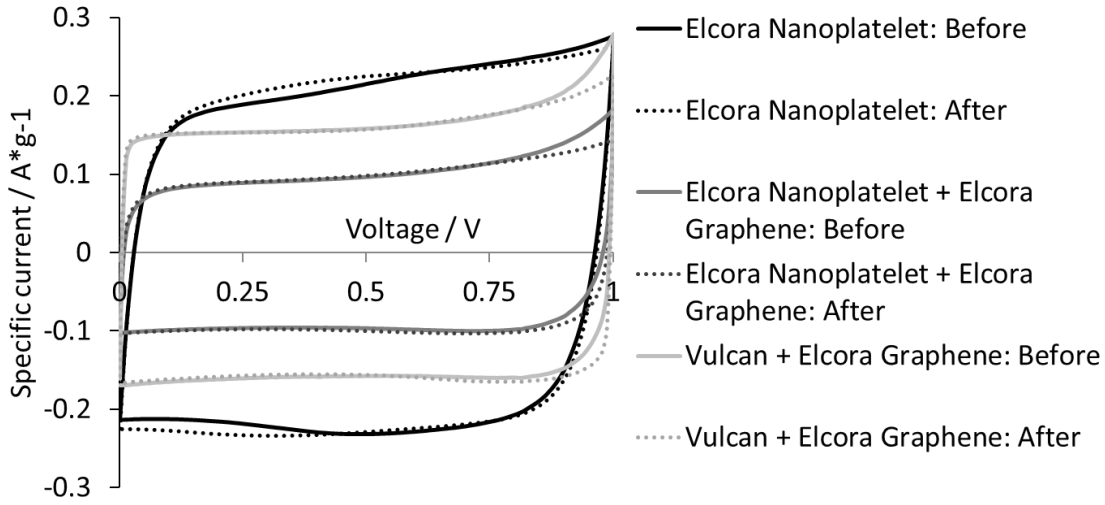

Figure 4-17. CVs at 100 mV/s of Elcora full-cell electrochemical capacitors before and after charge/discharge testing, with the carbon composition of the electrodes listed in the legend and 0.5 M Na_2SO_4 electrolyte (note: multiple electrode materials indicated by "+" are mixed 50:50 in both of the cell's electrodes)

EIS is an electrochemical technique that can be used to evaluate why the CV testing seems to be showing higher resistance for the cell made with only nanoplatelet carbon. Recall from section "2.4.2 Nyquist Plots" that we expect capacitive materials, like those used in EC applications, to present an upright tail in EIS Nyquist plots. Nyquist plots of the full-cell EC devices with different electrode compisitions are shown in Figure 4-18 and generally show this upright tail shape, as we would expect for EC devices. However, the Nyquist plot for the full-cell device made with only nanoplatelet carbon in

its electrodes does have a small semi-circle before its upright tail (Figure 4-18, “Elcora Nanoplatelet”). As discussed in section “2.4.2 Nyquist Plots”, this indicates that this cell has significant resistance across an interface, which is usually from a Faradaic reaction or contact resistance between different materials. We do not expect a Faradaic reaction to be occurring in these cells since carbon stores energy via the electrochemical double layer and the redox-active species present on these carbons were shown not to be active in 0.5 M Na_2SO_4 electrolyte. This makes a contact resistance between materials the likeliest source for this resistance. Given the layers of different materials in these coin cells (see Figure 3-3), it is hard to say where exactly this resistance might be from. Additionally, with the limitations in number of cells tested for this part of the project, we cannot be sure if the semi-circle in the nanoplatelet cell’s Nyquist plots is specific to this replicate or something that occurs more generally with this electrode type. Nevertheless, EIS has helped us identify the issue with this particular cell, which is a helpful first step in further improving the performance of these devices.

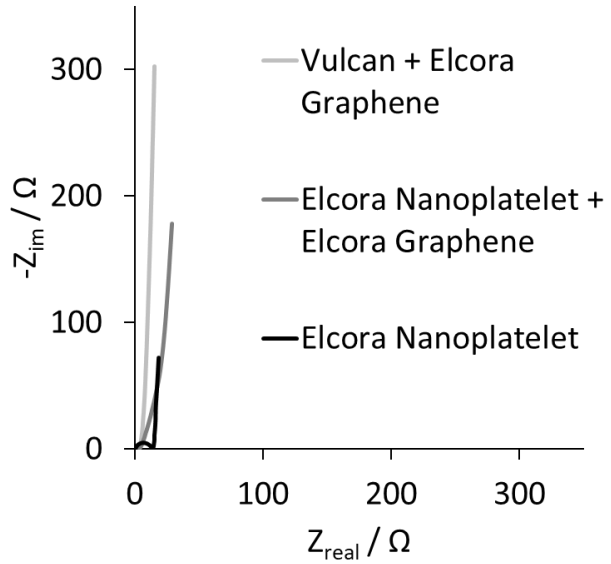

Figure 4-18. EIS Nyquist plots of Elcora full-cell electrochemical capacitors with 0.5 M Na_2SO_4 electrolyte, where the carbon composition of the electrodes listed in the legend (note: multiple electrode materials indicated by "+" are mixed 50:50 in both of the cell's electrodes)

4.5 Conclusions

All the carbon materials studied in this chapter tend to show two redox peaks that may increase slightly during electrochemical experiments (referred to as peaks 1 and 2). The presence of two distinct peaks could mean that there are two different redox-active functional groups, or it could mean that the same type of functional group exists in two different chemical environments (e.g., para- and ortho-quinones). Cyclic voltammetry in acidic electrolyte reveals that electrochemistry increases the level of redox-active functional groups on the surface of the carbon, particularly if cycling above potential of 0.28 V vs Ag/AgCl. Cycling in neutral-pH electrolyte also causes an increase in redox-active functional groups, although the peaks associated with those groups may not be

visible in CVs in the neutral electrolyte (for Vulcan) or at least not visible during early cycles (for the nanoplatelet carbon).

The carbons that were received from Elcora (nanoplatelet and graphene) exhibit a third redox peak that is apparent in CVs in 1 M H_2SO_4 electrolyte. The species responsible for this peak is unstable and can be eliminated by soaking the carbon in 1 M H_2SO_4. The degradation of this peak can be accelerated by applying potentials below 0.5 V in acidic electrolyte, although this does not have the same effect in neutral-pH electrolyte. It is possible that this redox peak is due to a functional group that is not stable at acidic pHs, however mined graphite (the source material for the Elcora carbons) is known to sometimes have iron-containing contaminants, which may be another possible source for peak 3. Electrochemistry of Vulcan carbon soaked in a 0.05 M $FeSO_4$ solution was consistent with that of the Elcora carbons that showed "peak 3" in CVs, supporting this hypothesis. However, EDS and XPS characterization of these materials found neither a redox-active contaminant nor a difference in surface functional groups for carbons that exhibited "peak 3" in cyclic voltammetry experiments. While we were unable to conclusively determine what species was responsible for this unstable redox peak, Elcora Advanced Materials ultimately eliminated this from their carbon materials by implementing a new purification procedure.

An important figure of merit for carbon materials aimed at EC applications is their power capabilities. Nanoplatelet carbon from Elcora showed a similar level of capacitance loss at high CV sweep rates compared to Vulcan (a commercially-available carbon black that is typical of carbons used in EC applications). The Elcora graphene and

the reduced graphene oxide show much larger capacitance loss at fast sweep rates. This suggests that the nanoplatelet and Vulcan carbons would be better-suited to EC applications. However, it has not been established if these microcavity electrode results are translatable to other electrode systems, as how the carbon powders pack into the microcavities could influence these results.

Prototypes of full-cell EC devices made using Elcora carbon electrode materials were studied in order to get an idea of how these carbons behave in a system more comparable to real-life applications. A number of trouble-shooting variations of these cells were made in order to create full cells with decent electrochemical performance. Thoughtful selection of a separator material and fabrication methods for the electrodes was important. Full-cell EC devices studied for this project with Elcora were made using 0.5 M Na_2SO_4 electrolyte, which allowed us to use readily-available stainless steel hardware for the cells. This neutral-pH electrolyte would also be appropriate for use in applications that combine carbon with pseudocapacitive manganese oxide, as will be discussed later in this thesis. Better performance at fast rates could be achieved by using 1 M H_2SO_4 electrolyte (which has superior conductivity), but this would require an alteration in cell design to be compatible with the electrolyte. Ultimately, though, we were able to create fairly well-performing full cell EC device prototypes, showing that Elcora's nanoplatelet carbon may be suitable for this application.

Chapter 5: Manganese Oxide

Manganese oxide is a promising pseudocapacitive material for EC applications due to its elemental abundance, environmental friendliness, and cost-effectiveness.[16] Therefore, this is the pseudocapacitive material chosen in this thesis to study in conjunction with carbon materials in Chapter 6. Having a good understanding of the properties and electrochemical behaviour will be important before we further complicate our system by adding carbon materials.

One aspect of manganese oxide's electrochemical behaviour that merits further investigation is the origin of semi-circle shapes in its EIS Nyquist plot. Nyquist plot semi-circles arise when there is significant resistance across an interface (recall Section "2.4.2 Nyquist Plots"). In the literature, some researchers show significant semi-circles in manganese oxide Nyquist plots,[13,35–41] although the semi-circle is absent in other results.[42] Therefore, it will be important to understand whether this Nyquist plots feature is intrinsic to manganese oxide (e.g., from its pseudocapacitive Faradaic reaction), or something that arises from poor contact between the manganese oxide and other materials.

This chapter will examine electrodes whose active material is manganese oxides, in the absence of carbon. Here, manganese oxide films are grown on metal foils and a portion of the film may undergo heat treatment. A further description of these electrodes was previously provided in Section "3.2.3 Manganese Oxide Electrodeposition". Note that the abbreviations used to distinguish these different films describe the percentage of film that is heat-treated versus not heat-treated. For example, in a 10dry:90wet

manganese oxide film, the first 10% of the film is heat treated while the remaining 90% is not heat-treated.

Section 5.2 is adapted from a paper published in the Journal of Power Sources,[69] with the exception of the information outlined in subsections 5.2.1 and 5.2.2.

Subsection 5.2.2 is adapted from another existing publication.[70] Note that approximately half of the electrode replicates shown in this subsection were made and tested with the help of Andreas lab colleague Josiah Pratt. All other data collection and all of the analysis were completed by myself.

5.1 Physical Characterization

5.1.1 Scanning Electron Microscopy

SEM images of the wet manganese oxide films on stainless steel and platinum as well at the dry films and all ratios of hybrid dry:wet films are shown in Figure 5-1. All of these films exhibit the same fine platelet texture. Despite the different drying, storage, and substrate conditions, the highly porous structure of the manganese oxide is not noticeably impacted. Neither drying the manganese oxide nor growing it on stainless steel, platinum, or dried manganese oxide has altered the structure. Therefore, differences in electrochemical performance between these different film types cannot be attributed to differences in the manganese oxide morphology.

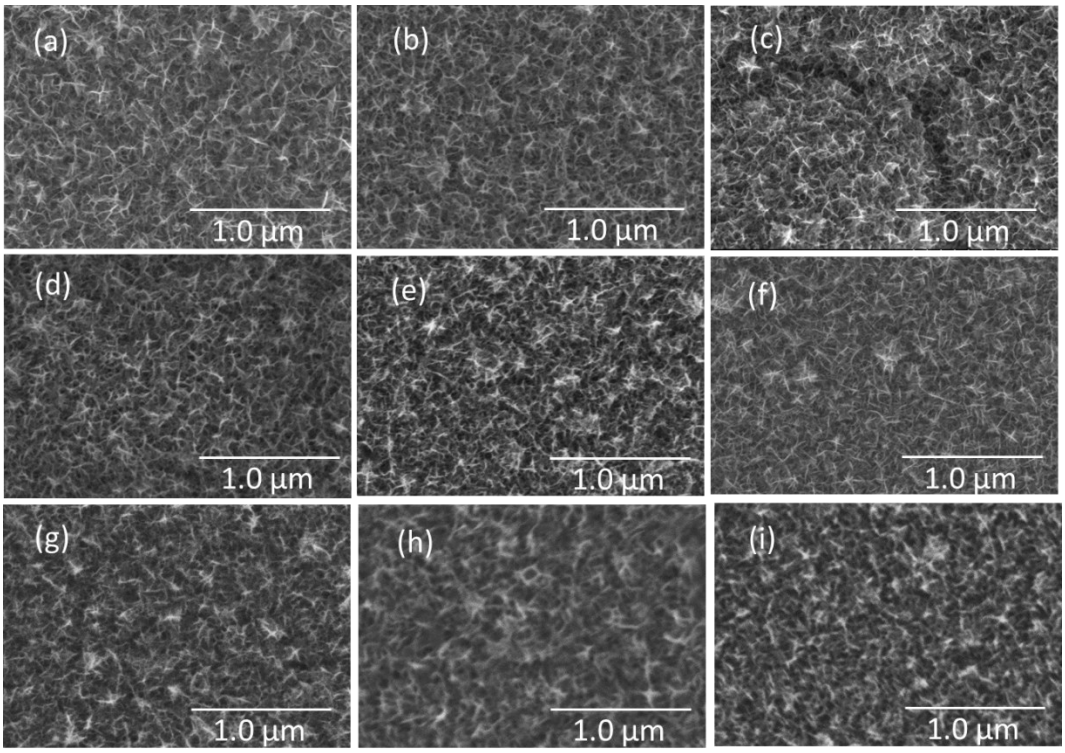

Figure 5-1. SEM of (a) wet film, (b) wet film on platinum, (c) dry film (d) 1dry:99wet, (e) 5dry:95wet, (f) 10dry:90wet, (g) 25dry:75wet, (h) 50dry:50wet, and (i) 75dry:25wet at 50 000 times magnification (films are on stainless steel unless otherwise indicated).

5.1.2 Film Thickness

Film thickness is an important variable for rate capabilities; thinner films lend themselves to higher power. In commercially-made electrodes, film thickness is often manipulated by controlling the mass loading of the electrode's active material. Our manganese oxide films are instead made by electrodeposition, and it has not been established in the literature how the thickness of these films compare to other methods. Therefore, an evaluation of the mass loading or thickness of manganese oxide on our electrodes would help provide context for our electrodes' rate capabilities.

Previous attempts to establish a mass loading of our electrodes have not been successful; the mass of the manganese oxide film is too low to measure on the much heavier stainless-steel substrate and water content in the film cannot be differentiated from manganese oxide material. Therefore, we attempted to measure the thickness of our manganese oxide films. It is important to note, however, that we do not expect the electrodeposition method to result in a uniform film thickness across the entire electrode (a thicker film is expected to form at edges and corners). Additionally, we do not necessarily expect the film thickness of the manganese oxide formed on metal foils to be representative of manganese oxide films formed on carbon materials (presented in Chapter 6), as the nature of the substrate (material, porosity, etc.) is different. Nevertheless, getting an idea of the thickness of our active material will support our understanding of these electrodes.

In order to measure the thickness of our manganese oxide films, a number of methods were used to try to obtain a cross-section of the electrode. Mechanical cutting with scissors and cross-sectioning with a focused ion beam both resulted in too much damage get any meaningful measurements. Subsequently, an ion mill was used to attempt cross sections on two of our electrodes. One of the electrodes was excessively damaged by the technique (Figure 5-2a). However, we were able to use SEM to see a cross section of the other electrode, showing our stainless steel substrate and a manganese oxide film of about 1.2 μm (Figure 5-2b). This may be only a snapshot of one area on one electrode, but it gives us a ballpark for the thickness of our manganese oxide films. Using ion-milling to get a cross section of our electrode was helpful, but the technique's expense

and propensity to excessively damage the electrode limits its utility, especially with respect to collecting multiple thickness measurements on replicates.

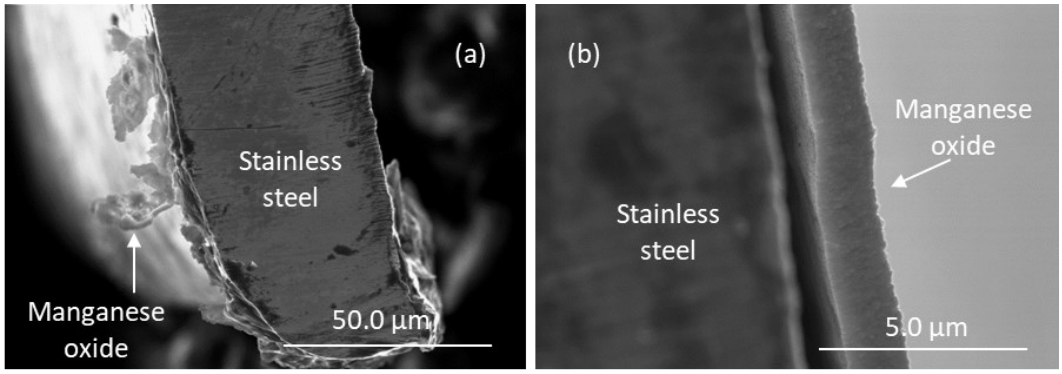

Figure 5-2. Ion-milled cross sections of (a) a dry manganese oxide film (1000 times magnification) and (b) a 10:90 film (10 000 times magnification).

Because we wanted to evaluate the thickness of all the different types of manganese oxide films we have made, we sought another thickness measuring method that would allow us to evaluate a higher number of films. In this thesis, we have analyzed electrodes that have undergone drying procedures (e.g., "dry" vs "wet" films) as well as electrodes that have undergone multiple electrodepositions (e.g., "10dry:90wet" films). Therefore, it is important to establish if either the drying of the films or having multiple electrodepositions is dramatically impacting the manganese oxide thickness, which could in turn impact the electrode's rate capabilities. In order to test this, we lifted the manganese oxide films off of their stainless-steel substrates using a metal wedge. SEM images of resulting flakes were evaluated to get measurements for thickness for all of the types of manganese oxide films (Figure 5-3). This technique has numerous potential sources of error. We cannot be certain that each of imaged flakes represent the full

thickness of the film, as the film may have fractured into layers during sample preparation. Additionally, the angle of the flakes in the SEM images will add some level of inaccuracy to the thickness measurements, as not all flakes are positioned perfectly on their sides. In order to mitigate these potential issues, as many flakes as possible were assessed for each sample and only flakes that were relatively vertical (i.e., positioned on their sides) were measured. Although this technique has its disadvantages, it does allow us to evaluate a larger sample size of thickness measurements for all of the manganese oxide film types.

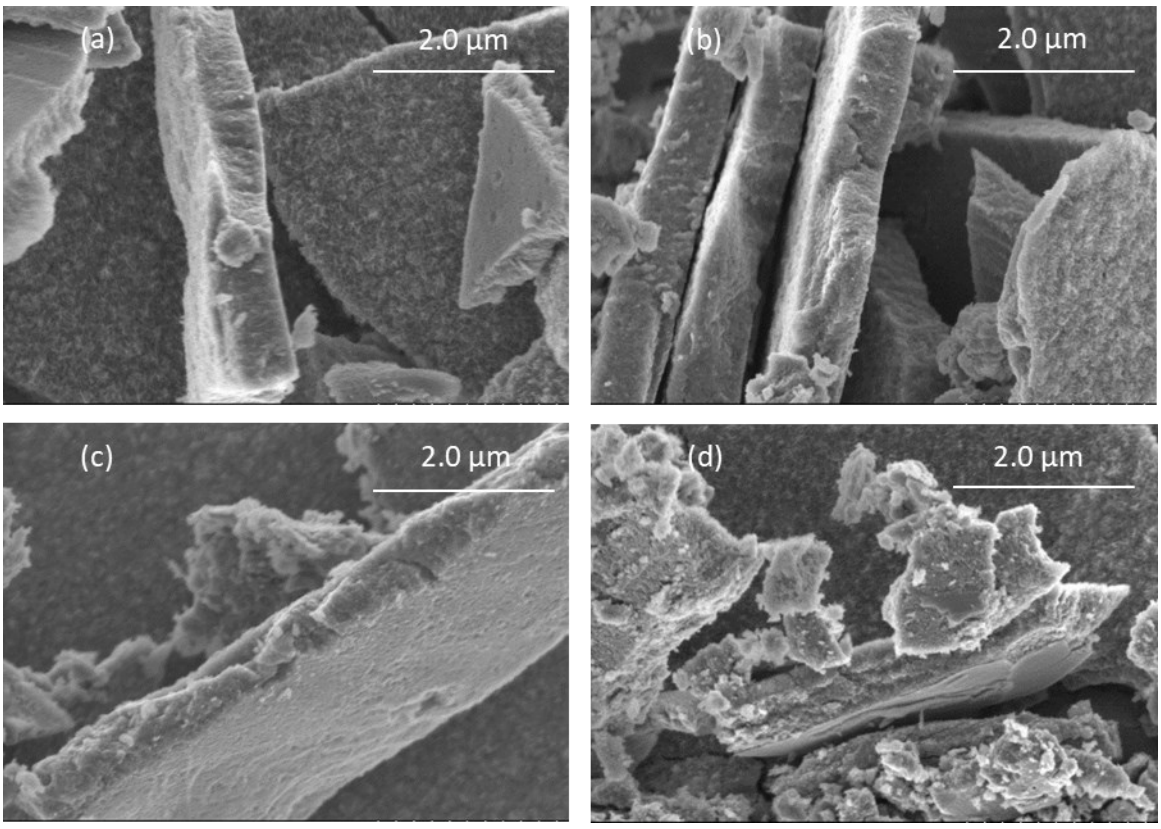

Figure 5-3. Examples of SEM images used to evaluate film thickness, with flakes from (a) wet, (b) 5:95, (c) 10:90, and (d) 50:50 films scraped off stainless steel (at 20 000 times magnification).

The average measured thicknesses of different manganese oxide film types are shown in Figure 5-4. Because we expect each manganese oxide film to have a range of thicknesses and because of the sample preparation method, we anticipated that there may be a considerable amount of variability in the measured thicknesses. We can see this is true as the average film thickness for the different film types varies from below 400 to over 600 nm and the standard deviations are relatively large (Figure 5-4). Importantly, these film thickness measurements do not reveal any differences in film thicknesses between the different film types. As a consequence, we do not have any evidence that heat-treating the manganese oxide films (i.e., "wet" compared to "dry") or employing multiple electrodepositions (as is used for the remaining film types) results in any change in film thickness.

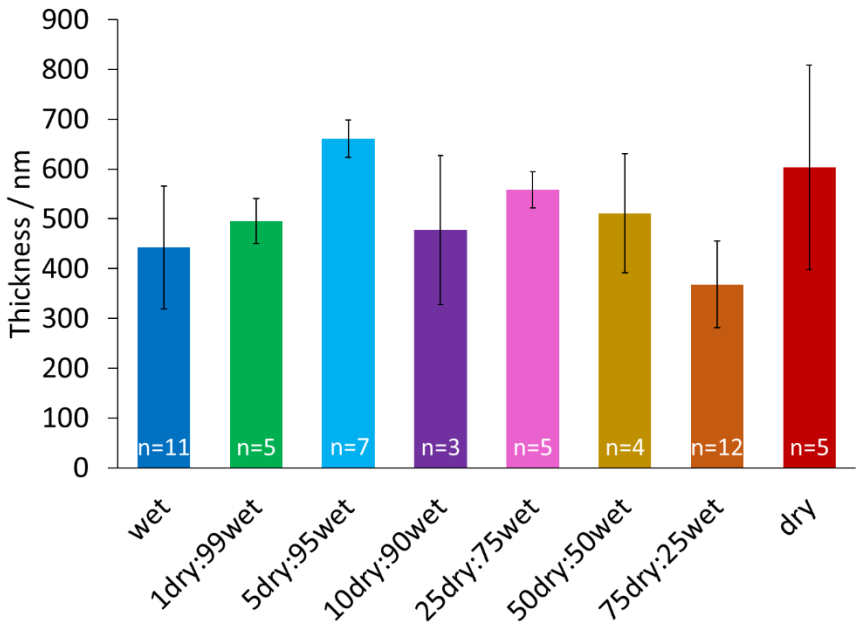

Figure 5-4. Average thickness of manganese oxide film flakes from SEM for each type of manganese oxide film, with error bars showing one standard deviation (sample size, n, is indicated on each bar).

The two methods used in this section for measuring manganese oxide film thickness yielded notably different results. Our ion-milled sample had a measured film thickness of 1200 nm, while our samples prepared by physical scraping exhibited thicknesses that were typically around 500 nm (with some variation). One possible source of this discrepancy may be the area of film that was measured in each technique. The ion-milling of the manganese oxide film occurred by removing a very thin section of the electrode at its edge. In contrast, the physically scraped samples were lifted from near the center of the film, as this was the easiest area to scrape evenly by hand. We would expect electrodeposited films to be thicker near electrode edges and corners, so this may be responsible for the discrepancy in thickness measured using these two different techniques. Additionally, our ion-milled thickness measurement is disadvantaged by the fact that we only had one sample. Notably, this evaluation of film thicknesses did not reveal any differences in manganese oxide thickness between the different film types. This is important to consider as we explore the electrochemical rate capabilities of these electrodes, as film thickness would impact rate capabilities.

5.1.3 X-Ray Photoelectron Spectroscopy

In this thesis, our electrodeposited films are referred to with the ambiguous term "manganese oxide". This is because we anticipate that the electrodeposition technique of electrode fabrication may result in a film that is a mixture manganese oxidation states (and therefore a mix of manganese oxides). As we evaluate the behaviour and

performance of these films, it will be important to understand what kind of material we are using.

In order to evaluate what kind of manganese oxides are present in our films, XPS spectra of the $Mn_{2p3/2}$ orbital were fitted with relevant manganese species. Both "wet" and "dry" manganese oxide films were tested to assess if the drying procedure used for the "dry" films results in any chemical change in the electrode material. Initially, the $Mn_{2p3/2}$ XPS data were fitted with peaks associated with MnOOH, Mn_2O_3, and MnO_2.[62] The relatively small size of the resulting MnO_2 peaks prompted an exploration of whether this oxide species should be included at all. Fittings were therefore also completed with only MnOOH and Mn_2O_3 peaks. The residuals of both fittings (with and without MnO_2) were then plotted to evaluate if the presence of the MnO_2 peaks improves the fit. For the "dry" manganese oxide film, these residuals increased when MnO_2 was excluded from the fitting (Figure 5-5a), suggesting that the MnO_2 peaks, albeit small, do improve the fit. This difference, however, was not seen in the XPS fittings for the "wet" manganese oxide films, where there was no noticeable difference in the fitting residuals with and without MnO_2 peaks (Figure 5-5b). Therefore, MnO_2 peaks were included in the final fitting for the "dry" manganese oxide films, but were excluded from the final fitting of the "wet" films.

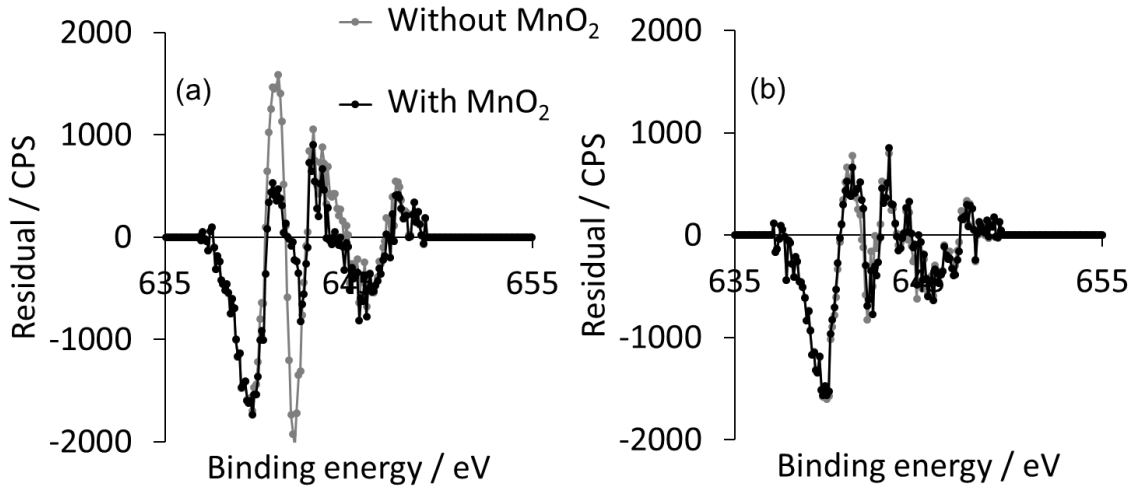

Figure 5-5. XPS $Mn_{2p3/2}$ fitting residuals in counts per second (CPS) for (a) dry and (b) wet manganese oxide films, for fittings with and without MnO_2 peaks.

The $Mn_{2p3/2}$ XPS data and fitted curve (envelope) for both types of manganese oxide films are shown in Figure 5-6 and were previously published.[70] In both cases, the envelope contribution of each manganese oxide species is also plotted. A qualitative evaluation of the peak areas for the manganese oxide species indicates that for both the "dry" film (Figure 5-6a) and "wet" film (Figure 5-6b), the most prevalent species is Mn_2O_3, followed by MnOOH. The "dry" film has a small contribution from MnO_2, whereas this is absent in the "wet" film due to the previously discussed evaluation of XPS fitting residuals.

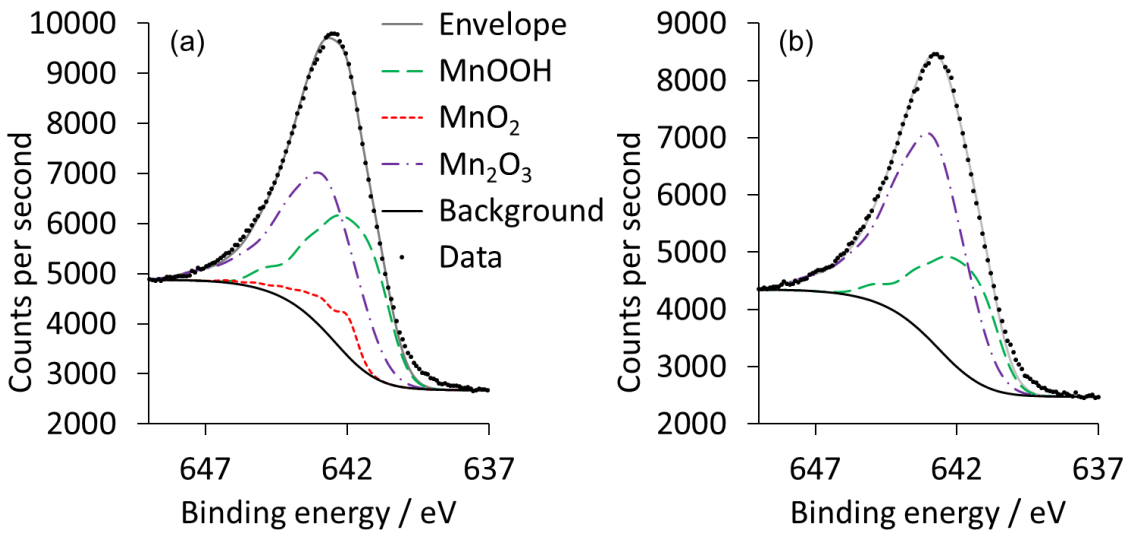

Figure 5-6. XPS $Mn_{2p3/2}$ fittings for (a) dry and (b) wet manganese oxide films, showing the contributions of each type of oxide to the overall envelope.

A quantitative analysis of the peak areas for each manganese oxide species can theoretically give us an indication of the relative amount of each species in our film. The XPS peak area percentages for the manganese species in both types of films are therefore compiled in Table 3.

Table 3. Percentage of fitted peak area contributed from each type of oxide in XPS $Mn_{2p3/2}$ fitting.

	Percentage of peak area contributed from oxide	
	"dry" manganese oxide film	"wet" manganese oxide film
Mn_2O_3	49 %	67 %
MnOOH	43 %	33 %
MnO_2	8 %	N/A

However, it is important to consider that XPS analyses of manganese species are challenging due to the multitude of possible oxidation states and overlapping peaks in the spectra. This can make the identification and quantification of manganese species somewhat unreliable. Additionally, there is limited reputable literature on fitting protocols for different manganese species. For instance, we expect that our drying protocol will decrease hydration in our films, however there is no detailed $Mn_{2p3/2}$ XPS fitting protocol for hydrous versus anhydrous manganese oxide species. Therefore, we cannot be certain that the manganese species evaluated in this XPS analysis are the only possibilities for our films. We can infer, however, that the relatively good fit of the species evaluated herein points towards their respective manganese oxidation states being probable in our films. Therefore, this XPS analysis suggests that our manganese oxide films likely contain a mixture of Mn^{3+} and Mn^{4+} oxidation states.

5.1.4 Other Characterization

Other physical and chemical characterization of these types of manganese oxide films (wet, dry, and 10dry:90wet films on stainless steel) have been published previously by the Andreas group.[71] To summarize, heat-treatment increases the film physical stability, but also removes hydration sites in the oxide, lowering the measured pseudocapacitance. Thus, the heat-treatment used herein is an effective means of altering the pseudocapacitive response without changing the oxide's oxidation state or physical structure. The films were also found to be composed of amorphous platelets, which means that other physical characterization techniques such as X-ray diffraction

spectroscopy (which requires crystalline materials) cannot be used to evaluate the oxide composition of the films. Therefore, we must rely on XPS fittings (as seen in the previous section) to give us insight into what types of manganese species may be present in our electrodeposited films.

5.2 Origin of Interfacial Resistance in Manganese Oxide Films

Because of inconclusive results in the literature regarding the origin of semi-circles in Nyquist plots of manganese oxide, EIS of "wet", "dry" and "10dry:90wet" manganese oxide films on stainless steel as well as manganese oxide films on platinum foil were studied. A detailed description of how these different films were made can be found in Section "3.2.3 Manganese Oxide Electrodeposition".

The Nyquist plots (Figure 5-7a) of all manganese oxide films exhibit an upright tail characteristic of a capacitive process, as is expected for this pseudocapacitive material. Despite the fact that the amount of manganese oxide on each electrode is controlled by deposition charge in the electrodeposition (i.e., the same amount of manganese oxide is deposited on each electrode) the capacitance, as measured by cyclic voltammetry (Figure 5-7b), is lower for the "dry" film (79 ± 3 mF) compared to the other film types. This lower capacitance is as expected for manganese oxide with fewer hydration sites.[71] To compare, the more hydrated films on stainless steel exhibit capacitances of 152 ± 1 mF ("wet" film) and 142 ± 6 mF ("10dry:90wet"). As anticipated, the length of the capacitive tail in the EIS Nyquist plot is inversely related to

the measured pseudocapacitance, where the lower-capacitance "dry" film results in a longer capacitive tail (Figure 5-7a).

A large semi-circle is evident in the Nyquist plot of the "wet" manganese oxide films deposited on stainless steel (SS/$MnOx_{wet}$, Figure 5-7a). Semi-circles are often attributed to the charge-transfer resistance of the pseudocapacitive reaction;[13,35–41] however, the "dry" films exhibit less than 1% of the semi-circle size (SS/$MnOx_{dry}$, Figure 5-7a), despite having ~50% of the capacitance of the "wet" films (Figure 5-7b). Note that the "10dry:90wet" films have the same substrate connection as the "dry" films and – since the pseudocapacitive reaction takes place in the outer film layer[13,14,72,73]– they have the same pseudocapacitive-active outer layer as the "wet" films. Because the "wet" and "10dry:90wet" films have the same active outer layer, they exhibit similar pseudocapacitance (Figure 5-7b), however the size of the Nyquist semi-circles is very different (Figure 5-7a). Thus, the degree of pseudocapacitance does not correlate with Nyquist semi-circle size; and, the semi-circle cannot be governed by the pseudocapacitive reaction, as suggested previously.[13,35–41]

The other significant difference between the "wet" and "dry" films is the interface between the manganese oxide and stainless steel, as heat-treatment may improve the contact between the film and its substrate.[71] Although the "10dry:90wet" films have a pseudocapacitive layer that matches the "wet" films, their substrate connection is the same as the "dry" films. The Nyquist semi-circle size is similar for the films with similar film-substrate interfaces (SS/$MnOx_{dry}$ and SS/$MnOx_{10dry:90wet,}$ Figure 5-7a) and is very different for the films where the pseudocapacitive layer is the same but the film-substrate

interface is different (SS/MnOx$_{wet}$ and SS/MnOx$_{10dry:90wet}$, Figure 5-7a). Clearly, improving the interface between the manganese oxide and its substrate removes more than 99% of the semi-circle present in Nyquist plots of wet films on stainless steel. Thus, these data show that the size of the Nyquist semi-circle for pseudocapacitive manganese oxides is dominated by the interface between the oxide and the substrate on which it was deposited, not due to charge-transfer resistance as is commonly suggested in the current literature.

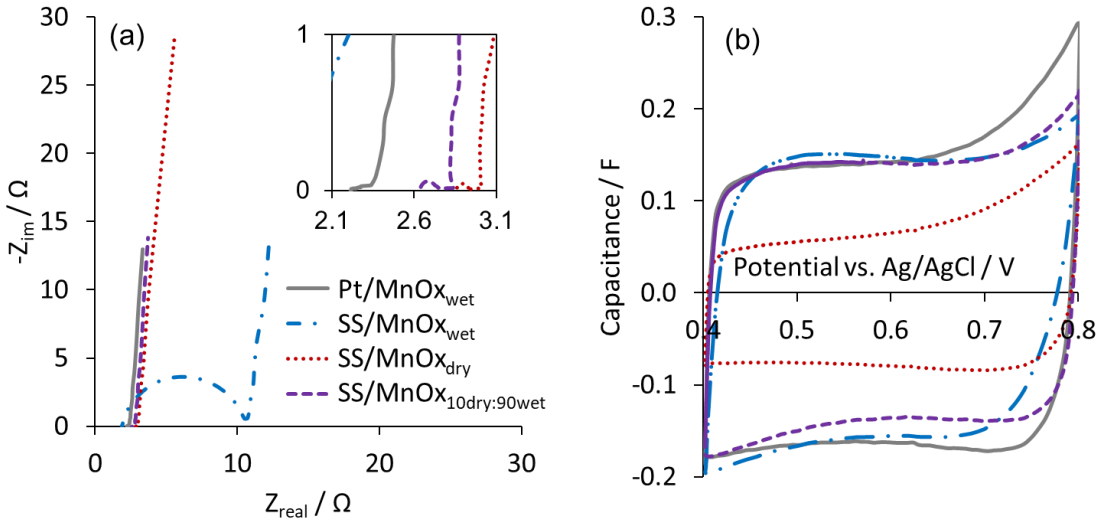

Figure 5-7. (a) Representative Nyquist plots with inset showing enlarged version of the high frequency region and (b) representative differential capacitance plots derived from steady-state cyclic voltammograms of manganese oxide films recorded in 0.5 M Na_2SO_4.

Since the previous data suggest that the interface is the key source of the Nyquist plots semi-circle, this will be further confirmed by changing the electrodeposition substrate to a different metal (e.g., Pt), which should in turn change the film-substrate interface. Platinum was chosen for the substrate since it is a noble metal, with no native

oxide, and because it is a good substrate for electrodeposition. “Wet” manganese oxide films were studied on this substrate ($Pt/MnOx_{wet}$). These films have the same degree of hydration as the wet films on stainless steel ($SS/MnOx_{wet}$) and similar pseudocapacitive values (161 ± 7 mF); however, the film-substrate interface is different. This interface difference is reflected in the Nyquist plots, wherein there is only a small, indistinct semi-circle ($Pt/MnOx_{wet}$, Figure 5-7a). Clearly, changing the interface at the substrate is the source of the Nyquist plot semi-circles for these pseudocapacitive materials. In the “dry” manganese oxide films, the heat-treatment has decreased the resistance between the manganese oxide and stainless steel to a magnitude similar to that between manganese oxide and platinum. This is the first time it is shown in literature that the semi-circle commonly attributed to the pseudocapacitive reaction may actually be due to the substrate-oxide interface. This finding may lead to a fundamental rethinking of how Nyquist plots of pseudocapacitive materials are analysed.

To examine the frequency dependence of the various manganese oxide films, real and imaginary capacitances[43,44] were calculated from the EIS data (Figure 5-8). The “dry” films present a low-frequency plateau in the real capacitance plot (Figure 5-8a) with a much smaller capacitance value compared to the “10dry:90wet” films. This is consistent with hydration resulting in a higher capacitance in pseudocapacitive metal oxides due to more facile cationic access to the pseudocapacitive films.[3,9,71] Wet films deposited on stainless steel exhibit a low capacitance but do not exhibit a plateau, suggesting they do not access all of their active material even at the very low frequencies tested in this EIS measurement. The low capacitance is therefore not due to a lack of

active material but is related to a low rate-capability for the reaction. Recall that the morphology of all these different film types appears to be the same (Figure 5-1) and there was no measurable difference in their thicknesses (Figure 5-4). Therefore, it is likely that the high resistance due to poor substrate contact in the "wet" films hinders (i.e., slows) access to the active material lowering both the frequency response and the capacitance. Films that have a less resistive interface and a thick layer of hydrated manganese oxide ($SS/MnOx_{10dry:90wet}$ and $Pt/MnOx_{wet}$) exhibit both a faster frequency response and higher capacitance (Figure 5-8a).

Similar conclusions can be drawn from the imaginary capacitance plot (Figure 5-8b). The smaller peak size of the "dry" film reflects the lower capacitance of dehydrated manganese oxide while the peak of the "wet" film on stainless steel positioned at a lower frequency is reflective of the high resistance between the film and substrate, hindering the film's ability to react quickly. The "10dry:90wet" film on stainless steel presents an imaginary capacitance peak of a similar area (i.e., similar capacitance) and similar peak position (i.e., similar RC time constant) as the wet film on platinum foil. Clearly, heat-treating improves the interface between manganese oxide and stainless steel to a level comparable to that of manganese oxide on platinum (an oxide-free substrate), confirming that contact between the manganese oxide and substrate is the most important variable to improve frequency response in these electrodes. This improved frequency response means these systems could access more manganese oxide material at fast rates, meaning they could store more energy in the high-power applications in which ECs are often used.

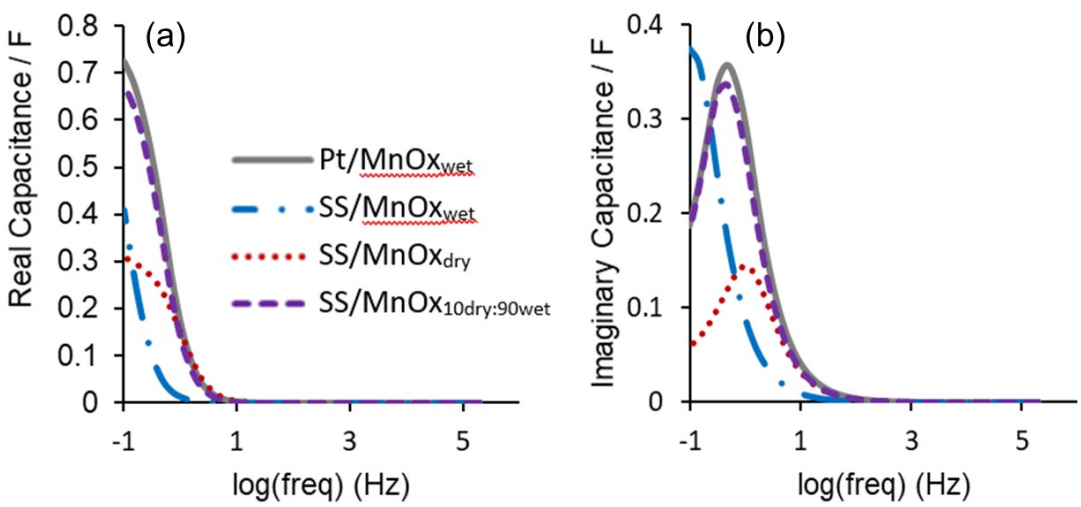

Figure 5-8. Representative (a) real capacitance and (b) imaginary capacitance from EIS data of manganese films recorded in 0.5 M Na_2SO_4.

5.2.1 Additional Control Experiments

Some additional experiments were conducted to ensure that the semi-circle detected in the SS/$MnOx_{wet}$ films originated from the interface between manganese oxide and its substrate, rather than other components of the experimental set-up. For example, EIS of SS/$MnOx_{wet}$ films was measured where some of the stainless steel substrate was also exposed to the electrolyte. Because this bare stainless steel was usually sealed using parafilm, another film was tested where parafilm was used to cover the bare stainless steel but was poorly sealed, allowing electrolyte to wick underneath the parafilm. Neither of these scenarios influenced the size of the semi-circle in the Nyquist plot of the manganese oxide film.

EIS of bare stainless steel was also recorded. Tested conditions include: bare stainless steel, bare stainless steel that was heat-treated at 200 °C for 2 hours (same drying conditions as the SS/$MnOx_{dry}$), and bare stainless steel shat was heat-treated in an

oven that also had manganese oxide films present. None of these bare stainless steel samples presented a semi-circle in their Nyquist plots. Additionally, manganese oxide films that were deposited on stainless steel that had previously been heat-treated yielded Nyquist plot semi-circles similar in size to those normally recorded for $SS/MnOx_{wet}$ films. Therefore, the decrease in semi-circle size observed for the $SS/MnOx_{dry}$ and $SS/MnOx_{10dry:90wet}$ compared to the $SS/MnOx_{wet}$ stems from an improvement in the contact between the manganese oxide and stainless steel, and not from a change in the stainless steel itself.

5.2.2 Interfacial Resistance in Other Dry:Wet Ratio Films

Earlier in this section, we explored how the EIS response of "wet", "dry", and "10dry:90wet" films varied. From this, we concluded that the interface between the substrate and electrode material was the source of resistance in these electrodes' Nyquist plot semi-circles. However, it is worth exploring how altering the ratio of dry to wet film in these electrodes may impact this interfacial resistance. This subsection will explore exactly this. Note that all of the electrodes studied in this section used stainless steel as a substrate.

Recall that the semi-circle in manganese oxide Nyquist plots gives us a measure of the resistance between the manganese oxide and its substrate, where a larger semi-circle indicates higher resistance. Representative EIS Nyquist plots for a range of dry:wet ratio manganese oxide films are shown in Figure 5-9. Note that the "wet", "dry", and "10dry:90wet" data from earlier in this section is included in this plot for easier

comparison. We can see from the Nyquist plot that an electrode with 1% of the deposited manganese oxide in a dried layer (and the remaining 99% deposited on top) has a substantially smaller Nyquist semi-circle compared to a fully "wet" film (Figure 5-9a, "1dry:99wet" and "wet"). This indicates that the presence of this thin heat-treated layer (proportional to only 1% of the total charge passed in electrodeposition) is improving the contact between the manganese oxide film and the stainless-steel substrate. However, an enlarged view of the semi-circle region (Figure 5-9b), shows that the semi-circle for the "1dry:99wet" manganese oxide electrode is still noticeably larger than electrodes with larger dried films. This suggests that the contact resistance between the manganese oxide and its substrate has not been optimally minimized in the "1dry:99wet" manganese oxide film.

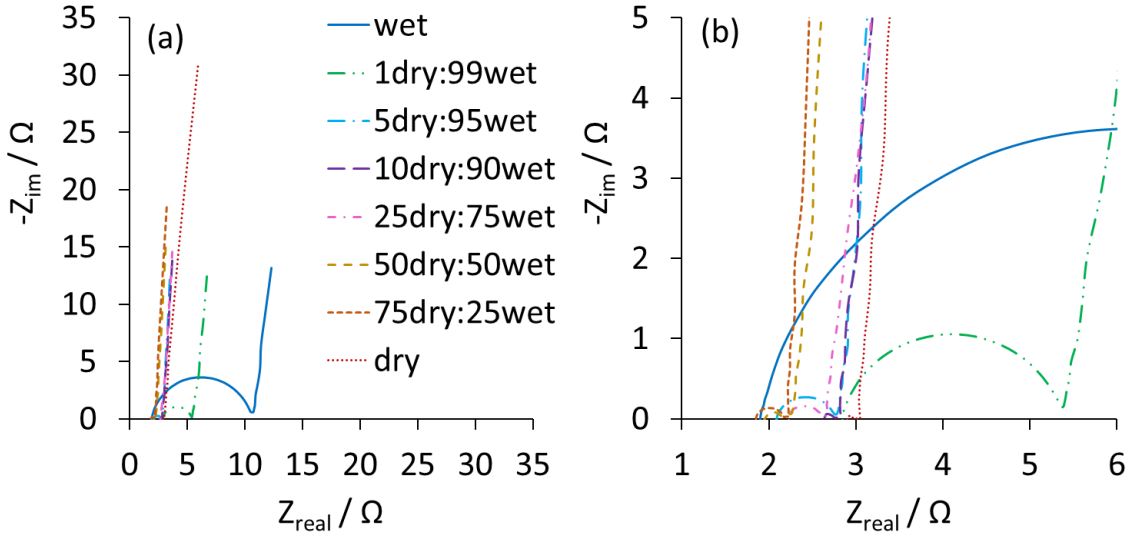

Figure 5-9. (a) Representative EIS Nyquist plots for various dry:wet ratio manganese oxide films on stainless steel with (b) an enlarged version better showing the semi-circle region.

To better compare the resistance between these different manganese oxide films and their substrates, the resistance associated with Nyquist plot semi-circles was averaged for each dry:wet manganese oxide ratio (Figure 5-10). From this, we can see that the "1dry:99wet" manganese oxide films do indeed offer improved resistance versus the films that have no heat-treated manganese oxide layer (Figure 5-10, "1dry:99wet" and "wet"). There is, however, another measurable decrease in resistance when upon increasing the dried film layer to be 5% of the overall charge passed in the manganese oxide electrodeposition (Figure 5-10, "5dry:95wet"). For films with dried manganese oxide layers of 5% and above, there is no difference in the interfacial resistance between manganese oxide and its substrate (note that the error bars in Figure 5-10 represent only one standard deviation). While we had previously confirmed that the dried layer of manganese oxide was critical for minimizing the resistance between manganese oxide and its substrate, this work suggests that there exists a critical thickness that the dried layer must achieve to be maximally effective.

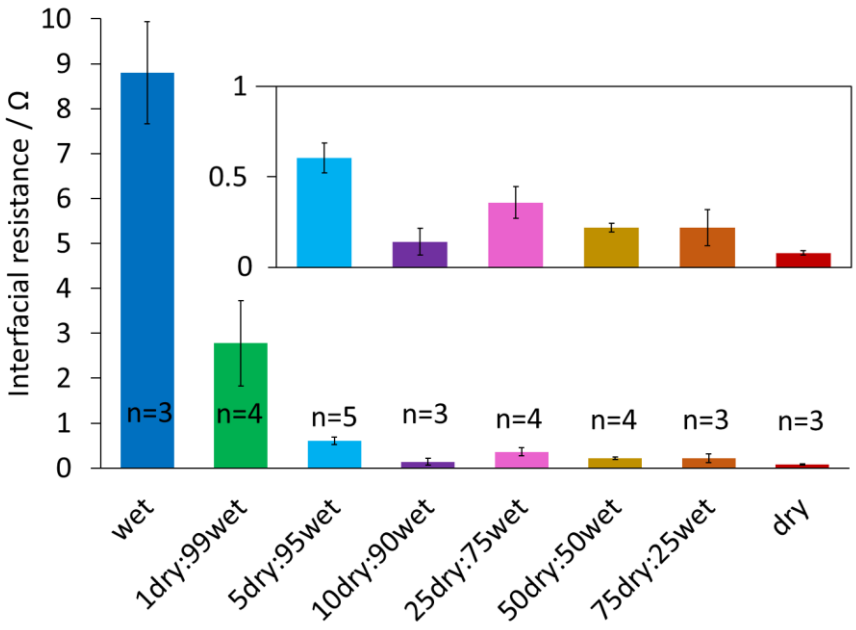

Figure 5-10. Average interfacial resistance (from EIS Nyquist plot semi-circle) for each manganese oxide film type, with an inset showing a magnified version of the last six film types (note that the error bars represent one standard deviation and "n" indicates the sample size for each category).

Because the resistance between the manganese oxide film and its substrate was measurably different for the "1dry:99wet" and "5dry:95wet" films, an investigation of the dry portion of these films was prompted. SEM images of a 1% dry film and a 5% dry film on stainless steel are shown in Figure 5-11a and Figure 5-11b, respectively. In both images, we can see the platelet structure characteristic of our electrodeposited manganese oxide films. However, in the 1% dry layer (Figure 5-11a), we can see that the manganese oxide platelets are not entirely covering the smooth stainless steel. In the 5% dry layer (Figure 5-11b), the SEM image shows that the manganese oxide platelets are covering the stainless steel much more thoroughly. It therefore stands to reason that when the second layer of manganese oxide is deposited, the 1% dry layer will have only some of the new

manganese oxide depositing on dried manganese oxide, whereas some will deposit on exposed stainless steel. With the 5% dry layer, newly electrodeposited manganese oxide will be growing on dried manganese oxide, rather than the stainless steel. This explains why the "1dry:99wet" only offer a marginal improvement in interfacial resistance compared to the "wet" electrodes, while the "5dry:95wet" reach similar interfacial resistance values to films with larger dry manganese oxide layers.

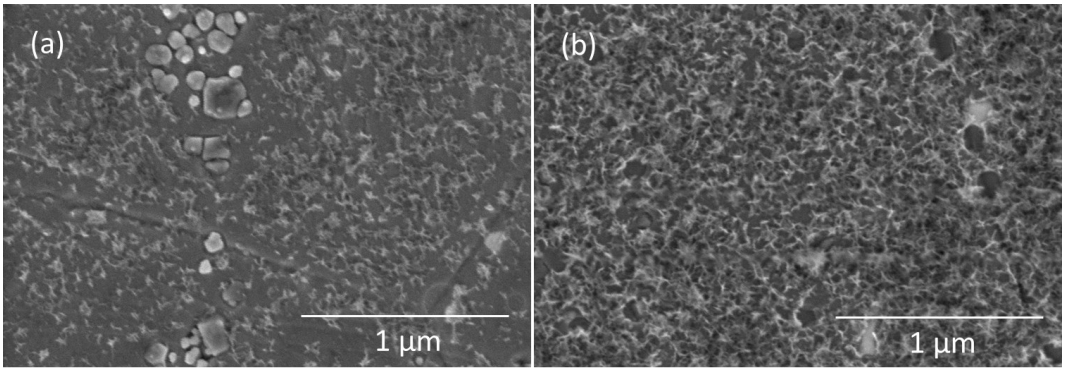

Figure 5-11. SEM images of (a) a "1dry" layer and (b) a "5dry" layer of manganese oxide on stainless steel at 50 000 times magnification.

We have learned herein that, while the dry layer is important for improving the connection between manganese oxide and its substrate, this dried layer of manganese oxide must be adequately thick that it covers the substrate well. Otherwise, as was seen with our "1dry:99wet" films, the resistance associated with this interface will not be minimized as much as it could be. For the dry:wet manganese oxide ratios studied in this section, we saw the lowest interfacial resistance when 5% or more of the charge passed in the electrodeposition of manganese oxide was allocated to the dry film. If we consider our estimated full-film thicknesses from Figure 5-4 to be accurate, we can estimate that

our 5% layer is approximately 25 nm. The lower resistance seen in films with 5% or more dried manganese oxide will consequently improve the rate capabilities of these electrode, which is an important parameter for electrochemical capacitor systems.

We must also consider, though, how the dry:wet ratio may impact the energy storage capacity of the electrodes. Since we know that hydrated manganese oxide should be able to store more energy, [71] we might expect that films with more "wet" manganese oxide will have higher energy storage capacity. Other electrochemical data published by our group for these different manganese oxide films reveal that this is in fact the case, but only up until a certain threshold; there was no further improvement in the energy storage capacity after attaining 95% "wet" manganese oxide in the film. However, the "wet" and "1dry:99wet: films experienced increased instability and a decrease in power compared to the "5dry:95wet" films.[70] We can therefore conclude that, of the dry:wet manganese oxide ratios tested, the "5dry:95wet" film are optimal. This is due to their minimized interfacial resistance between the dried manganese oxide and its substrate as well as their thick hydrous layer of manganese oxide maximizing their energy storage capacity.

5.3 Considerations for Manganese Oxide Circuit Models

In this chapter so far, we have explored Nyquist and complex capacitance representations of manganese oxide EIS data, which are both helpful for visualizing different figures of merit. Another technique for extracting figures of merit from EIS data is fitting the data with circuit model, as is explained in Section "2.4.1 Equivalent Electrical Circuit Models". Circuit model fittings, which are commonly employed in the

literature, fit virtual electrical circuits to EIS data points, yielding numerical values for each circuit element. Additionally, circuit models that fit data well can also be used to support hypotheses for how a system functions. However, choosing a circuit model can be difficult due to the wide variety of options employed in the literature.

In this section, we will walk through an in-depth analysis to determine what circuit model best represents our pseudocapacitive manganese oxide. Because we will be examining common pseudocapacitive circuit models herein, we have chosen to fit these models to our "wet" manganese oxide EIS data, as they most closely resemble what is typically seen for pseudocapacitive EIS data in the literature. In our analysis, we will explore circuits that are recommended for pseudocapacitive systems and widely employed in the literature and show how we can narrow down these options to the most suitable model for our system.

Before fitting circuit models to our EIS data, it is important to first establish that our EIS data are valid, meeting the EIS assumptions of being stationary and having a linear relationship between potential and current. To do this, we can fit a measurement model to our data to ensure that subsequent circuit fittings are valid, as is described in more detail in Section "2.4.4 Measurement Considerations". The measurement model used in this project was a Voight circuit comprised of 12 Voight elements (see Figure 2-11) and we sought relative residual errors of less than 3% from our fitting (a standard used in other measurement model evaluations of Kramers-Kronig compliance[74]). The fit of this Voight circuit to the Nyquist plot of a "wet" manganese oxide electrode and the resulting relative residual errors is shown in Figure 5-12. This fitting resulted in relative

residual errors that were less than three percent at most of the measurement frequencies, except for the imaginary capacitance residuals for the four highest-frequency data points (Figure 5-12b). Note that these high-frequency data points correspond to the beginning of the Nyquist plot semi-circle (see Figure 5-12a) and therefore have very small imaginary impedance values. This means that even small inaccuracies in the fitted values can result in high relative residual error. Nevertheless, if our measurement model cannot achieve low residual errors at these data points, we cannot expect other circuit models to be able to do so. Therefore, the four highest-frequency data points are excluded from the rest of the circuit fittings presented in this section.

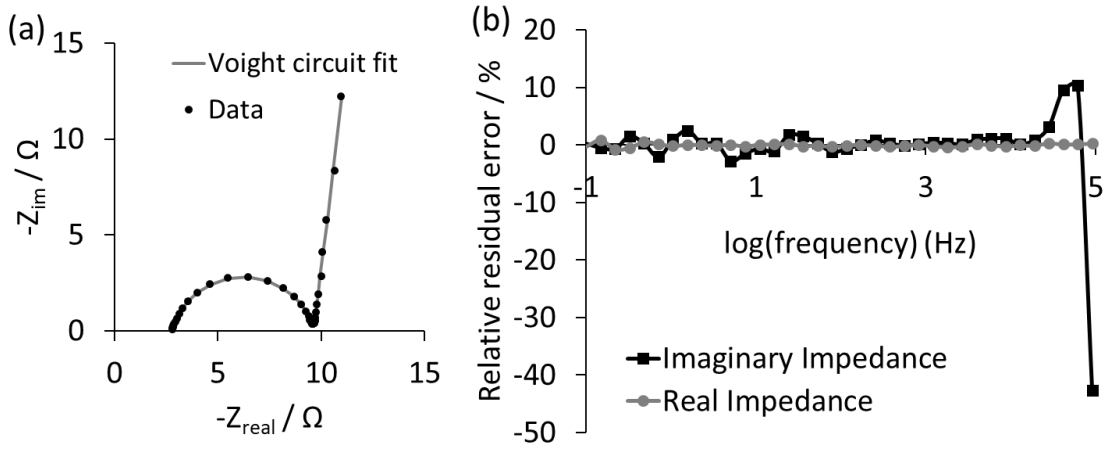

Figure 5-12. Relative residual error of imaginary and real impedance from fitting EIS of a "wet" manganese oxide film with a 12 Voight element measurement model circuit.

When selecting a circuit model for EIS data, there are a few considerations that should be made. Fistly, the circuit should be reasonable for the given electrochemical system. Each circuit element should relate to an expected process in the system and the circuit should be kept as simple as is reasonable to avoid "overfitting" the data from an

excess of fitting variables. Additionally, the goodness of fit for the circuit should be considered. Although circuit models will likely not fit EIS data perfectly, especially large residual errors may suggest that the circuit does not adequately describe the electrochemical system. Lastly, it can be helpful to consider the fitted values for each circuit element. If a certain circuit element yields a physically irrelevant value, this would indicate that this circuit element is not serving its intended purpose and should be excluded from the model.

Circuit models that are commonly used for pseudocapacitive materials are presented in Figure 5-13 and are based on textbook recommendations for pseudocapacitive systems.[75] Of these, the most simplistic is circuit 1, which consists of resistor followed by a parallel unit consisting of a capacitor on one side and a resistor and capacitor on the other side (Figure 5-13a). Recall from Chapter 2 that having a capacitor and resistor in parallel results in a semi-circle shape in a Nyquist plot, while the extra capacitor in series with a resistor will result in an upright tail (see "Circuit 3" in Figure 2-9). This circuit should therefore result in approximately the right shape to fit our "wet" manganese oxide EIS data. However, it is important to take into account that the capacitive processes in our system may not be behaving as ideal capacitors. In this case the capacitors could instead be modelled by constant phase elements (CPE), as is described in Section "2.4.1 Equivalent Electrical Circuit Models". Therefore, we will also consider a circuit where the first capacitor is replaced by a constant phase element (Figure 5-13b), a circuit where the second capacitor is replaced (Figure 5-13c), and a circuit where both capacitors are constant phase elements (Figure 5-13d). In order to

determine which of these circuits may best model our “wet” manganese oxide electrodes, we will need to carefully consider how they fit our electrochemical data.

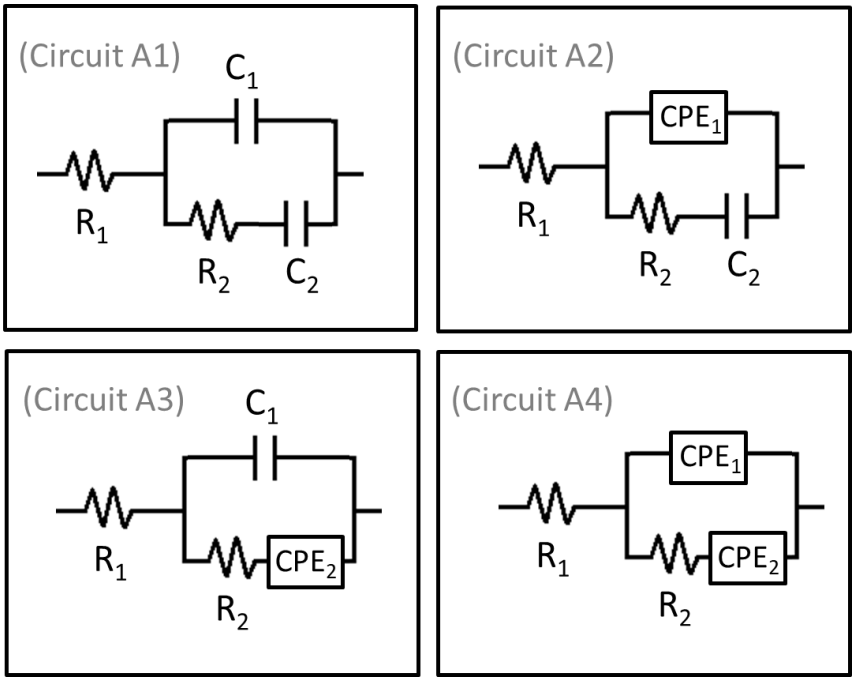

Figure 5-13. EIS circuit models commonly applied to pseudocapacitive electrochemical system, with resistors (R), capacitors (C), and constant phase elements (CPE) labelled accordingly.

The Nyquist plot fit and resulting relative residual errors for each of these circuits will be important to consider in determining which circuit best models our electrochemical system. For circuit A1 (Figure 5-13a), which only has capacitors and no constant phase elements the Nyquist plot fit is visibly poor (Figure 5-14a), with relative residual errors that reach well over 30% (Figure 5-14b). This suggests that one or both of the capacitive processes in our electrochemical system may not be behaving as an ideal capacitor and may therefore be better modelled by a constant phase element.

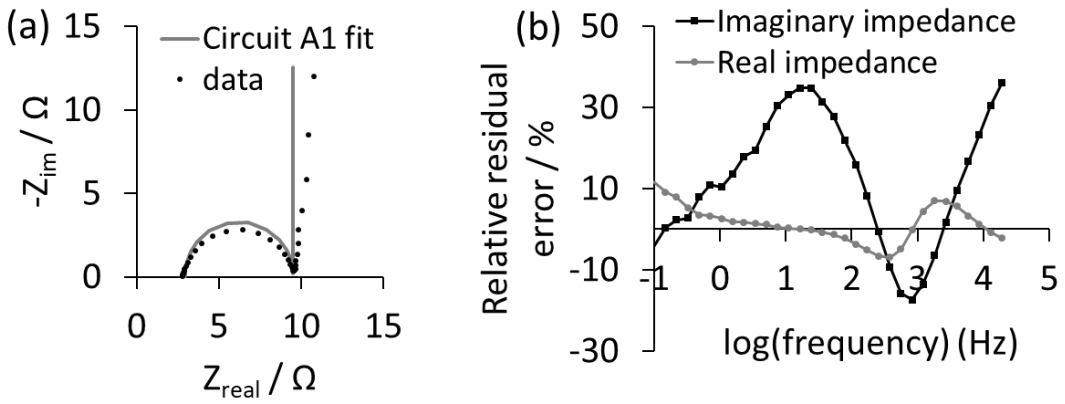

Figure 5-14. (a) Nyquist plots fit and (b) relative residual errors for "wet" manganese oxide EIS data fit to circuit A1.

Circuit A2 (Figure 5-13b), has the first capacitor, which is associated with the Nyquist semi-circle, replaced by a constant phase element. This circuit does better fit the semi-circle region in the Nyquist plot, but the fit in the tail region is still visibly poor (Figure 5-15a). The relative residual errors for this circuit reach well over 10% in the low frequency region (Figure 5-15b), indicating that circuit A2 does not fit our data adequately well.

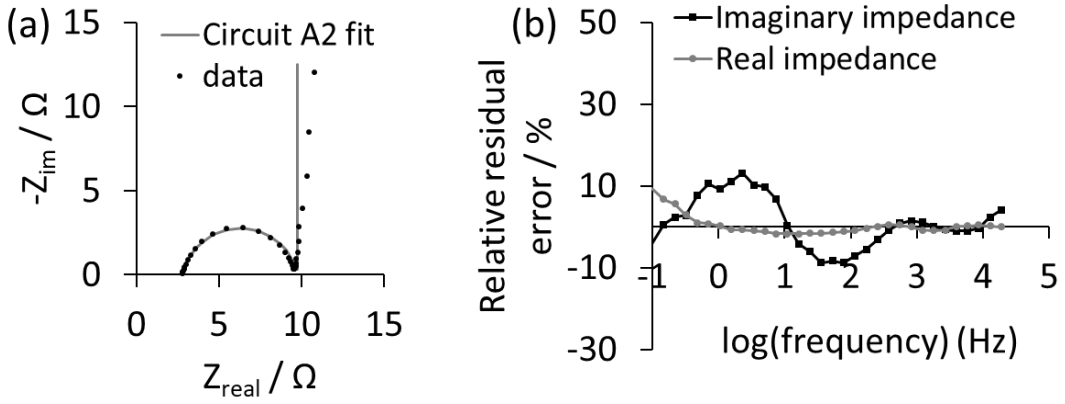

Figure 5-15. (a) Nyquist plots fit and (b) relative residual errors for "wet" manganese oxide EIS data fit to circuit A2.

Circuit A3 (Figure 5-13c) has a capacitor for the process associated with the semi-circle, but it has a constant phase element for the capacitive process associated with the Nyquist plot tail. The fitted data for this circuit does better fit the tail region of the Nyquist plot but is visibly inaccurate in the semi-circle region (Figure 5-16a). As a result, this fitting results in large relative residual errors, reaching over 30% at some frequencies (Figure 5-16b). This poor fit suggests that it is not sufficient for only one of the capacitors in our circuit model to be replaced by a constant phase element.

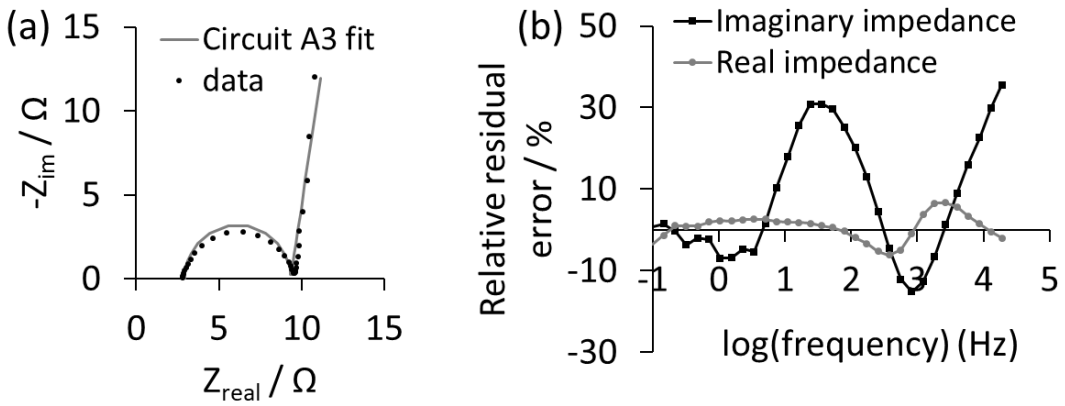

Figure 5-16. (a) Nyquist plots fit and (b) relative residual errors for "wet" manganese oxide EIS data fit to circuit A3.

Circuit A4 (Figure 5-13d) has constant phase elements in place of both capacitors. This circuit is able to accurately fit our EIS data (Figure 5-17a). For the majority of the EIS measurement, the relative residual error remains below 3%, with the exception of the two highest-frequency data points, which have slightly elevated relative residual errors (Figure 5-17b). Nevertheless, circuit A4 provides an overall excellent fit for our EIS data. This suggests that both of the capacitive processes in our system are not behaving as ideal

capacitors and require constant phase elements to be accurately modelled. Of the circuits tested thus far, circuit A4 (Figure 5-13d) is the best model for our "wet" manganese oxide electrodes.

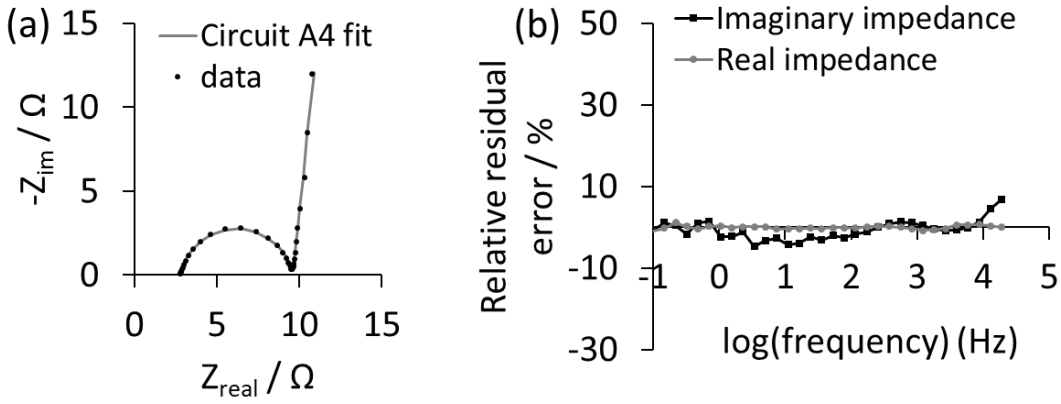

Figure 5-17. (a) Nyquist plots fit and (b) relative residual errors for "wet" manganese oxide EIS data fit to circuit A4.

Another circuit that is commonly used in the literature for pseudocapacitive systems, is one that includes a Warburg element in addition to the circuit elements included in circuit A4 (Figure 5-18). Recall that a Warburg element models diffusion-controlled electrochemical behaviour and results in a characteristic 45° tail in Nyquist plots. Notably, we do not expect diffusion-controlled electrochemistry to be occurring in our system (and, in fact, we do not see a 45° tail in our Nyquist plots). However, it is important to consider how this circuit might fit our data, since it is a common pseudocapacitive circuit in the literature[36,38,40,76] and may therefore be considered by researchers seeking a circuit model for their pseudocapacitive electrochemical system.

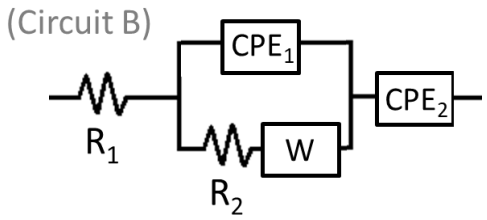

Figure 5-18. Common pseudocapacitive EIS circuit model that includes a diffusion element, with resistors (R), capacitors (C), constant phase elements (CPE), and Warburg element (W) labelled accordingly.

If we fit circuit B (Figure 5-18) to our "wet" manganese oxide EIS data, the Nyquist plot fit shows a good fit (Figure 5-19a), with relative residual errors that are largely less than 3%, save for a couple data points at high frequencies (Figure 5-19b). However, one may notice that the relative residual error profile for circuit B (Figure 5-19b) looks strikingly similar to the fitted data for circuit A4 (Figure 5-17b). In fact, the inclusion of the Warburg element in circuit B has barely changed the fit at all, with both the shape and magnitude of the relative residual errors remaining nearly identical to those of circuit A4 (see Figure 5-19b and Figure 5-17b)

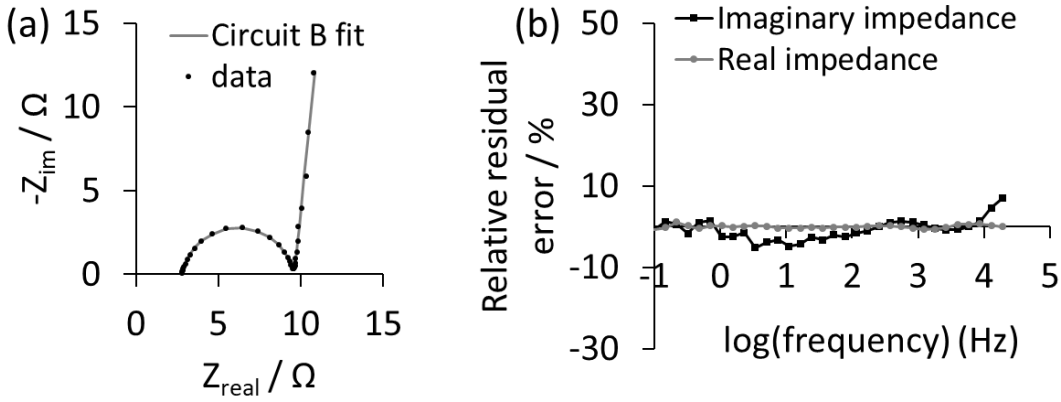

Figure 5-19. (a) Nyquist plot fit and (b) relative residual errors for "wet" manganese oxide EIS data fit to circuit B.

The lack of difference in the fitting residuals between circuit B (Figure 5-19b) and circuit A4 (Figure 5-17b) raises the question of whether the Warburg element in Circuit B (Figure 5-18) should be included at all. An examination of the fitted values for each circuit element can help us evaluate if this is the case. If we consider the circuit elements that circuit A4 and circuit B have in common, we can see that there is very little difference in the fitted values (Table 4). Additionally, the fitted value for the Warburg element in Circuit B is very small (Table 4). These observations paired with the fact that including this Warburg element has not substantially changed the fitting residuals (see Figure 5-19b and Figure 5-17b) suggests that circuit B is not appropriate for our particular electrochemical system.

Table 4. Circuit element values from fitting "wet" manganese oxide EIS data with circuit A4 and circuit B.

Circuit	**R_1 / Ω**	**CPE_1 / $F \cdot s^{(n-1)}$**	**n_1**	**R_2 / Ω**	**CPE_2 / $F \cdot s^{(n-1)}$**	**n_2**	**W / $\Omega * s^{1/2}$**
A4	2.789	$1.116*10^{-4}$	0.8690	6.823	0.1268	0.9330	-
B	2.789	$1.110*10^{-4}$	0.8694	6.810	0.1275	0.9351	0.02947

From our analysis of the EIS fitting residuals and consideration of the fitted values for each circuit element, we can conclude that circuit A4 remains the most appropriate circuit model for our manganese oxide electrode. Going through this processing while selecting a circuit model was important. Circuit B fits our data well and, had we not considered the fitting values for the circuit elements and compared the fitting

residuals to other circuits, we may have wrongly assigned this circuit to our system. A careful analysis of multiple circuits is therefore helpful in identifying the circuit that best suits EIS data.

For each circuit element that is used in a circuit model, it is important to be able to identify what physical process it represents. In textbooks and the literature, R_1 in circuit A4 (Figure 5-13d) is attributed to solution resistance (or, sometimes, "equivalent series resistance"). This represents sources of resistance such as the electrolyte, wires, etc. and is appropriate for our system. Our fittings therefore indicate that our system has an equivalent series resistance of 2.789 Ω. The second resistor, R_2, is responsible for the Nyquist semi-circle and is typically attributed to the charge transfer resistance in manganese oxide's pseudocapacitive reaction. However, we know from data presented in this chapter that our Nyquist semi-circle is caused from poor contact between our manganese oxide and its substrate. Therefore, the R_2 in our circuit is associated with contact resistance. Importantly, this means the resistance of 6.823 Ω associated with this resistor is not from manganese oxide's pseudocapacitive reaction, but rather a contact resistance at the electrode-substrate interface. The constant phase element across from this resistor (CPE_1) is also associated with the Nyquist semi-circle and is customarily assigned as capacitance from the electrochemical double layer, as this would exist at the same interface (the electrode-electrolyte interface) as a charge transfer resistance. However, since we know that our resistance is occurring at the electrode-substrate interface, our CPE_1 must be associated with charge separation at the electrode-substrate interface due to the poor contact between the manganese oxide and stainless steel. The

final constant phase element (CPE_2) is typically assigned as capacitance from manganese oxide's pseudocapacitive reaction. This is appropriate for our system, and the relatively large capacitance and high n-value (0.1268 $F \cdot s^{(n-1)}$ and 0.9330, respectively) support this assignment (recall that an n-value of 1 is an ideal capacitor). This analysis confirms that the circuit elements included in circuit A4 (Figure 5-13d) makes sense for our "wet" manganese oxide electrodes.

In circuit models, it is also important to consider the arrangement of circuit elements to ensure that they best describe the system at hand. the placement of this circuit element after R_2 is done so because R_2 is typically though to be charge transfer resistance, making both R_2 and CPE_2 linked to manganese oxide's pseudocapacitive reaction. However we know that, in our system, this resistor and constant phase element represent processes occurring in different regions of the system; R_2 is from contact resistance at the electrode-substrate interface and CPE_2 is associated with capacitance from manganese oxide's pseudocapacitive reaction, which occurs predominately at the electrode surface. Therefore, we propose that a more appropriate arrangement of these circuit element would be that of circuit C (Figure 5-20), where CPE_2 is moved to be after the parallel circuit elements associated with the Nyquist semi-circle (R_2 and CPE_1). Note that changing the arrangement of circuit elements in this way does not substantially alter the EIS fitting residuals or circuit element fitted values as was presented for circuit A4 (Figure 5-17b and Table 4). However, this rearrangement gives a more intuitive description of the processes occurring in the system, so it more clearly serves the function of a circuit model, which is to help describe electrochemical processes clearly.

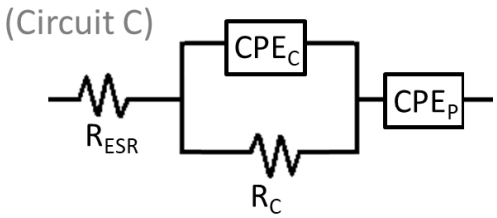

Figure 5-20. Proposed circuit model for our pseudocapacitive "wet" manganese oxide electrodes, with equivalent series resistance (R_{ESR}), contact resistance (R_C), constant phase element for contact capacitance (CPE_C), and constant phase element for pseudocapacitance (CPE_P) labelled accordingly.

While circuit C best describes our "wet" manganese oxide electrodes, it is important to consider that not all pseudocapacitive systems will be well represented by the same model. For example, a system that results in an EIS Nyquist plot without a measurable semi-circle would not require the parallel resistor and constant phase element associated with poor contact at the electrode-substrate interface (R_c and CPE_c in Figure 5-20). This is why a methodical exploration of potential circuit models, as is described in this section, is important when seeking a circuit model to represent EIS data.

5.4 Conclusions

This work shows for the first time that a semi-circle in the Nyquist plot for pseudocapacitive manganese oxides is due to oxide-substrate interface resistance rather than the charge-transfer resistance, as is commonly suggested in the current literature.[13,35–41] By varying and controlling the interface and by separating the interface and pseudocapacitive responses, we show a minimized interface resistance (e.g., by using a Pt substrate) almost entirely eliminates the Nyquist semi-circle. The interface resistance between manganese oxide and stainless steel is reduced by 99% by heat-treating the

manganese oxide film but results in a lower capacitance due to decreased hydration. A manganese oxide film composed of a heat-treated base layer (10% of the film) and a thick hydrated layer (90%) maintains the high capacitance of the hydrated films while minimizing the manganese oxide-stainless steel interface resistance, eliminating much of the Nyquist semi-circle and providing a rapid frequency response. Proper identification of the source of the semi-circle in Nyquist plots is important as it facilitated the identification of the key limitation of these films (interface resistance) and allowed for their thoughtful optimization. Minimizing resistance and maximizing capacitance are vital for optimizing the material performance, especially for applications in ECs.

By studying the Nyquist plot semi-circle for manganese oxide films of varying dry:wet ratios, we were able to determine that the dry portion of the film needs to reach a critical thickness before the contact resistance is minimized to the full extent possible. For the dry:wet ratios tested in this thesis, dry film thickness of 5% or higher resulted in fully-minimized Nyquist semi-circles, while dry films of 1% resulted in larger contact resistances that were only slightly reduced compared to the "wet" manganese oxide films. The resistance associated with the Nyquist semi-circle was greatly reduced for the films with a dried manganese oxide layer, improving their electrochemical performance.

However, a question remains as to whether the small residual semi-circles seen in these electrodes' Nyquist plots are due to some remaining contact resistance or a charge-transfer resistance of the pseudocapacitive reaction itself. While manganese oxide's pseudocapacitive reaction should theoretically result in a Nyquist plot semi-circle, its high capacitance and presumably low resistance will make it measurable only at very

high frequencies, and because we do not know the exact value of this charge transfer resistance, we cannot know the exact frequency at which to expect it. It is possible that this semi-circle from the pseudocapacitive reaction is outside of our measurement frequency range. This question will be further explored in Chapter 6, which studies manganese oxide with carbon materials is microcavity electrodes. The extremely small amount of electrode material used in these electrodes means the capacitance is lower and resistance is higher than the electrodes studied in this chapter. This will shift manganese oxide's pseudocapacitive semi-circle to lower frequencies, making it more likely that we will be able to detect it in our EIS measurements.

Identifying the main source of interfacial resistance in these manganese oxide films raises considerations that should be made when fitting equivalent circuits to manganese oxide EIS data. After methodically testing and considering popular pseudocapacitive circuit models, we determined that the most appropriate was a circuit that consisted of a resistor followed by a parallel unit with a constant phase element on one side and a resistor and constant phase element on the other side. However, the arrangement of these circuit elements was prompted by the fact that the parallel resistor and constant phase element are usually thought to be attributed to manganese oxide's pseudocapacitive reaction. However, we know that this is not the primary source of interfacial resistance in our "wet" manganese oxide electrodes. Rather, poor contact at the electrode-substate interface is the culprit. This prompted a rearrangement of these circuit elements to separate the pseudocapacitance constant phase element from electrode-substrate interface elements. This final proposed circuit model better describes what is

occurring in our particular electrochemical system. Therefore, systematically considering the fit of different circuit models is important as is having some existing knowledge of how an electrochemical system functions.

Chapter 6: Carbon and Manganese Oxide

The combination of carbon and pseudocapacitive materials is attractive as the pseudocapacitive material can impart improved energy storage capacity while the carbon material can help sustain performance at faster rates, when the pseudocapacitive material performance begins to wane.

In this chapter, we will explore how carbon and manganese oxide perform when combined in an electrode by adding manganese oxide to carbon powders by electrodeposition, as was used to synthesize pseudocapacitive manganese oxide in Chapter 5. To study these materials in conjunction, we used our house-made microcavity electrodes, as were employed in Chapter 4. This allowed us to avoid using binders, slurries, and electrode fabrication techniques that could alter the carbons' structure or chemistry. Carbon materials are a relatively complicated substrate for electrodeposition since different carbons can vary in porosity, surface area, and surface chemistry and it is unknown how these variables might impact electrode performance when combined with electrodeposited pseudocapacitive materials.

As we explore how to best electrodeposit manganese oxide on our carbon materials, we will need to consider whether the manganese oxide is blocking access to the carbon, as it is important the carbon remains electrochemically accessible to maintain performance at fast rates. The goal is to deposit manganese oxide only at the surface of the carbon, rather than down the carbon pores. This is important because manganese oxide has an inherently slower energy storage mechanism compared to carbon, so we do not want the manganese oxide depositing down the carbon pores where it will be further

impeded by the resistance associated with ion movement down the pore. Ideally, this will also leave carbon material electrochemically accessible so that it can help maintain the electrochemical performance at faster rates. Electrodeposition was chosen as a method to add manganese oxide to carbon as we believe it may give us some control over where the manganese oxide is positioned on the carbon, especially compared to electrode fabrication techniques that simply mix carbon and manganese oxide powders. This will be considered as we evaluate the performance of manganese oxide and carbon electrodes presented in this chapter.

In this chapter, the performance of electrodeposited manganese oxide on two different carbon materials (Vulcan XC-72 and graphite) is compared to try to evaluate if the type of carbon substrate impacts the performance of manganese oxide. Two different graphite materials are examined to further study the impact of carbon surface area on electrodes with electrodeposited manganese oxide. Additionally, the effect of carbon surface chemistry changes that occur naturally during electrochemistry is explored by comparing electrodes made with oxidized and non-oxidized Vulcan XC-72 carbon. This will give us insight into what factors are important to consider when combining carbon with pseudocapacitive materials like manganese oxide.

6.1 Physical Characterization

Physical characterization of carbon materials and our electrodeposited manganese oxide were presented in the past two chapters. However, we cannot be certain that our manganese oxide films will have the same morphology when grown on porous carbon

materials as they did when grown on the metal substrates (stainless steel and platinum foil) in Chapter 5. Therefore, various attempts were made to attain imaging of our electrodeposited manganese oxide on carbon materials, as will be detailed in the following section.

6.1.1 Scanning Electron Microscopy

Unfortunately, the extremely small electrode volume in our microcavity electrodes as well as their long, cylindrical shape means that direct SEM imaging of our electrodes is not possible. Attempts were made to remove the electrode material from the microcavity for imaging by painting the electrode opening with nail polish and peeling the layer off once dried. While this did lift the electrode material out of the microcavity, the small amount of material immediately fell apart, as the binder-free carbon had nothing to hold it together outside of the microcavity.

Because we were unable to image manganese oxide on the carbon in our microcavity electrodes, we explored other electrode set-ups that may allow us to electrodeposit manganese oxide on carbon. To remain as relevant as possible to this thesis, it was in our interest to use carbon materials that are studied in conjunction with manganese oxide in this chapter: Vulcan XC-72 and graphite. One attempt involved coating conductive carbon tape in carbon powder, but high resistance in this electrode set-up made it unsuitable for electrodeposition. Then, we attempted to drop-coat our carbon powders onto glassy carbon. This method was not ideal as it required ultrasonication of our carbon powders to prepare a suspension. Ultrasonication is known

to alter the structure and surface chemistry of carbon materials,[21] and could therefore potentially influence how the manganese oxide grows in unforeseen ways. After encountering difficulty in getting a consistent carbon powder coating from this method, we explored electrodepositing manganese oxide directly onto glassy carbon disk electrodes. Unfortunately, the electrodeposition permanently damaged the glassy carbon disk electrode, which prompted us to forgo a deposition on an SEM-friendly glassy carbon plate, especially since this type of carbon is not analogous to the carbon powders studied in this chapter.

A conductive graphite rod was purchased as a possible SEM-friendly carbon substrate. Graphite materials can vary in their particle size and purity, so this graphite rod is likely not entirely analogous to the graphite materials used in this chapter. However, this at least provides a way to image manganese oxide grown on a carbon material similar to one used in this thesis. This conductive graphite rod was used in a 1 minute manganese oxide electrodeposition. The resulting SEM image (Figure 6-1a) shows a fine platelet structure, similar to that seen in images of manganese oxide on metal foils (see Section "5.1.1 Scanning Electron Microscopy"). However, on a larger scale, the mound-like structures of manganese oxide seen in this SEM image (see Figure 6-1a) are unique to this sample and are not seen with films electrodeposited on metal foils. This is unsurprising as the graphite rod (shown in Figure 6-1c) has a much more irregular topography compared to metal foils. An image of the 325-mesh graphite used throughout this chapter was also collected for comparison (Figure 6-1b), and while the graphite

flakes seen in this sample are generally smaller than the graphite rod, the topography of this carbon materials is still relatively irregular.

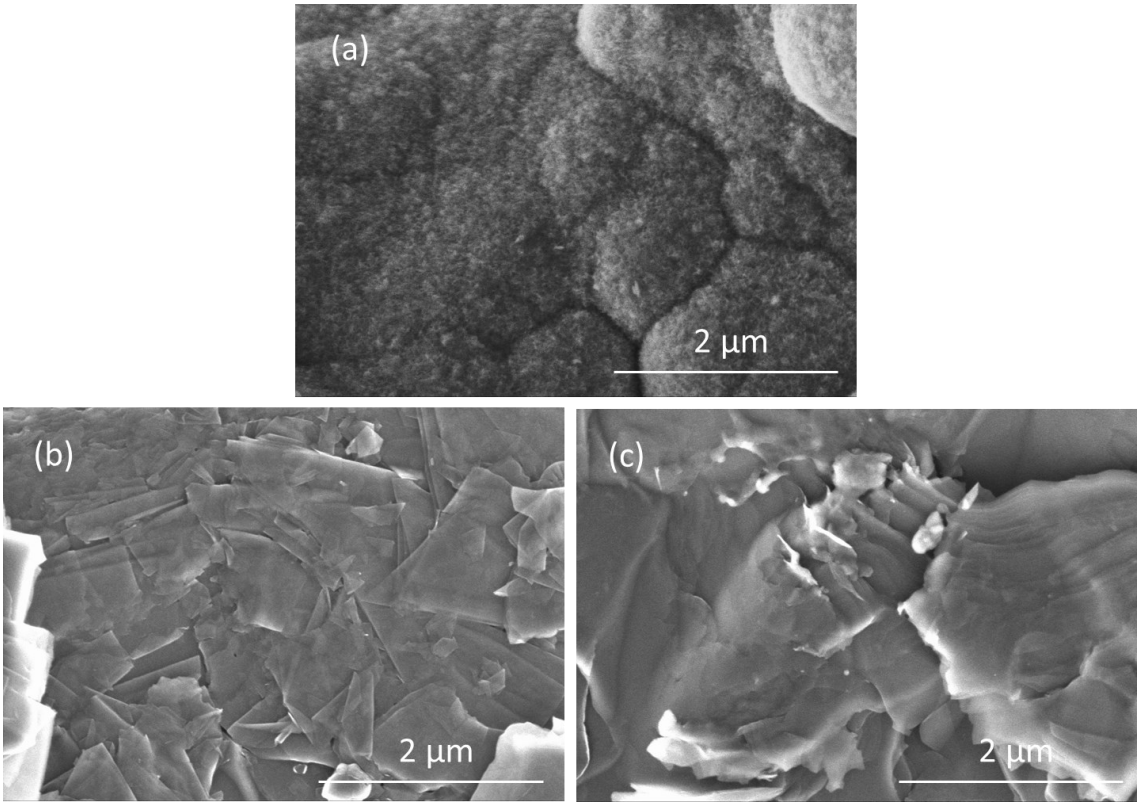

Figure 6-1. SEM images of (a) manganese oxide on a graphite rod and (1 minute electrodeposition time), (b) 325-mesh graphite powder, and (c) the graphite rod used in (a), all at 25 000 times magnification.

Unfortunately, were unable to attain SEM images of manganese oxide on Vulcan XC-72 (which is also used in this chapter). To offer some comparison between our electrodeposited manganese oxide and Vulcan carbon, Figure 6-2a shows manganese oxide beginning to electrodeposit on stainless steel (electrodeposition time of approximately 1 second) as well as bare Vulcan XC-72 powder at the same scale (Figure 6-2b). It is not known if our electrodeposited manganese oxide will have the same

platelet-shaped structure (as seen in Figure 6-2a) when grown on Vulcan. However, we can imagine that this porous material growing on a porous carbon (see Figure 6-2b) will likely result in a complicated network of electrode material.

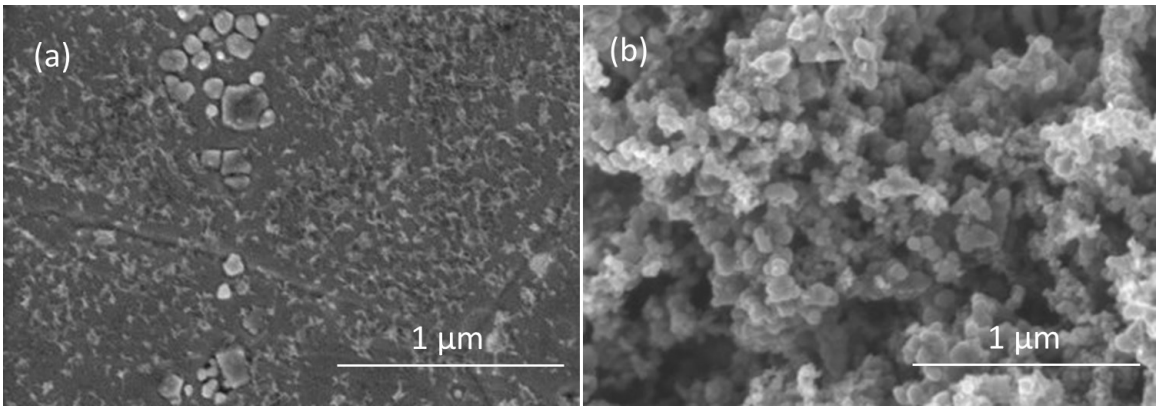

Figure 6-2. SEM images of (a) 1 second manganese oxide deposition on stainless steel and (b) Vulcan XC-72 carbon at 50 000 times magnification.

6.2 Manganese Oxide Electrodeposition on Carbon Substrates

Undoubtedly, porous carbon is a very different substrate than the comparatively smooth metals we used for our manganese oxide electrodes in Chapter 5. Therefore, we wanted to establish if the electrodeposition parameters we used in Chapter 5 still work well when electrodepositing manganese oxide on carbon substrates. During initial attempts to fabricate electrodes with manganese oxide on carbon, it was noted that some of the carbon would often fall out during the electrodeposition procedure (as was confirmed by a decrease in capacitance in EIS or CV after electrodeposition). This was mitigated by doing the electrodepositions at room temperature, rather than the 55 – 60 °C temperature used for electrodepositions in Chapter 5.

Another factor that needs to be considered is that the much smaller size of the microcavity electrodes compared to the electrodes in Chapter 5 (which had geometric surface areas of 6 cm^2) means that a much smaller amount of manganese oxide needs to be deposited. In order to identify what amount of manganese oxide is appropriate for this electrode set-up, repeated electrodepositions of manganese oxide were made on a Vulcan XC-72 electrode. Between each electrodeposition, the electrode was transferred to a cell containing 0.5 M Na_2SO_4 in order to measure its EIS response. In initial experiments, the amount of manganese oxide was controlled by the charge passed during electrodeposition, as this yielded highly reproducible electrodes in Chapter 5. Analyzing EIS data for electrodes that had manganese oxide deposited by this charge-controlled electrodeposition will give us insight into their capacitance (i.e., energy storage abilities) and RC time constant (i.e., rate capabilities).

Nyquist plots for increasing amounts of manganese oxide on Vulcan are shown in Figure 6-3, for an electrode with manganese oxide deposited by a charge-controlled electrodeposition. These Nyquist plots present a decreasing tail size as the total electrodeposition charge increases. This indicates that the capacitance increases as we add more manganese oxide to the electrode, as we would expect from adding more electrode material. However, we can also notice that the electrode with the most manganese oxide is noticeably shifted to the right in the Nyquist plot (Figure 6-3, “5 mC”). This signals that there is an increase in resistance, which will decrease the rate-capabilities of the electrode. A better understanding of how the capacitance and rate-

capabilities are changing can be gained from analyzing the complex capacitance plots for this EIS data.

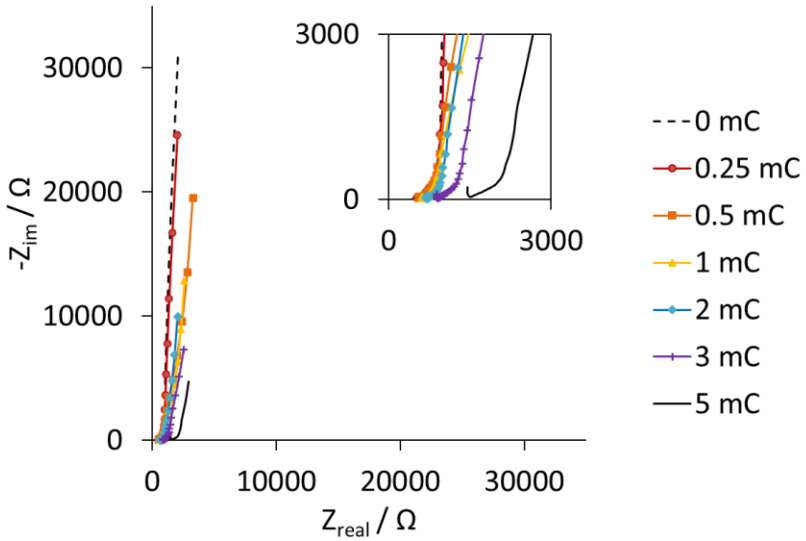

Figure 6-3. Nyquist plot recorded in 0.5 M Na_2SO_4 electrolyte for a Vulcan electrode with increasing amounts of manganese oxide, controlled by charge passed during electrodeposition (total electrodeposition charge is noted in the legend), with an inset showing an enlarged version of the high-frequency region.

The real capacitance plot for this EIS data shows that there is an increase in capacitance as more manganese oxide is deposited onto the carbon, as expected (Figure 6-4a). However, the fact that the real capacitance does not reach a plateau at low frequencies suggests there may be some rate capability issues. This is confirmed by the imaginary capacitance plot, where we see that even for small amounts of manganese oxide (see "0.5 mC" and "1 mC" in Figure 6-4b), a peak associated with the manganese oxide appears at lower frequencies than the original Vulcan peak (Figure 6-4b, "0 s"). Therefore, the manganese oxide in this electrode has slower rate capabilities than the Vulcan carbon. This is not necessarily surprising as the manganese oxide utilizes an

inherently slower mechanism for energy storage (pseudocapacitance) compared to carbon, which stores energy via the electrochemical double layer.

One major issue with this charge-controlled electrodeposition on carbon substrates is that the electrode's increase in capacitance after electrodeposition was variable, especially when compared between replicates. The increase in capacitance after deposition should be proportional to the amount of manganese oxide added, so this suggests that this electrodeposition method is not depositing consistent amounts of manganese oxide for a given amount of charge passed. This is thought to be due to the charging current of the electrode during electrodeposition. Charging current is a flow of charge that occurs when applying a potential different than an electrode's resting potential. This charging current would be small for the metal foils used in Chapter 5 but would likely be a relatively larger proportion of the charge passed in electrodepositions with carbon substrates, due to the high amount of charge they can store in the electrochemical double-layer. Therefore, not all of the charge passed during electrodepositions on carbon is going towards manganese oxide deposition. Since there is often slightly different amount of carbon packed into our microcavity electrode in each replicate, this results in inconsistent amounts of manganese oxide being deposited. Accordingly, it is worth investigating whether we can receive more reproducible results when controlling the electrodepositions in a different way.

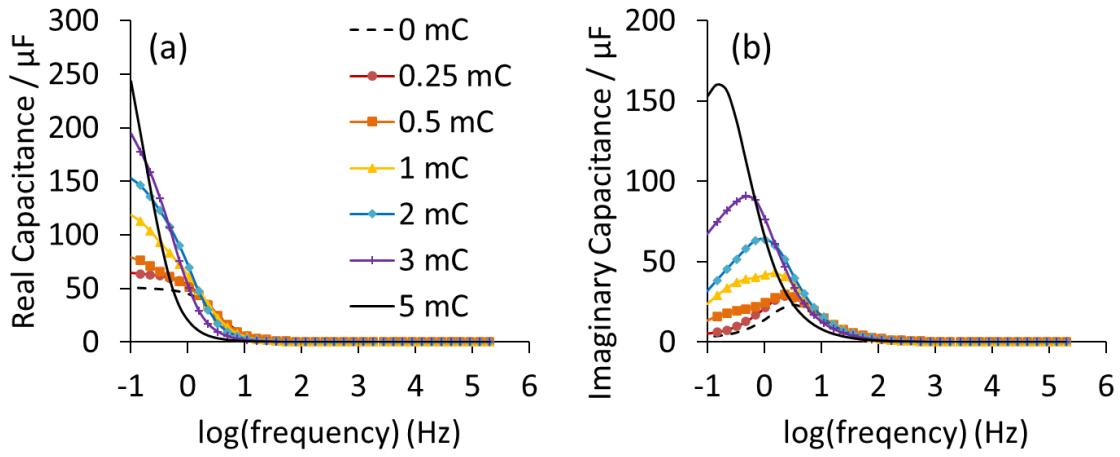

Figure 6-4. Plots showing (a) real capacitance and (b) imaginary capacitance from EIS data recorded in 0.5 M Na_2SO_4 electrolyte for a Vulcan electrode with increasing amounts of manganese oxide, controlled by charge passed during electrodeposition (total electrodeposition charge is noted in the legend).

Because the manganese oxide we deposited on Vulcan via the charge-controlled electrodeposition had variable capacitance and slow rate capabilities, we wanted to explore if there was another way to electrodeposit the manganese oxide that would improve upon these factors. Recall that rate capabilities are not only impacted by the type of material, but also film thickness and porosity. If the manganese oxide were to deposit on the carbon in a thin film and near the outer surface of the carbon, rather than down its pores, this would help maximize its performance at fast rates. Ideally, the carbon pores would remain accessible after manganese oxide electrodeposition, allowing much of the carbon's surface area to remain accessible and contribute to energy storage, especially at faster rates. A diagram depicting this ideal configuration of these two materials is shown in Figure 6-5.

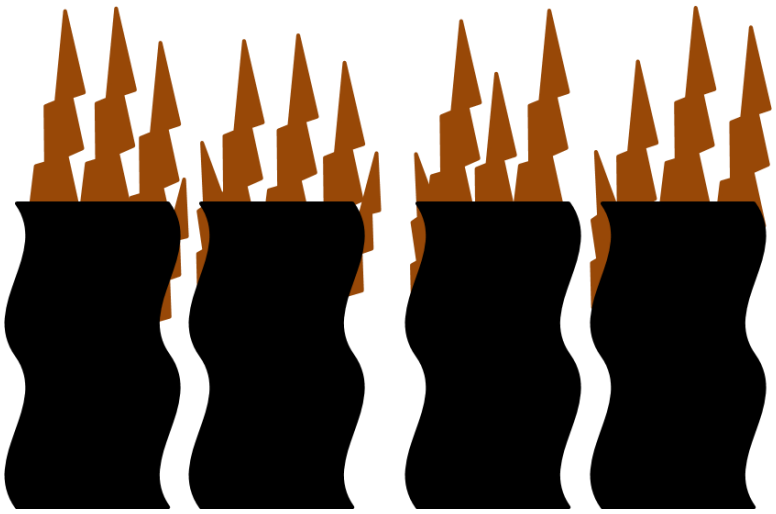

Figure 6-5. Hypothetical physical configuration of electrodeposited manganese oxide on porous carbon.

In order to encourage the manganese oxide to deposit near the surface of the carbon, we created an electrodeposition protocol that applied the deposition potential in short pulses, as described in section "3.2.3 Manganese Oxide Electrodeposition". The rationale behind this technique is that resistance within carbon pores slows the propagation of charge down the length of the pore. So, if the electrode is only held at the deposition potential for a short period of time, there will hopefully not be enough time for charge to fully propagate down the pores, and the depths of the pores will not reach the potential threshold for manganese oxide deposition. The thickness of the manganese oxide film can be controlled by the overall deposition time, so repeated electrodeposition pulses were tested to evaluate different total deposition times. After every five pulses, the electrode was transferred to a cell containing 0.5 M Na_2SO_4 electrolyte in order to record an EIS measurement. Nyquist plots after increasing numbers of 1 second electrodeposition pulses show shorter and shorter tails (Figure 6-6). This indicates that

the capacitance increases as we add more manganese oxide to the carbon surface. Unlike with the Nyquist plots for the charge-controlled electrodeposition (Figure 6-3), we do not see a rightward shift in the Nyquist plots for increasing amounts of manganese oxide deposited by the pulsed technique (Figure 6-6). This suggests that the pulsed electrodeposition technique does not result in a major increase in resistance with increasing amounts of manganese oxide, for the deposition times tested. This suggests that this electrode will likely have better rate performance compared to the electrode made by a charge-controlled electrodeposition.

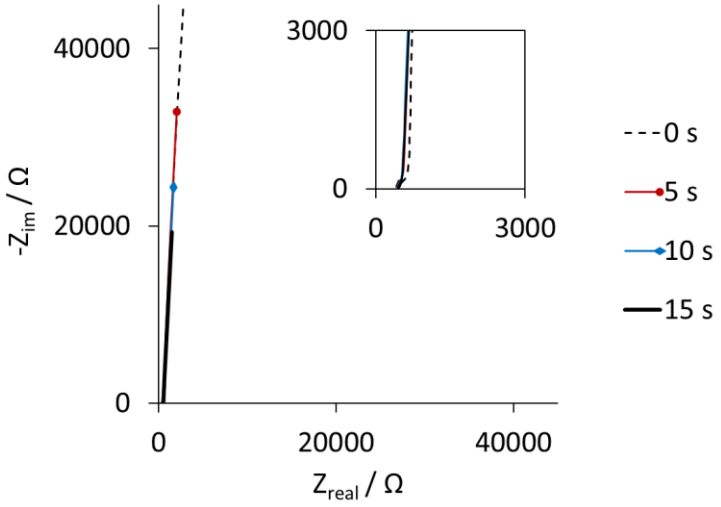

Figure 6-6. Nyquist plot recorded in 0.5 M Na_2SO_4 for a Vulcan electrode with increasing amounts of manganese oxide, controlled by consecutive 1 second pulses of electrodeposition (total electrodeposition time is noted in the legend), with an inset showing an enlarged version of the high-frequency region.

The real capacitance plot for our pulsed electrodeposition technique demonstrates that there is a fairly consistent increase in capacitance for each segment of deposition time shown (Figure 6-7a). Since this capacitance increase should be proportional to the

amount of manganese oxide added to the electrode in each deposition segment, this indicates that this electrodeposition technique is depositing consistent amounts of manganese oxide with each pulse. We also noted more reproducibility with this capacitance increase between replicates, in contrast to the charge-controlled deposition, indicating that this method is better able to deposit consistent amounts of manganese oxide onto different electrodes.

The imaginary capacitance peak shifts very slightly to the left as more manganese oxide is deposited onto the Vulcan surface (Figure 6-7b), meaning the RC time constant is getting slower (i.e., rate capabilities are decreasing). This leftward shift is much less dramatic compared to that seen with the charge-controlled electrodeposition technique, where even for small amounts of manganese oxide the imaginary capacitance peak appears at quite low frequencies (below zero on the logarithmic frequency axis) (Figure 6-4b). This indicates that that the manganese oxide being deposited in our pulsed electrodeposition technique operates at a faster rate. Therefore, this electrodeposition technique was able to improve upon both the reproducibility and rate-capability issues of the charge-controlled electrodeposition technique.

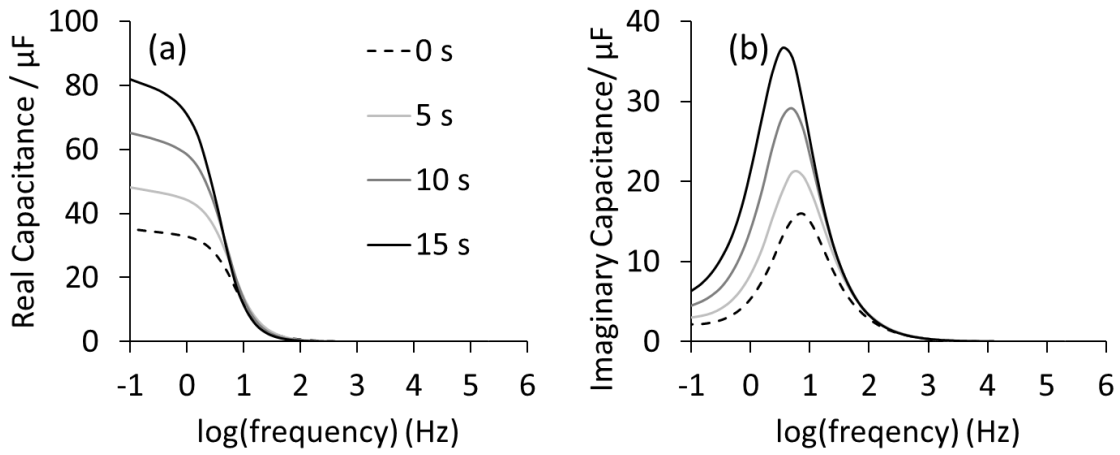

Figure 6-7. Plots showing (a) real capacitance and (b) imaginary capacitance from EIS data of Vulcan with increasing amounts of manganese oxide deposited on top, controlled by consecutive 1 s pulses of electrodeposition (total electrodeposition time is noted in the legend) in 0.5 M Na_2SO_4 electrolyte.

Although our pulsed electrodeposition technique resulted in more reproducible electrodes with better rate capabilities, we should note that there were two electrodeposition variables changed: (a) pulsing rather than having a continuous hold at the deposition potential and (b) controlling the deposition length by time rather than by charge passed. Therefore, we wanted to compare our pulsed electrodeposition technique (which had 15 one-second deposition pulses) to a simple 15 second un-pulsed electrodeposition. The Nyquist plots for a Vulcan electrode before and after this simple timed electrodeposition show a shorter tail after electrodeposition (Figure 6-8), illustrating that there has been an increase in capacitance after manganese oxide was added to the electrode. Similar to the pulsed electrodeposition, we do not see a noticeable shift to the right in the Nyquist plot after electrodeposition (Figure 6-8). Therefore, we do not see evidence of an increase in resistance by evaluating the Nyquist plot. However,

complex capacitance plots of the EIS data can give us a more comprehensive description of how this system has changed after electrodeposition.

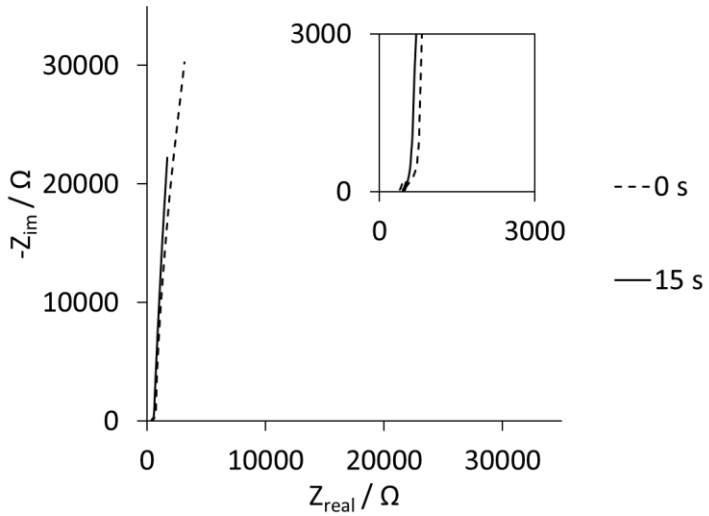

Figure 6-8. Nyquist plot recorded in 0.5 M Na_2SO_4 for a Vulcan electrode with increasing amounts of manganese oxide, controlled by electrodeposition time (non-pulsed), with total electrodeposition time noted in the legend and an inset showing an enlarged version of the high-frequency region.

In the real capacitance plot for our simple, timed electrodeposition, we can see that the capacitance increases by around 20 μF after manganese oxide is added to the electrode (Figure 6-9a). This is much smaller than the capacitance increase seen in our pulsed electrodeposition technique, which was over 40 μF (Figure 6-7a) despite the two techniques having the same overall deposition time (15 seconds). This is likely due to the rests between each pulse in the latter method, which would allow time for the Mn^{2+} concentration at the electrode surface to replenish between each deposition pulse.

An EIS imaginary capacitance plot can be used to evaluate the rate capabilities of our electrode made with a simple, timed manganese oxide electrodeposition. Compared

to the imaginary capacitance peak position for the pulsed electrodeposition technique, the peak position yielded by our simple timed deposition is similar (Figure 6-7b and Figure 6-9b, respectively). This is surprising as we designed the pulsed technique to encourage manganese oxide deposition at the carbon surface (rather than down pores) and therefore expected it to have superior rate capabilities. One possible explanation is that the length of the pulses in this technique was too long and therefore allowed manganese oxide to deposit down carbon pores. However, the excellent rate performance of the manganese oxide in these electrodes casts doubt upon this explanation. Alternatively, there may not be enough time for Mn^{2+} ions to propagate down the carbon pores in our electrodeposition techniques in general, as the carbon electrodes sit in the electrolyte for only a brief moment before electrodeposition begins. This would hinder manganese oxide deposition down carbon pores regardless of whether the electrodeposition potential was pulsed or held for a longer period of time. This explanation is consistent with the excellent rate performance of manganese in our simple, timed electrodeposition, as we expect manganese oxide to perform at its fastest when on the outer surface of the carbon, rather than down the carbon pores where it is slowed by the resistance associated with ion movement down the pores. In fact, for this electrodeposition technique, the imaginary capacitance peak after manganese oxide deposition has a very similar peak position to the Vulcan carbon (Figure 6-9b), which is a typical type of carbon material that would be used in EC applications. With this manganese oxide electrodeposition technique, we have been able to substantially increase the capacitance (i.e., energy storage) of this electrode without majorly impacting the rate capabilities.

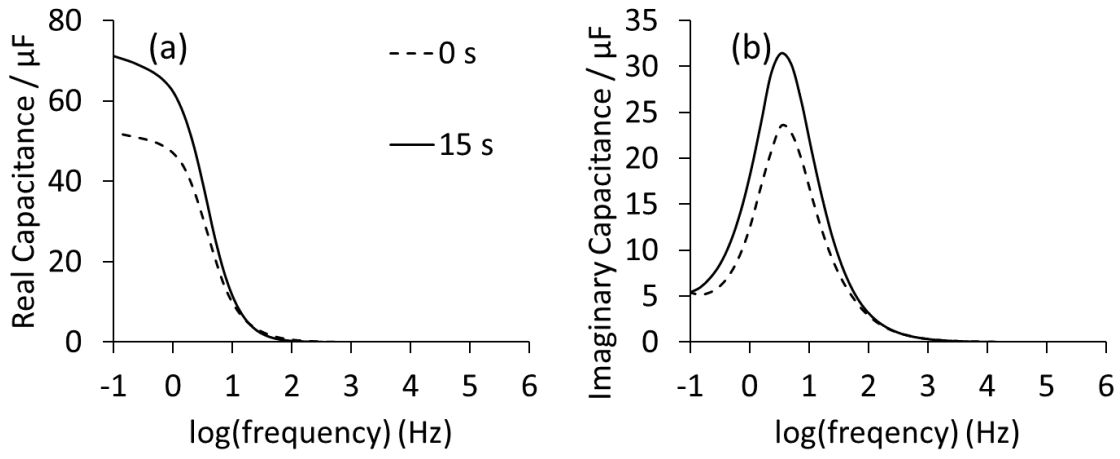

Figure 6-9. Plots showing (a) real capacitance and (b) imaginary capacitance from EIS data recorded in 0.5 M Na_2SO_4 electrolyte of Vulcan with and without manganese oxide, for a 15 s long un-pulsed electrodeposition.

The time-controlled electrodeposition methods used in this section gave us more reproducible results between replicates when compared to the charge-controlled method, potentially due to the background charging currents of the carbon substrates. Both the pulsed and un-pulsed timed electrodepositions yielded a manganese oxide and Vulcan electrode with excellent rate capabilities, as seen by the peak positions in their imaginary capacitance plots (Figure 6-7b and Figure 6-9b). Although the pulsed electrodeposition technique offered higher capacitance for a given deposition time, this can be rectified in the simple, timed electrodeposition merely by increasing the total deposition time. The simple, timed technique is also more straightforward, with fewer depositions overall meaning fewer potential sources of variance. This is important because the time-controlled electrodeposition techniques are sensitive to electrode positioning in the electrodeposition cell, where electrodes positioned closer to the stir bar attain higher amounts of manganese oxide. Because the pulsed technique did not offer any major

advantages, the more simplistic un-pulsed time-controlled method was used as the manganese oxide electrodeposition method of choice for carbon substrates.

6.2.1 Manganese Oxide Electrodeposition Time

After establishing that a simple, timed electrodeposition was the best method for adding manganese oxide to our carbon electrodes, we wanted to test different deposition lengths to explore how different thicknesses of manganese oxide perform on carbon substrates. Additionally, recall that in Chapter 5, we saw that the manganese oxide deposited on a platinum substrate had better performance than "wet" manganese oxide deposited on stainless steel. This was because of reduced resistance due to an improved interface between the manganese oxide and its substrate, as was confirmed by the difference in the Nyquist plot semi-circle. In this chapter, we need to consider that manganese oxide might perform differently on different carbon substrates. Therefore, we studied the EIS response of electrodes with Vulcan XC-72 (which is a carbon black material typical of the type of carbon used in EC applications) and graphite (which is utilized later in this chapter for another project), both with manganese oxide electrodepositions of 1 minute, 2 minute, and 3 minute lengths.

Nyquist plots for representative 1, 2, and 3 minute manganese oxide electrodepositions on Vulcan and graphite are shown in Figure 6-10. Note that for all these Nyquist plots, there is no semi-circle, even at higher deposition times (see "3 minute" in Figure 6-10). This is surprising as these three-minute depositions are approximately three-times the length of the manganese oxide electrodeposition on metal

foils that were presented in Chapter 5. Electrodepositions of such length on metal foils have been shown to be unstable in our lab, peeling and losing contact with the substrate. Yet, on these carbon materials, we do not see a Nyquist plot semi-circle, which we have established is indicative of poor contact between manganese oxide and its substrate (recall Section "5.2 Origin of Interfacial Resistance in Manganese Oxide Films"). Therefore, these results suggest that our electrodeposited manganese oxide has very good contact with both the Vulcan and graphite carbons.

For both the Vulcan (Figure 6-10a) and graphite (Figure 6-10b) electrodes, the length of the Nyquist tail gets shorter as the manganese oxide deposition time gets longer. This indicates that the capacitance increases as the electrodeposition time goes up, as we would expect for increasing amounts of manganese oxide. Also note that the Nyquist plot tails for the graphite-based electrodes are generally longer than the electrodes that utilized Vulcan as a substrate. This indicates that the capacitance is lower for the graphite-based electrodes, which means that they can store less energy overall. This difference in capacitance can be better visualized in complex capacitance representations of this EIS data.

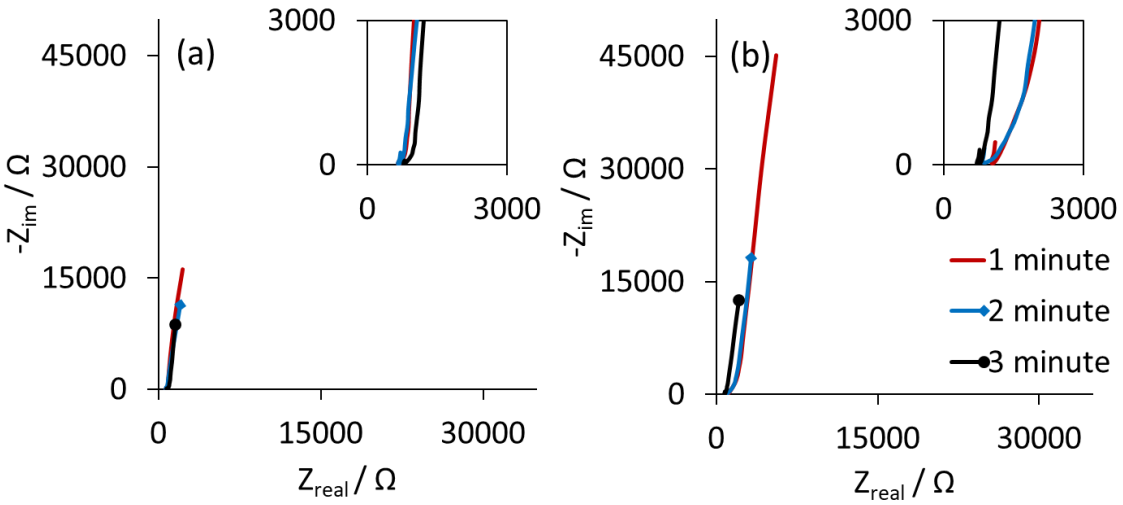

Figure 6-10. Representative Nyquist plots recorded in 0.5 M Na_2SO_4 for 1, 2, and 3 minute manganese oxide electrodepositions on (a) Vulcan XC-72 and (b) 325-mesh graphite, with insets showing an enlarged version of the high-frequency region.

Real capacitance plots of these electrodes approach a plateau in the low frequency region (Figure 6-11). As was understood from the Nyquist plots, we see that for both carbon substrates, the real capacitance increases as the manganese oxide deposition time increases (Figure 6-11). However, the Vulcan electrodes (Figure 6-11a) have generally higher capacitances compared to the graphite electrodes (Figure 6-11b). This could be because our electrodeposition method is depositing different amounts of manganese oxide on the two substrates. However, when the bare carbons' capacitances are compared, we see that Vulcan has an inherently larger capacitance compared to graphite (50 ± 2 and 3.4 ± 7 μF, respectively). This baseline difference in the carbon capacitance could be important if the carbon materials remain electrochemically active after manganese oxide is deposited, as we have hypothesized may be occurring based on our results from the preceding section. If the carbon materials do remain electrochemically

accessible after manganese oxide deposition, the capacitance discrepancy between the Vulcan and graphite electrodes could be due to contributions from the carbon materials themselves rather than a difference in the electrodeposited manganese oxide.

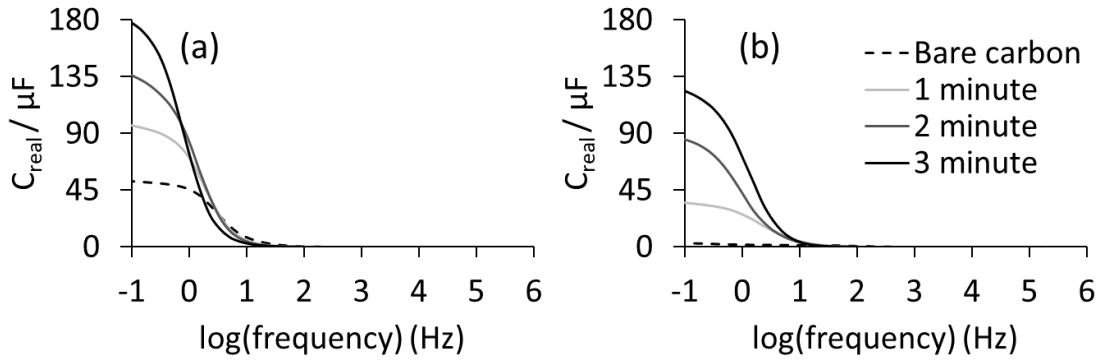

Figure 6-11. Representative EIS real capacitance plots recorded in 0.5 M Na_2SO_4 electrolyte for 1, 2, and 3 minute manganese oxide electrodepositions on (a) Vulcan XC-72 and (b) 325-mesh graphite.

To better compare the capacitances of these different electrodes, the maximum capacitance at low frequencies (as measured by the EIS real capacitance plots) are plotted against each other for the two different carbons. We can see that, while there is some variation in the replicates, there is a reasonably linear relationship between the capacitances at each deposition time for the two carbons, with a slope of approximately one. This suggests that the electrodeposition technique is likely adding the same amount of carbon to the Vulcan versus graphite. In fact, the discrepancy in capacitance between the two data sets is approximately 50 µF, which is roughly the same as the difference in capacitance for the two carbon materials. While the variation in replicates means that we cannot be certain of this linear relationship, there is no evidence from this EIS data that the manganese oxide electrodeposition is depositing different amounts of material on the

different carbon substrates. Therefore, it is likely that the higher capacitance measured for the Vulcan electrodes is due to the carbon material remaining accessible even after manganese oxide electrodeposition. This is a potentially valuable characteristic of these electrodes, as it would allow the carbon material (which has an inherently faster energy storage mechanism) to contribute to energy storage at fast rates, when the manganese oxide may lose some of its energy storage capacity. This is one of the intentions behind combining carbon with pseudocapacitive materials.

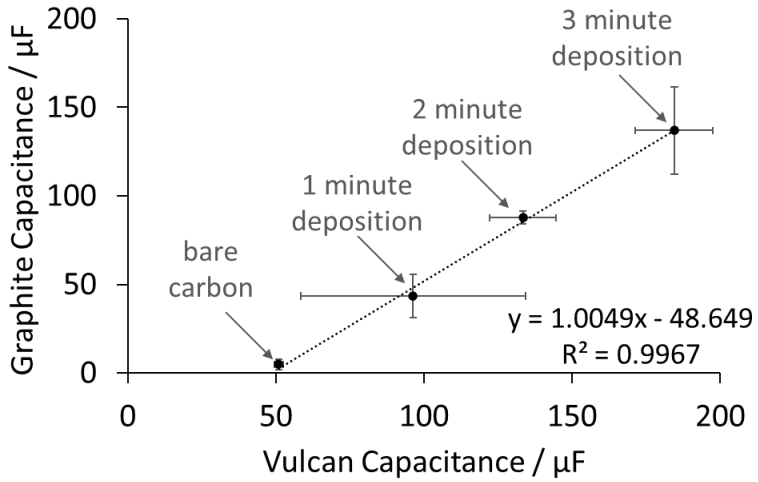

Figure 6-12. Maximum capacitance from EIS real capacitance plots for bare carbon as well as 1, 2, and 3 minute manganese oxide electrodepositions on 325-mesh graphite versus Vulcan XC-72 carbon.

Imaginary capacitance plots of EIS data show peaks positioned at lower frequencies after manganese oxide electrodeposition compared to the bare carbon, indicating that the system is getting slower after manganese oxide is added (Figure 6-13). The difference in peak position, however, is relatively small. Even for the 3 minute electrodepositions, the RC time constants are only an average of approximately one

second slower compared to the bare carbon materials (for both the Vulcan and graphite replicates). This is only a slight decrease in rate capabilities, especially since these 3 minute electrodepositions almost quadruple the capacitance of the Vulcan electrodes. Thus, we were able to make electrodes that combined carbon with manganese oxide that maintained excellent rate capabilities.

For the Vulcan electrodes (Figure 6-13a) the imaginary capacitance plots show peak positions that move to lower and lower frequencies as more manganese oxide is added to the electrode. This indicates that the bare carbon responds fastest followed by the 1 minute deposition, 2 minute deposition, and finally the 3 minute deposition, which is slowest. However, the representative plots shown for the graphite electrodes (Figure 6-13b) do not show a consistent trend in peak position with increasing amounts of manganese oxide. This highlights that the variability in this data makes it difficult for us to make sound comparisons between all these different electrode conditions. Variation between replicates in this set-up is exacerbated by two factors. Firstly, there is a tendency for slightly different amounts of carbon to pack into the microcavity electrode each time, which can contribute to variation even after manganese oxide is deposited since the carbon material appears to remain electrochemically accessible. Secondly, the time-controlled electrodeposition method is particularly sensitive to electrode placement during electrodeposition. While there were attempts to control for this variable as much as possible, each time the electrodeposition cell was dismantled and reassembled, there is some degree of variability introduced.

Additionally, for this EIS data, a comparison of the RC time constants for Vulcan versus graphite electrodes was made difficult by the lack of density in data points at the apex of the imaginary capacitance peaks (shown in Figure 6-13). Because we are interested in the frequency at the peak maximum, this lack of data point density could result in two peaks with visibly different positions having the same frequency selected at its maximum (and therefore the same calculated RC time constant). Quantitatively comparing the peak positions is therefore imprecise using this method. Additionally, peak fitting procedures have not been established for this kind of data and although adding extra data points in the low frequency region would help with this issue, it would substantially increase the EIS measurement time, making it more difficult to meet the EIS measurement requirement of having a stationary system. Therefore, while we can conclude from the EIS data that the rate capabilities of these electrodes decreased after manganese oxide electrodeposition, it would be a benefit to this project to explore another means to evaluate rate capabilities in more detail.

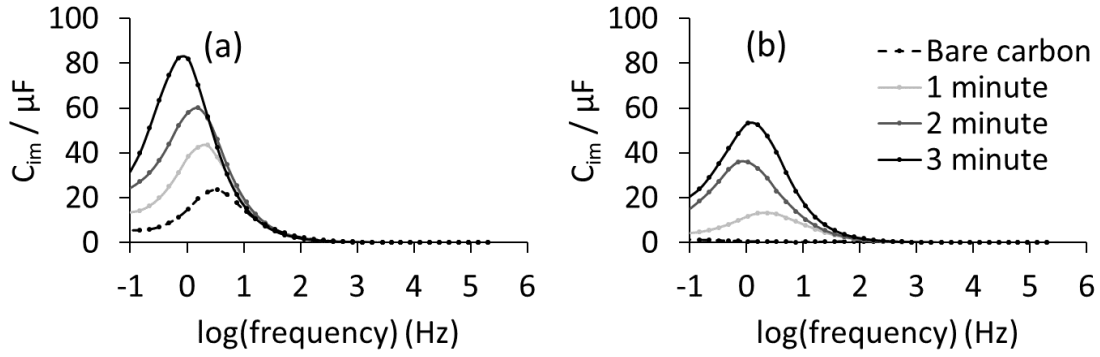

Figure 6-13. Representative EIS imaginary capacitance plots for 1, 2, and 3 minute manganese oxide electrodepositions on (a) Vulcan XC-72 and (b) graphite, with data points shown on each curve.

In addition to the imaginary capacitance, another way we can evaluate rate capabilities is by analyzing CV sweep rate experiments, as was done in Chapter 4 (recall Section "4.2.3 Rate Capabilities"). Like in Chapter 4, the sweep rates were used to convert the CVs from current to capacitance (see Equation 2). For each electrode type, the capacitance at 0.5 V (averaged anodic and cathodic) was calculated for each sweep rate and is shown in Figure 6-14. This figure shows that for all manganese oxide electrodeposition lengths, there is a loss in capacitance as the sweep rate increases. This is an anticipated outcome, as we expect that as we move to faster rates, more of the electrode material becomes inactive as it is unable to keep up. For the Vulcan electrodes (Figure 6-14a), although the electrodes with the highest manganese oxide deposition time start out at the highest capacitances, all the electrodes end up at comparable capacitances at higher sweep rates. A similar observation can be made for the capacitance change with CV sweep rate for the graphite electrodes (Figure 6-14b). However, one noticeable difference for the graphite electrodes is that they have a much sharper capacitance decline at low sweep rates compared to the Vulcan electrodes (Figure 6-14b compared to Figure 6-14a). Therefore, since the graphite-based electrodes have more dramatic capacitance loss in mid-rate CVs, we can say that the graphite-based electrodes have worse rate capabilities than those made with Vulcan. The better rate capabilities seen with the Vulcan electrodes could be due to the Vulcan material remaining active as the manganese oxide performance decreases. Because the Vulcan has a much higher capacitance than the graphite, we would expect it to better maintain performance at fast rates, like is seen in Figure 6-14. However, we must also consider that the manganese oxide could be

operating with different rate capabilities depending on which carbon is used as a substrate. One factor that could influence this is a difference in connection between the manganese oxide and the carbon substrates. However, this seems unlikely since the lack of semi-circles seen in the Nyquist plots of both Vulcan and graphite electrodes (see Figure 6-10) suggests that there is an excellent connection between the manganese oxide and both substrates. Another possibility is that the manganese oxide is electrodepositing with a different film thickness on the two carbon substrates. Vulcan is a much higher surface area carbon than graphite, so the manganese oxide could be depositing on the Vulcan in a thinner film, thereby improving its rate capabilities.

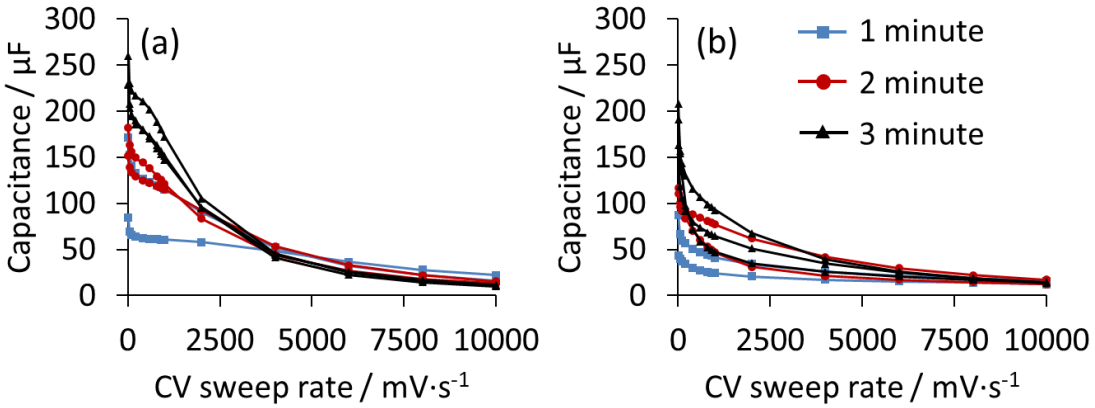

Figure 6-14. Capacitance (calculated from CVs at 0.5 V) versus sweep rate from cyclic voltammetry sweep rate experiment in 0.5 M Na_2SO_4 electrolyte for (a) Vulcan and (b) 325-mesh graphite electrodes with 1, 2, and 3 minute manganese oxide electrodepositions.

In this subsection, we established that we can maintain good rate capabilities in electrodes that combine manganese oxide and carbon. This remains true even for long manganese oxide electrodeposition times, such as our 3 minute electrodeposition, which almost quadrupled the capacitance of our Vulcan electrodes (on average) while

minimally impacting the RC time constant. Electrodes that used Vulcan as a substrate exhibited higher capacitance than those made with graphite. However, the reasonably consistent increase in capacitance per minute of manganese oxide electrodeposition (for both carbons) suggests that this difference is from capacitance contributions from the carbon, rather than a difference in manganese oxide on the two electrode types. Additionally, the rate capabilities of Vulcan-based electrodes outperformed those made with graphite. A question remains as to whether this is due to the Vulcan carbon contributing to the capacitance as the manganese oxide performance wanes or if the high surface area of the Vulcan carbon is causing the manganese oxide to deposit in a thinner film, improving its rate capabilities. The latter of these options will be explored further in the next section.

6.3 Carbon Particle Size Impact on Manganese-Oxide-Containing Electrodes

Undoubtedly, porous carbon is a more complicated substrate than the comparatively smooth metals we used in Chapter 5. In the previous section, we saw that manganese oxide electrodes made with graphite substrates had worse rate performance compared to those made with Vulcan (see Figure 6-14). One possible explanation for this difference is a disparity in surface area between the two carbon materials. The higher surface area of the Vulcan could conceivably cause the manganese oxide to deposit in a thinner layer, improving its performance at fast rates. To further explore this possibility, we studied electrodes made with a graphite that has a particle size of less than 150 μm. This is a larger particle size (and therefore lower surface area) compared to the 325-mesh

graphite used earlier in this chapter, which has particle sizes of 44 μm or less. This allowed us to study manganese oxide on two chemically similar carbon materials that differ only by their particle size. Based on gravimetric surface areas for other similar graphite materials, we expected the 325-mesh graphite to be approximately twice the surface area of the 150 μm graphite. However, it is noteworthy that the electrochemical surface areas of these two graphite materials (as estimated from EIS capacitance values[64]) was more similar than expected (both materials had estimated electrochemical surface areas of 0.3 cm when calculated to one significant figure). We anticipate that the larger particle sized graphite presented in this section may cause manganese oxide to form a thicker film due to the lower available surface area for deposition. As a consequence, we expect to see lower rate capabilities for electrodes made with this lower surface area graphite.

This larger-particle-size graphite with manganese oxide electrodeposited on top yields upright tails in EIS Nyquist plots (Figure 6-15), similar to the Nyquist plot profiles shown earlier in this chapter. Note that the lack of semi-circle in this Nyquist plots suggests there is still a good connection between the manganese oxide and carbon. This is important since poor contact between materials can be a source of resistance and can negatively impact rate capabilities.

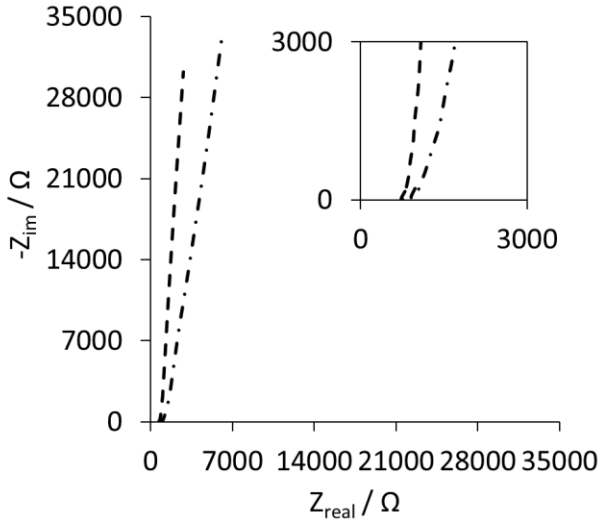

Figure 6-15. EIS Nyquist plots recorded in 0.5 M Na_2SO_4 for 1 minute manganese oxide electrodepositions on <150 µm particle size graphite (different line styles are used for different replicates).

The average maximum real capacitance calculated for these electrodes (see Figure 6-16a) was 49 ± 5 µF compared to the 40 ± 10 µF measured for 1 minute manganese oxide depositions on the larger surface area graphite shown in the previous section. Therefore, there was no difference in capacitance for manganese oxide electrodes made using graphite with particle sizes of less than 150 µm compared to 325-mesh graphite (which has particle sizes less than 44 µm). Recall that when we previously compared electrodes made with Vulcan versus 325-mesh graphite, the Vulcan electrodes had generally higher capacitances (Figure 6-11). This is thought to be due to capacitance contributions from the higher-surface-area Vulcan carbon, since energy storage by electrochemical double-layer is proportional to surface area. Therefore, if these carbon materials are electrochemically accessible, we might expect a similar capacitance difference between electrodes made with the higher surface area graphite from the

previous section and this lower surface area graphite. However, the capacitance contribution of the graphite is very low compared to the manganese oxide capacitance in these electrodes. Therefore, small difference in capacitance for these graphite materials does not seem to significantly impact the overall capacitance of these electrodes after manganese oxide deposition.

The imaginary capacitance plots of EIS data can be used to evaluate the rate capabilities of electrodes made with this lower surface area graphite. After 1 minute manganese oxide electrodepositions, the imaginary capacitance peak positions of these electrodes fall between zero and one on the logarithmic frequency axis (Figure 6-16b). This is similar to the peak positions for one-minute manganese oxide depositions on 325-mesh graphite, as was shown in section "6.2.1 Manganese Oxide Electrodeposition Time" (see Figure 6-13b). This suggests that there may not be a difference in the rate capabilities of manganese oxide on these two different surface area graphite materials, even though we expect the manganese oxide to deposit in a thicker film on the lower surface area carbon used in this section. However, as was discussed earlier in this chapter, the imaginary capacitance plots offer an imprecise value for their RC time constant, in part due to the sparsity of data points in the curves. Therefore, it is beneficial to explore another means of evaluating rate capabilities in these electrodes.

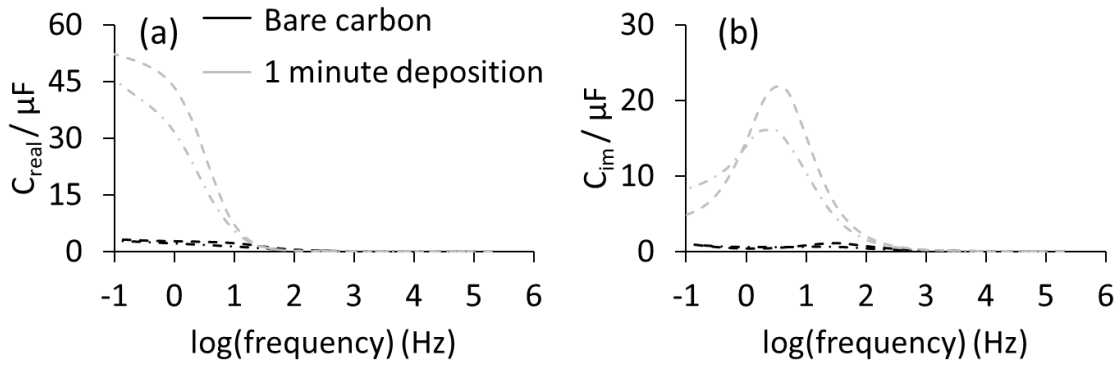

Figure 6-16. EIS complex capacitance plots for (a) real capacitance and (b) imaginary capacitance for 1 minute manganese oxide electrodepositions on <150 µm particle size graphite (matching line styles indicate the data is from the same replicate).

Cyclic voltammetry sweep rate experiments were done with these replicates as they were for previous graphite electrodes. Figure 6-17 shows the calculated capacitance for these experiments for both the lower surface area graphite used in this section (<150 µm) and 1 minute manganese oxide electrodepositions on 325-mesh graphite data, which was previously shown in Figure 6-14b. Given the variability in these replicates, there is no discernable difference in how the capacitance decreases with sweep rate for the two graphite materials. Therefore, there is no evidence from this evaluation that the surface area of the carbon substrate impacts the rate capabilities of electrodeposited manganese oxide. This is surprising, as we expected the lower surface area graphite (the <150 µm material to have a thicker film of electrodeposited manganese oxide, resulting in a sharper decline in capacitance as the CV sweep rate is increased for these electrodes.

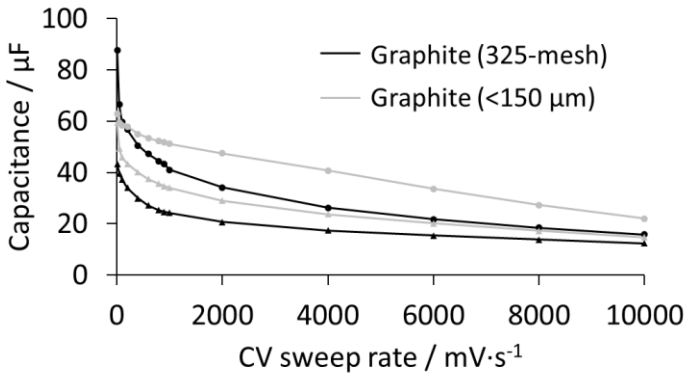

Figure 6-17. Capacitance (calculated at 0.5 V in CVs) from cyclic voltammetry sweep rate experiments for 325-mesh and <150 µm graphite electrodes with 1 minute manganese oxide depositions (different data point shapes indicate different replicates).

In this section we used two graphite materials from the same supplier that differed only in particle size. In this way, we were able to study how the carbon surface area, specifically, impacts the overall performance of electrodeposited manganese oxide. The electrochemical data presented herein did not reveal any difference in the overall capacitance (i.e., energy storage capacity) or rate capabilities for manganese oxide electrodeposited on these two different graphite materials. Therefore, we do not have evidence that carbon surface area impacts the performance of this type of electrode. However, it is noteworthy that the Vulcan carbon studied in the previous section has a substantially higher surface area compared to the graphite materials, as is evident from its much higher capacitance (see Figure 6-11). Therefore, it is possible that the difference in surface area for our two graphite materials was not great enough to resolve any differences this variable causes in electrochemical performance. For example, based on gravimetric surface areas for other similar graphite materials, we expected the 325-mesh graphite to be approximately twice the surface area of the 150 µm graphite. However, the

electrochemical surface areas of these two graphite materials (as estimated from EIS capacitance values[64]) was more similar than expected (both materials had estimated electrochemical surface areas of 0.3 cm when calculated to one significant figure). The surface area difference between these graphite materials may therefore not be large enough to resolve any impact that this has on electrodeposited manganese oxide performance. Therefore, the possibility must be sustained that the rate capability differences seen between Vulcan and graphite electrodes (see Figure 6-14) could still be due to a difference in the carbon surface areas.

To address how inconclusive this experiment was, considerations were made to compare the results shown in this chapter to those of larger electrodes (which would have even higher surface areas). However, we are unable to create larger microcavity electrodes as larger cavities are unable to hold together loose carbon powder. Additionally comparing data from totally different electrode set-ups would be problematic as there could be many new sources of resistance that could be impacting rate capabilities. It could be worthwhile to seek out other carbon materials that have the same chemistry but a more extreme difference in their surface areas. Unfortunately, due to time constraints, we were unable to continue exploring the impact of carbon surface area on manganese oxide performance.

6.4 Carbon Surface Functional Groups' Impact on Manganese-Oxide-Containing Electrodes

The surface chemistry of a carbon material could feasibly play a role in the connection between manganese oxide and carbon, impacting the resistance of the

electrode and thereby influencing its rate capabilities. Additionally, the surface chemistry of carbon materials is quite variable, and it is unknown how this might affect manganese oxide's growth by electrodeposition on a carbon surface. While we have seen that the interface between manganese oxide and its substrate can cause rate issues (recall Section "5.2 Origin of Interfacial Resistance in Manganese Oxide Films"), the absence of Nyquist plot semi-circles in our manganese oxide and carbon electrodes in this chapter means we have no evidence of contact issues between these two materials. We did discover, however, that manganese oxide electrodes made with Vulcan substrates demonstrate better rate capabilities than those made with graphite. Therefore, it is worthwhile to explore whether differences in surface chemistry play a role in electrochemical performance for these electrodes.

In Chapter 4, we established that carbon materials like Vulcan form redox-active surface functional groups during cyclic voltammetry, even in the neutral-pH electrolytes that are necessary when manganese oxide is included in the electrode (see Section "4.3 Carbon Electrochemistry in Neutral-pH Electrolyte"). Because it is reasonable to expect this change in carbon surface chemistry to occur during regular electrode use, it is worthwhile to investigate if it impacts the performance of the manganese oxide electrodes. To study this, Vulcan electrodes were oxidized by cyclic voltammetry. To expediate this process, a slightly higher CV potential window was chosen than that used in Chapter 4, and acidic electrolyte was used. The choice of electrolyte also allowed us to monitor the appearance of redox peaks in the CVs, which indicates the formation of redox-active surface functional groups. CVs from the beginning and end of this oxidation

step are shown in Figure 6-18, and the formation of redox peaks centered around 0.3 V vs. Ag/AgCl are clearly visible. Note that although acidic electrolyte was used in this step (to encourage and monitor the growth of surface functional groups), all other electrochemistry in this section is completed using neutral-pH electrolyte in order to be compatible with manganese oxide.

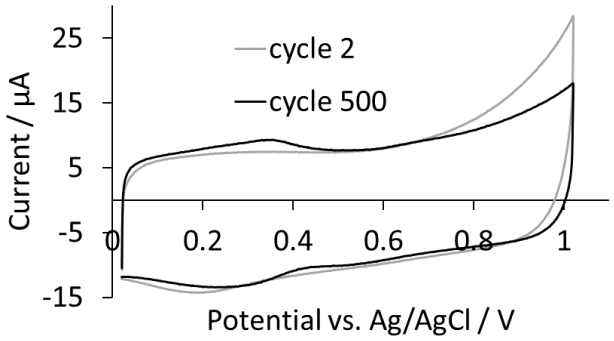

Figure 6-18. CVs recorded during Vulcan oxidation by cyclic voltammetry in 1 M H_2SO_4 electrolyte, showing the formation of redox peaks.

EIS Nyquist plots for one-minute manganese oxide electrodepositions on oxidized Vulcan are shown in Figure 6-19. Like we would expect from capacitive electrode materials, the Nyquist plots present as upright tails. Importantly, there is no semi-circle present, and therefore there is no indication that the change in surface chemistry for the Vulcan results in substantial resistance at the interface between carbon and the electrodeposited manganese oxide. However, a more comprehensive understanding of this EIS data can be gained from evaluating its complex capacitance plots.

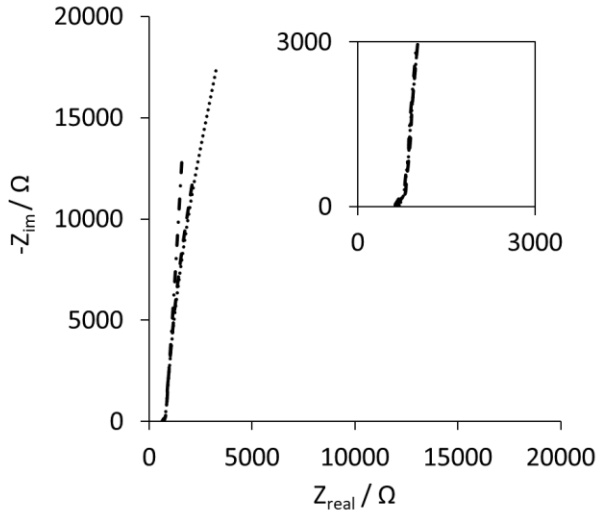

Figure 6-19. EIS Nyquist plots recorded in 0.5 M Na_2SO_4 for 1 minute manganese oxide electrodepositions on Vulcan XC-72 that was oxidized by cyclic voltammetry (different line styles are used for different replicates).

The EIS real capacitance for these electrodes approaches a plateau at low frequencies (see Figure 6-20a). The maximum real capacitance reached at these low frequencies was found to be 110 ± 20 µF for a one-minute manganese oxide electrodeposition on oxidized Vulcan. This is on par with the 100 ± 40 µF capacitance calculated for the non-oxidized Vulcan electrodes presented earlier in this chapter (see Section "6.2.1 Manganese Oxide Electrodeposition Time"). This is not a surprising discovery as we have previously shown in Chapter 4 that the redox-active functional groups grown on the oxidized Vulcan are not active in neutral-pH electrolyte, and they would therefore would not impart an increased capacitance in these tests. These results also confirm that manganese oxide deposited on the oxidized Vulcan does not have a significantly different capacitance compared to manganese oxide grown on the non-oxidized Vulcan.

The imaginary capacitance plots for these electrodes (Figure 6-20b) suggest they have similar rate capabilities to the 1 minute manganese oxide depositions on non-oxidized Vulcan shown previously in this chapter (see Figure 6-13a). However, the low data point density described earlier prevented us from drawing conclusions. Therefore, we again turned to CV sweep rate analysis to better understand the rate capabilities of these electrodes.

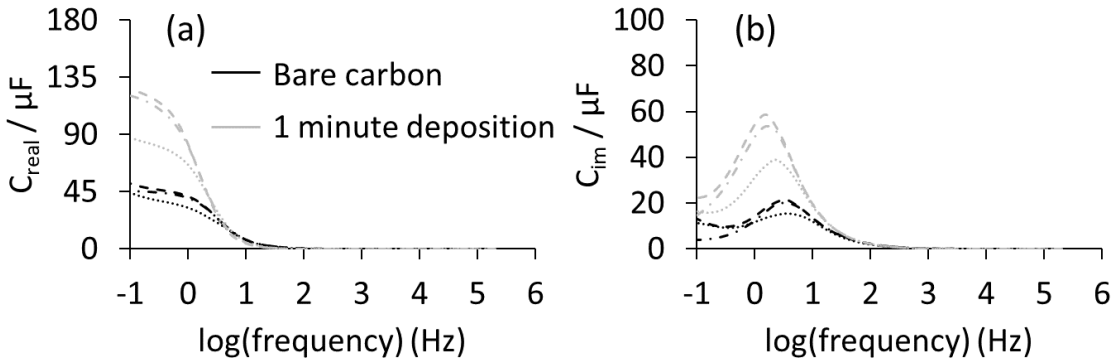

Figure 6-20. EIS complex capacitance plots for (a) real capacitance and (b) imaginary capacitance of 1 minute manganese oxide electrodepositions on Vulcan XC-72 that was oxidized by cyclic voltammetry (matching line styles indicate the data is from the same replicate).

To evaluate these electrodes' rate capabilities in more detail, electrodes with oxidized Vulcan were tested by cyclic voltammetry sweep rate experiments. The resulting capacitance (calculated from CVs at 0.5 V) versus sweep rate is shown in Figure 6-21 along with replicates completed with non-oxidized Vulcan (shown earlier in this chapter). From this, we can see that there is no difference in how the capacitance decreases with sweep rate for the for the oxidized and non-oxidized Vulcan electrodes.

Therefore, Vulcan's surface oxidation caused by cyclic voltammetry has not impacted the rate capabilities of these manganese-oxide-containing electrodes.

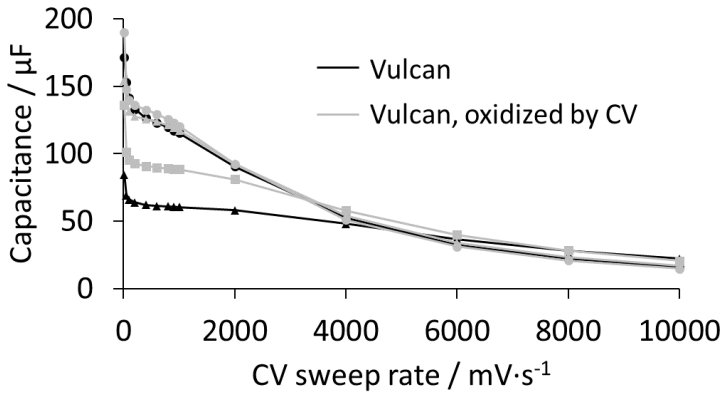

Figure 6-21. Capacitance (calculated at 0.5 V in CVs) versus sweep rate from cyclic voltammetry sweep rate experiments for oxidized and non-oxidized Vulcan XC-72 carbon, all with 1 minute manganese oxide depositions (different data point shapes indicate different replicates).

In this section, we evaluated whether changes in Vulcan's surface chemistry (which is known to happen naturally during electrochemical procedures) might impact the performance of electrodes that combine Vulcan and manganese oxide. From our EIS and CV sweep rate experiments, we were not able to detect any changes in these electrodes' capacitance (i.e., energy storage capabilities) or rate capabilities compared to electrodes made with non-oxidized Vulcan. Therefore, changes in carbon surface chemistry associated with electrochemical oxidation are not likely to have an impact on manganese oxide's performance in these electrodes. However, there are many other variations in surface chemistry that have not been considered in this thesis. It is possible that another variation in carbon surface chemistry could impact its connection with manganese oxide, even if the CV-induced redox-active species do not have this effect.

6.5 Conclusions

In this chapter, we examined the electrochemical response of carbon electrodes with electrodeposited manganese oxide. Charge-controlled electrodepositions of manganese oxide yielded inconsistent results on carbon substrates, possibly due to the charging current of the carbon materials consuming a portion of the charge allocated to be passed during the electrodeposition. Instead, we attained much more reproducible results by controlling the time of the electrodeposition, although there was still some variation in replicates.

We then explored how different manganese oxide electrodeposition times impact the performance of Vulcan- and graphite-based electrodes. Even the longest deposition time tested (three minutes), maintain reasonably good rate capabilities, despite increasing the capacitance (and therefore energy storage) of Vulcan by more than three times. This electrodeposition length is approximately three-times the length of depositions used in Chapter 5 and, despite the expectation that it would yield unstable electrodes, there was no sign of manganese oxide instability. Additionally, the lack of semi-circle in the EIS Nyquist plots for these electrodes suggests the manganese oxide and carbon are well-connected.

A comparison of the capacitance for electrodes made with different electrodeposition times on Vulcan and graphite reveal that there is a consistent amount of capacitance gained for the length of deposition, regardless of the carbon substrate. This suggests that our electrodeposition technique deposits a consistent amount of manganese oxide, regardless of differences in the carbon substrates. However, an examination of CV

sweep rate experiment results revealed that electrodes made with Vulcan maintained their capacitance better as the rate of the CVs increased, compared to electrodes that were made with graphite. A likely factor in this is that the carbons stay electrochemically accessible after manganese oxide electrodeposition, as was suggested from the finding that the electrodes made with Vulcan had generally higher capacitance than those made with graphite. This would allow the Vulcan (which has a much higher capacitance than graphite) to continue contributing to energy storage when the rates get too high for the manganese oxide to maintain its performance.

Conceivably, the surface area of the carbon substrates used in this chapter could impact the thickness of the electrodeposited manganese oxide (e.g., a higher surface area carbon could cause manganese oxide to deposit in a thinner film). Because we know that film thickness impacts rate capabilities (thinner films are faster), it was important to evaluate if carbon surface area impacts the performance of the electrodes made in this chapter. To evaluate this, we compared electrodes made with graphite of two different particle sizes, both with one-minute manganese oxide electrodepositions. There was no difference found in the capacitance or rate capabilities for these electrodes, suggesting that carbon surface area is not an important factor in performance for these electrodes. However, there is a possibility that the difference in surface area between these two graphite materials was not great enough to see its influence on electrochemical performance.

In Chapter 4, we established that carbons like Vulcan form redox-active surface functionalities during electrochemistry in neutral-pH electrolyte. Therefore, it was

important to evaluate if this change in carbon surface chemistry could impact the performance of electrodes with electrodeposited manganese oxide. To test this, we oxidized Vulcan by CV in order to compare electrodes made with oxidized Vulcan versus non-oxidized Vulcan. The absence of a semi-circle in EIS Nyquist plots for electrodes made with oxidized Vulcan suggests that the formation of redox-active surface functional groups has not resulted in poor contact between manganese oxide and the carbon. Additionally, no difference was found in the capacitance or rate capabilities of electrodes made with oxidized versus non-oxidized Vulcan, suggesting that the difference in surface chemistry does not impact the performance of these electrodes. However, it is possible that the change in surface chemistry studied in this section was too small of a portion of the carbon surface area to have a measurable impact on performance. Additionally, it is possible that there exists surface functionalities that do impact performance, but that the species formed during CV do not have an effect on the connection between manganese oxide and carbon. While this is not a comprehensive study on how carbon surface chemistry impacts the connection between carbon and manganese oxide, we were able to determine that the changes in carbon surface chemistry that occur naturally during electrochemical testing do not impact the overall performance of these electrodes.

An important piece of information to note from this chapter is that the Nyquist plots do not have semi-circles, which indicates that there is an excellent connection between the manganese oxide and carbon substrates. In Chapter 5, we discussed how manganese oxide's pseudocapacitive reaction should theoretically result in a semi-circle associated with the charge-transfer resistance of its Faradaic reaction and its capacitive

electrochemical response. However, the high capacitance of this reaction and its presumably low resistance would make it measurable only at very high frequencies. The very small microcavity electrodes used in this chapter may conceivably shift such a semi-circle to lower frequencies, making it more easily measurable. However, there was still no semi-circle measured in the EIS Nyquist plots in this chapter. This suggests that the small semi-circles seen in many of the Nyquist plots in Chapter 5 were likely from residual contact resistance between the manganese oxide and the metal substrates.

Chapter 7: Conclusions

The aim of this thesis was to better understand the electrochemical performance of systems combining carbon and pseudocapacitive materials, and the factors that impact this performance. Data for electrodes combining carbon and pseudocapacitive manganese oxide was presented in Chapter 6. However, much of the work completed in Chapters 4 and 5, where these materials are studied separately, provides insight in to how these materials come together.

In preparation to study carbon and manganese oxide in conjunction, we examined a number of carbon materials in Chapter 4. This included two carbon materials that were prepared by our industrial partner, Elcora Advanced Materials, for this part of the project. We knew that we wanted to find a material with high-rate capability but needed also to have a clear idea of how the surface chemistry may be impacted by electrochemistry, since that may impact the performance of electrodeposited manganese oxide. In comparing the as-received carbons, the Elcora carbon materials had more redox-active surface functional groups compared to Vulcan XC-72, which was consistent with the higher amount of oxygen detected for the Elcora materials via EDS. However, all four of the carbon materials studied in this chapter saw an increase in redox-active surface functional groups after cyclic voltammetry in acidic electrolytes. However, for this project it was important to establish if this change in surface chemistry occurs in neutral-pH electrolyte, as this is necessary when manganese oxide is introduced to the system.

Redox peaks were readily apparent during cyclic voltammetry in acidic electrolyte, but were less apparent in Na_2SO_4 electrolyte, which is neutral in pH.

However, moving an electrode into an acidic electrolyte after extensive cycling in Na_2SO_4 revealed that both the Vulcan and the Elcora nanoplatelet carbons developed more redox-active functional groups during electrochemistry in neutral pH electrolyte, even though these groups could not be detected in-situ. This highlights an important consideration for when we combine carbon and pseudocapacitive manganese oxide: the carbon surface may be changing during electrochemistry in neutral-pH electrolyte. The possibility that this could impact the connection between the carbon and manganese oxide will therefore need to be considered later in Chapter 6.

An additional unstable redox peak (referred to as "redox peak 3" and shown in Chapter 4) appears in the CVs of Elcora carbons but not in CVs of the Vulcan nor the reduced graphene oxide. This set of peaks could be due to a redox active surface functional group or a redox-active contaminant, such as iron. Further investigation of this species revealed that that it is unstable in acidic conditions and that its degradation accelerated at lower potentials in our experimental potential window. Additionally, the electrochemical profile of redox peak 3 was consistent with the oxidation and reduction of iron ions as they migrate out of carbon pores and away from the electrode surface. However, the identification of the species responsible for peak 3 was inconclusive, as the physical characterization of these materials did not pinpoint a possible source for the signal and the electrochemical results merely suggested, but did not definitively confirm that, iron could be the source of "redox peak 3". Ultimately, it was not worthwhile to continue investigating this issue, as Elcora Advanced Materials was able to eliminate the species responsible for peak 3 but changing their purification procedures.

The rate performance of these four carbon materials was explored through varying the cyclic voltammetry sweep rate. These experiments revealed that the Vulcan and Elcora nanoplatelet carbons were able to better handle fast rates than the reduced graphene oxide and Elcora graphene carbons. However, it is noteworthy that the way these carbon powders pack into our microcavity electrodes could have impacted these results in a way that is not relevant to all electrode set-ups. As rate performance is a critical parameter for EC materials, it was determined from these experiments that Elcora's nanoplatelet carbon would be the most promising of their materials for EC applications.

After numerous rounds of optimization, prototype full-cell EC devices were created using Elcora's carbon materials. Experiments showed that these cells had good capacitor-like electrochemical profiles and maintained their performance after the device was used. Additionally, we were able to use EIS to identify a source of resistance in a cell that utilized Elcora's nanoplatelet carbon in its electrodes. Since we do not expect any Faradaic reactions to be occurring at this carbon electrode in neutral-pH electrolyte, the Nyquist plot semi-circle for this cell is most likely due to a contact resistance between materials in the device. This insight will be useful should Elcora decide they want to further optimize these full-cell EC devices.

In Chapter 5, the source of semi-circles in the EIS Nyquist plots of manganese oxide was identified as resistance between the manganese oxide and its substrate and not the resistance associated with the charge transfer in its Faradaic pseudocapacitive reaction. This is important as this Nyquist plot feature is commonly misidentified as

being due to manganese oxide's pseudocapacitive reaction in the literature. Additionally, it was unclear at the beginning of this project if there would be contact issues between manganese oxide and carbon. Because semi-circles in manganese oxide Nyquist plots are commonly mistakenly attributed to the pseudocapacitive reaction, if we had not done this work then we would have expected semi-circles to appear in our work in Chapter 6, which they do not. Instead, we now know that the lack of semi-circles seen in Nyquist plots in Chapter 6 simply indicates that the manganese oxide and carbon have good contact. The identification of the source of the semi-circle in manganese oxide's Nyquist plot also allowed us to closely evaluate what circuit model may be appropriate for this system. In this thesis, it is proposed that the capacitor and resistor associated with this semi-circle are kept separate from the capacitor associated with manganese oxide pseudocapacitive reaction in circuit models, as we now know these are separate processes.

Chapter 6 explores the performance of electrodes that combine carbon materials and pseudocapacitive manganese oxide. It was found that controlling the length of manganese oxide electrodepositions by the charge passed during the deposition resulted in high variations in replicates. Therefore, the amount of manganese oxide electrodeposited on carbon materials had to be controlled by the time of the deposition. This method presents new sources of variability, such as how close the electrode is to the stir bar during electrodeposition, but it remained a much more reliable electrodeposition method for the carbon substrates used in Chapter 6. By studying different electrodeposition times on both Vulcan XC-72 and 325-mesh graphite, we found that this

electrodeposition method seems to be adding a consistent amount of manganese oxide for a given electrodeposition time, regardless of which carbon was used as a substrate. However, the electrodes made with Vulcan carbon were better able to maintain their performance at faster rates in a CV sweep rate experiment. It is thought that this is due to the carbon materials staying electrochemically active after the manganese oxide is added, allowing the Vulcan to contribute to energy storage at rates that are too fast for the manganese oxide. The graphite, even if accessible, would be less able to do this due to its much lower capacitance compared to Vulcan. Therefore, we were able to create electrodes that benefited from manganese oxide's excellent energy storage properties, while the carbon substrate maintained performance at faster rates. For example, 3 minute electrodepositions of manganese oxide on Vulcan XC-72 almost quadrupled the capacitance of the system while only making the RC time constant approximately one second slower. These electrodes that combine electrodeposited manganese oxide with carbon therefore represent a substantial increase in energy storage, with a relatively minor penalty in rate capabilities when compared to Vulcan XC-72, which is a carbon material that might typically be utilized in EC applications. Unfortunately, a comparison to electrodes only containing manganese oxide cannot be made in this thesis, due to the substantially different size and electrode set-up for manganese oxide films studied in Chapter 5.

Because our electrodeposition method seemed to be depositing a fairly consistent amount of manganese oxide for a given deposition time, it was hypothesized that higher surface area carbons may end up with thinner manganese oxide films. Film thickness is

an important factor in rate capabilities, as thinner films are known to perform better at faster rates. However, 60 second manganese oxide electrodepositions on two graphite materials with different surface areas did not result in electrodes with any significantly different performance. It is possible that the difference in surface areas between these graphite materials is not large enough to see the effect it has on electrode performance, but we did not obtain any evidence that carbon surface area is an important parameter in how the manganese oxide performs in these electrodes.

Because we established in Chapter 4 that the surface chemistry of carbon materials changes during electrochemistry in neutral-pH electrolyte, we wanted to study how this change might impact the performance of electrodes with manganese oxide. Particularly, if this change in surface chemistry hinders the connection between the carbon and manganese oxide, it may introduce substantial resistance between these two materials. This could be confirmed by a Nyquist plot semi-circle, like those discussed in Chapter 5. Comparisons were made between manganese oxide electrodes made with as-received Vulcan XC-72 versus those made with Vulcan that was oxidized by cyclic voltammetry. There was no difference in performance found between these different types of electrodes. In fact, there was no semi-circle found in any of the Nyquist plots studied in this Chapter, suggesting that the electrodeposited manganese oxide tends to have an excellent electrical connection with the carbon substrates used herein. It is possible that a carbon's surface functional groups can have an impact on its connection with manganese oxide, but that the amount or type of surface functionalities formed during cyclic voltammetry was not sufficient to see this impact. Nevertheless, these

experiments did not provide us with evidence that carbon's surface functional groups play a major role in the performance of manganese oxide that is combine with carbon in these electrodes.

The work completed in this thesis has provided important insights with respect to designing electrodes that combine both carbon materials and pseudocapacitive manganese oxide. However, as with any research, there are limitations to the work presented in this thesis. These limitations and suggestions for how this research could be expanded will be explored in the next section.

7.1 Future Work

7.1.1 Carbon

Our industry partnership with Elcora Advanced Materials was limited in time, and therefore there are a number of areas where future work could be completed by the company, if it was of interest. Clearly from the cyclic voltammetry results in Chapter 4, the carbons from Elcora feature either a carbon functional group or contaminant that is not present in either the Vulcan nor reduced graphene oxide (as is evident from the third set of Faradaic peaks present in the CVs of the Elcora nanoplatelet and graphene carbons). Although the company believed there to be iron contaminants in these carbon samples, this could neither be detected nor quantified by XPS and EDS methods. This is despite electrochemical results suggesting that iron contamination looked comparable to the mysterious "redox peak 3" in Elcora carbon sample. Another avenue that could have been taken to detect iron in the Elcora carbon samples would be to soak the carbon in 1

M H_2SO_4 and analyzing the solution with ICP-MS (inductively coupled plasma mass spectrometry). This could potentially detect and quantify iron that is present within these carbon samples. However, the presence of iron would not necessarily prove that it is the species responsible for the third set of Faradaic peaks in the Elcora carbon CVs. If iron were detected, the amount detected using ICP-MS would need to be compared to the amount of iron required to cause the measured size of the Faradaic peaks in the CVs, for the same amount of carbon. Then, an evaluation could be made as to whether or not an iron contaminant would be a reasonable source for the third set of Faradaic peaks in the Elcora carbon CVs. This is important because if the species responsible for peak 3 is an iron contaminant, this could potentially worsen energy loss in the material.[67,68] However, if the species responsible for peak 3 is not an iron contaminant, this could point towards it being a redox-active surface functional group, which could potentially contribute to the energy storage of the carbon, if it could be stabilized.

The full-cell EC devices described in this thesis were made under Elcora's guidance and could likely be further improved upon. If this was of interest to Elcora Advanced Materials, a good place to start would be to test replicates of the cell types presented in this thesis to establish if the cell fabrication methods used are reproducible. As was utilized throughout this thesis, CV sweep rate experiments could be used to evaluate the rate capabilities of different devices and EIS could be used to detect if there were significant contact resistances between layers in the coin cells. While the Na_2SO_4 electrolyte tested in the cells in this thesis would be appropriate if there was a desire to add manganese oxide to the system, higher rate capabilities could be achieved with the

carbon electrodes by switching to 1 M H_2SO_4 electrolyte, which is a higher conductivity electrolyte. Additionally, the extremely high amount of redox-active surface functional groups on the Elcora carbons would mean that these materials could benefit from an energy storage boost in the acidic electrolyte that allows this redox chemistry to be active. The carbon electrodes with no copper foil backing used in this thesis would be appropriate for this application, but this would likely require a re-evaluation of the other coin cell hardware used in these devices. Although it was outside of the scope of this thesis, there are many research directions that could be taken to further understanding of how Elcora's carbon materials perform in EC devices.

One interesting result of our carbon research was the formation of redox-active surface functional groups on Vulcan XC-72 carbon after electrochemistry in 0.5 M Na_2SO_4 electrolyte (Figure 4-11). Recall that there were redox peaks seen after CVs in this neutral-pH electrolyte that were at a different potential from those normally seen in acidic electrolytes. This suggests that there are redox-active functional groups formed in neutral-pH electrolyte that are different from those formed in acidic electrolyte. Changes in carbon surface chemistry in neutral-pH electrolytes are not well-studied in the literature, so a comparison of Vulcan's XPS spectra before and after electrochemistry in neutral-pH electrolyte would be of interest.

One of the limitations in this thesis is that most of the carbon electrochemistry is performed in microcavity electrodes. While this electrode set-up allowed us to study as-received carbon powders without the use of binders and potentially material-altering processing techniques, electrodes of this size and configuration are not typically used in

EC applications. Therefore, it would be of benefit to re-evaluate if some of the electrochemical phenomenon seen in this thesis are reproducible with a more industry-relevant working electrode set-up.

7.1.2 Carbon and Manganese Oxide

As touched on in the background chapter of this thesis, one of the figures of merit important to EC devices is their extremely long cyclic life. [3] This allows them to be used in applications that require frequent charging and discharge, like regenerative breaking,[2] without a loss in performance or the need to regularly replace the device. Recall that one of the downsides of pseudocapacitive materials is that they are expected to have inferior cyclic lives compared to EC systems made exclusively with carbon. Manganese oxide, in particular, can dissolve at lower potentials and has been shown in our lab to flake and degrade in strenuous experiments. Although it is outside the scope of this thesis, testing long-term performance is crucial before materials move to the market. Although we did not see any impacts in electrode performance when we altered Vulcan's surface chemistry, it is possible that we could see differences in manganese oxide's performance on these substrates in longer term testing. The contact between the manganese oxide and carbon at the beginning and end of long-term electrochemical testing could be evaluated using resistances as measured by EIS. For long-term electrochemical testing, CVs can be used to calculate the capacitance fade over time. Additionally, techniques like galvanostatic charge-discharge, which charges and discharges the system at constant currents, can provide a more analogous evaluation of cycle life.

In Chapter 6, we hypothesized that the excellent rate capabilities of our electrodeposited manganese oxide on carbon may be because the manganese oxide is depositing near the outer surface of the carbon, rather than down its pores. It would be helpful, therefore, to obtain imaging of these electrodes to confirm this. This would require designing a new electrode set-up that could more easily be used for imaging. Additionally, cross-sections of an electrode may be helpful in determining if manganese oxide is depositing down carbon pores. The requirement for a larger electrode size and electrode cross-sectioning will likely require the introduction of binders to the carbon material. While this kind of electrode would not be identical to the microcavity electrodes used in this thesis, this kind of experiment could help us understand how the manganese oxide electrodeposits on a porous carbon substrate.

In this thesis, we used two graphite materials with different particle sizes to study how carbon surface area impacts the performance of electrodeposited manganese oxide. While we did not see a difference in performance for electrodes made with these two materials, we hypothesized that this may be because the difference in surface area was not great enough to see its impact. Therefore, seeking out two other chemically similar carbons with more dramatically different surface areas may help further investigate this.

Our study on how carbon surface chemistry impact electrodeposited manganese oxide was limited to carbon surface functionalities formed during carbon cyclic voltammetry. While we saw no impact on electrode performance from this change in surface functional groups, there are many ways that carbon surface chemistry can vary. Therefore, it would be interesting to conduct a more robust investigation of how different

oxygen and nitrogen surface functional groups impact the performance of manganese oxide electrodeposited on carbon.

7.1.3 Other Pseudocapacitive Materials

Much of the focus of this thesis has been on how variations in the carbon materials affect the performance of pseudocapacitive manganese oxide films electrodeposited on the carbon. However, there is also merit in exploring how different pseudocapacitive materials perform when deposited on carbon. Other transition metal oxides could be appropriate candidates for further research, especially since many could be electrodeposited onto carbon in a similar way to the manganese oxide studied in this thesis. Unfortunately, few transition metal oxides beside manganese oxide (and the much more expensive ruthenium oxide) exhibit proper pseudocapacitive behaviour in a reasonably large potential window.[10] However, there has been some promising performance reported for manganese oxide doped with small amounts of cobalt.[77] Thus, further experiments exploring how doping affects the systems featured in this thesis could be of interest. If a dopant could significantly increase the stability of the manganese oxide material, the resulting improvement in cycle life could be a pivotal step towards utilizing these high energy-density materials in real EC devices. The effect of dopants on the overall capacitance and rate capabilities would also be of interest.

Another category of possible materials for future work is pseudocapacitive polymers. These materials offer an advantage over pseudocapacitive transition metal oxides in that there are many more possibilities for how a polymer could be altered to optimize its performance or tailor it to a specific application. There has already been

research into combining carbon materials with pseudocapacitive polymers for potential use in EC applications.[78–80] Overall, the synthetic tunability of pseudocapacitive polymers makes them an extremely promising material in this field, with near endless opportunities.

References

1. R. Kötz and M. Carlen, *Electrochim Acta*, **45**, 2483–2498 (2000).

2. B. E. Conway and W. G. Pell, *J Solid State Electrochem*, **7**, 637–644 (2003).

3. B. E. Conway, *Electrochemical Supercapacitors: Scientific Fundamentals and Technological Applications*, Kluwer Academic and Plenum Publishers, New York, (1999).

4. A. Borenstein et al., *J Mater Chem A*, **5**, 12653–12672 (2017).

5. M. B. Sassin, C. N. Chervin, D. R. Rolison, and J. W. Long, *Acc Chem Res*, **46**, 1062–1074 (2013).

6. M. Liu et al., *J Mater Chem A*, **2**, 2555–2562 (2014).

7. J. Kim, K. H. Lee, L. J. Overzet, and G. S. Lee, *Nano Lett*, **11**, 2611–2617 (2011).

8. X. Shi et al., *Electrochim Acta*, **278**, 61–71 (2018).

9. T. Liu, W. G. Pell, and B. E. Conway, *Electrochim Acta*, **42**, 3541–3552 (1997).

10. T. Brousse, D. Bélanger, and J. W. Long, *J Electrochem Soc*, **162**, A5185–A5189 (2015).

11. X. Liu and P. G. Pickup, *J Electrochem Soc*, **158**, A241–A249 (2011).

12. C. Y. Lee and A. M. Bond, *Langmuir*, **26**, 16155–16162 (2010).

13. S. E. Chun, S. Il Pyun, and G. J. Lee, *Electrochim Acta*, **51**, 6479–6486 (2006).

14. M. Toupin, T. Brousse, and D. Bélanger, *Chem Mater*, **16**, 3184–3190 (2004).

15. K. K. Upadhyay, T. Nguyen, T. M. Silva, M. J. Carmezim, and M. F. Montemor, *Mater Chem Phys*, **216**, 413–420 (2018).

16. G. Wang, L. Zhang, and J. Zhang, *Chem Soc Rev*, **41**, 797–828 (2012).

17. G. G. Wildgoose, P. Abiman, and R. G. Compton, *J Mater Chem*, **19**, 4875–4886 (2009).

18. P. S. Guin, S. Das, and P. C. Mandal, *Int J Electrochem*, **2011**, 1–22 (2011).

19. C. A. Thorogood et al., *Chem Mater*, **19**, 4964–4974 (2007).

20. A. M. Oickle, J. Tom, and H. A. Andreas, *Carbon N Y*, **110**, 232–242 (2016).

21. J. Tom and H. A. Andreas, *Carbon N Y*, **112**, 230–237 (2017).

22. L. Z. Fan et al., *Electrochim Acta*, **105**, 299–304 (2013).

23. D. Dong et al., *Mater Chem Phys*, **252**, 1–12 (2020).

24. Q. Abbas, M. Mirzaeian, A. A. Ogwu, M. Mazur, and D. Gibson, *Int J Hydrogen Energy*, **45**, 13586–13595 (2020).

25. R. de Levie, *Electrochim Acta*, **8**, 751–780 (1963).

26. J. Black and H. A. Andreas, *Electrochim Acta*, **54**, 3568–3574 (2009).

27. M. A. Davis and H. A. Andreas, *Carbon N Y*, **139**, 299–308 (2018).

28. C. Zhong et al., *Chem Soc Rev*, **44**, 7431–7920 (2015).

29. B. Pal, S. Yang, S. Ramesh, V. Thangadurai, and R. Jose, *Nanoscale Adv*, **1**, 3807–3835 (2019).

30. M. E. Orazem and B. Tribollet, *Electrochemical Impedance Spectroscopy*, John Wiley & Sons Inc., (2008).

31. H. Keiser, K. D. Beccu, and M. A. Gutjahr, *Electrochim Acta*, **21**, 539–543 (1976).

32. C. Portet, P. L. Taberna, P. Simon, and C. Laberty-Robert, *Electrochim Acta*, **49**, 905–912 (2004).

33. P. Huang et al., *J Power Sources*, **225**, 240–244 (2013).

34. Y. Rangom, X. Tang, and L. F. Nazar, *ACS Nano*, **9**, 7248–7255 (2015).

35. Suhasini, *J Electroanal Chem*, **690**, 13–18 (2013).

36. Y. Chen, J. W. Wang, X. C. Shi, and B. Z. Chen, *Electrochim Acta*, **109**, 678–683 (2013).

37. F. Ataherian and N.-L. Wu, *J Electrochem Soc*, **158**, A422–A427 (2011).

38. L. Chen, N. Gu, R. Ding, L. Qi, and H. Wang, *J Solid State Electrochem*, **17**, 2579–2588 (2013).

39. W. Wei, X. Cui, W. Chen, and D. G. Ivey, *Electrochim Acta*, **54**, 2271–2275 (2009).

40. M. Ghaemi, F. Ataherian, A. Zolfaghari, and S. M. Jafari, *Electrochim Acta*, **53**, 4607–4614 (2008).

41. D. P. Dubal, D. S. Dhawale, R. R. Salunkhe, and C. D. Lokhande, *J Electroanal Chem*, **647**, 60–65 (2010).

42. L. M. Gassa, H. T. Mishima, B. A. L. De Mishimab, and J. R. Vilche, *Electrochim Acta*, **42**, 1717–1723 (1997).

43. P. L. Taberna, C. Portet, and P. Simon, *Appl Phys A Mater Sci Process*, **82**, 639–646 (2006).

44. P. L. Taberna, P. Simon, and J. F. Fauvarque, *J Electrochem Soc*, **150**, A292–A300 (2003).

45. H. Wang and L. Pilon, *Electrochim Acta*, **63**, 55–63 (2012).

46. M. Hall et al., in *Conference on Precision Electromagnetic Measurements*,, p. 34–35, IEEE, London, UK (2004).

47. P. Agarwal, *J Electrochem Soc*, **139**, 1917–1927 (1992).

48. K. H. Kangasniemi, D. A. Condit, and T. D. Jarvi, *J Electrochem Soc*, **151**, E125–E132 (2004).

49. T. I. T. Okpalugo, P. Papakonstantinou, H. Murphy, J. McLaughlin, and N. M. D. Brown, *Carbon N Y*, **43**, 153–161 (2005).

50. E. Papirer, R. Lacroix, J. B. Donnet, G. Nanse, and P. Fioux, *Carbon N Y*, **32**, 1341–1358 (1994).

51. J. C. Lascovich, R. Giorgi, and S. Scaglione, *Appl Surf Sci*, **47**, 17–21 (1991).

52. B. Lesiak et al., *Appl Surf Sci*, **452**, 223–231 (2018).

53. A. Ganguly, S. Sharma, P. Papakonstantinou, and J. Hamilton, *J Phys Chem C*, **115**, 17009–17019 (2011).

54. K. Nkrumah-Amoako, E. P. L. Roberts, N. W. Brown, and S. M. Holmes, *Electrochim Acta*, **135**, 568–577 (2014).

55. A. Swiatkowski, M. Pakula, S. Biniak, and M. Walczyk, *Carbon N Y*, **42**, 3057–3069 (2004).

56. H. Valdes, M. Sanchez-Polo, J. Rivera-Utrilla, and C. A. Zaror, *Langmuir*, **18**, 2111–2116 (2002).

57. S. Biniak, G. Szymański, J. Siedlewski, and A. Światkoski, *Carbon N Y*, **35**, 1799–1810 (1997).

58. I. Velo-Gala, J. J. López-Peñalver, M. Sánchez-Polo, and J. Rivera-Utrilla, *Carbon N Y*, **67**, 236–249 (2014).

59. K. L. Smith and K. M. Black, *J Vac Sci Technol*, **2**, 744–747 (1984).

60. S. Contarini, S. P. Howlett, C. Rizzo, and B. A. de Angelis, *Appl Surf Sci*, **51**, 177–183 (1991).

61. A. A. Galuska, J. C. Uht, and N. Marquez, *J Vac Sci Technol*, **6**, 110–122 (1988).

62. M. C. Biesinger et al., *Appl Surf Sci*, **257**, 2717–2730 (2011).

63. J. Tom, thesis, Dalhousie University (2017).

64. H. Ji et al., *Nat Commun*, **5**, 3371-3323 (2014).

65. H. A. Andreas and B. E. Conway, *Electrochim Acta*, **51**, 6510–6520 (2006).

66. B. E. Conway, W. G. Pell, and T. C. Liu, *J Power Sources*, **65**, 53–59 (1997).

67. S. A. Kazaryan, G. G. Kharisov, S. v Litvinenko, and V. I. Kogan, *J Electrochem Soc*, **154**, A751–A759 (2007).

68. H. A. Andreas, K. Lussier, and A. M. Oickle, *J Power Sources*, **187**, 275–283 (2009).

69. A. Allison and H. A. Andreas, *J Power Sources*, **426**, 93–96 (2019).

70. A. Allison, M. A. Davis, F. Licht, J. M. Pratt, and H. A. Andreas, *J Electrochem Soc*, **167**, 80503–80511 (2020).

71. M. A. Davis and H. A. Andreas, *Electrochim Acta*, **292**, 147–156 (2018).

72. H. A. Andreas, J. M. Black, and A. A. Oickle, *Electrochim Acta*, **140**, 116–124 (2014).

73. M. Toupin, T. Brousse, and D. Bélanger, *Chem Mater*, **14**, 3946–3952 (2002).

74. M. A. MacDonald and H. A. Andreas, *Electrochim Acta*, **129**, 290–299 (2014).

75. F. Béguin and E. Frackowiak, *Supercapacitors: Materials, Systems, and Applications*, Wiley-VCH, Weinheim, Germany, (2013).

76. C. Jo, I. Hwang, J. Lee, C. W. Lee, and S. Yoon, *J Phys Chem C*, **115**, 11880–11886 (2011).

77. J. K. Chang, M. T. Lee, C. H. Huang, and W. T. Tsai, *Mater Chem Phys*, **108**, 124–131 (2008).

78. C. W. Kang et al., *J Mater Chem A*, **9**, 17978–17984 (2021).

79. M. Boota et al., *ChemSusChem*, **8**, 3576–3581 (2015).

80. H. L. K. S. Mosch et al., *Langmuir*, **32**, 4440–4449 (2016).